# REVIEW

of the

CTRICAL COMMUNICATION LABORATORY

PPON TELEGRAPH AND TELEPHONE PUBLIC CORPORATION

Former Reports of the Electrical Communication Laboratory
Nippon Telegraph and Telephone Public Corporation
from Vol.1, No.1, Sept. 1953 to Vol. 7, No. 12, Dec. 1959

VOLUME 8
NUMBERS 5-6

*Published Bimonthly by*

HE ELECTRICAL COMMUNICATION LABORATORY
NIPPON TELEGRAPH AND TELEPHONE PUBLIC CORPORATION
1551, Kitizyôzi, Musasino-si, Tôkyô, Japan

May-June
1960

Review of the Electrical Communication Laboratory



The Review of the Electrical Communication Laboratory is published six times a year (bi-monthly) by the Electrical Communication Laboratory, Nippon Telegraph Telephone Public Corporation, 1551, Kitizyôzi, Musasino-si, Tôkyô, Japan. Telephone: Tôkyô (391) 2261 and 2271.



Subscriptions are accepted at ¥1,200 per year. Single copy ¥300 each. Foreign postage is ¥300 per year or ¥50 per copy. Remittance should be made in check payable to the Electrical Communication Laboratory and mail to the Director.

Printed by Aoyama Printing Co., Tokyo, Japan

REVIEW
of the
ELECTRICAL COMMUNICATION LABORATORY

NIPPON TELEGRAPH AND TELEPHONE PUBLIC CORPORATION

Volume 8, Numbers 5-6 May-June 1960

U.D.C. 621.315.619

# Development of Paper for Laminates*

*Masaaki KATAGIRI*†

*This paper describes the development of a new paper for laminates which is made from cotton flock and flax.*

(*i*) *When cotton flock is cooked in NaOH solution, the relation between the amount of NaOH (%) and relative-viscosity (cuprammonium solution) or between the amount of NaOH (%) and the amount of α-cellulose is given approximately by the following formula:* $y=ae^{bx}$

(*ii*) *It was found that the maturing of the cooked cotton flock pulps has a good effect on increasing the absorptivity of the paper.*

(*iii*) *Colored papers and papers filled with wear resisting fillers were obtained, and a method of decreasing the water extract conductivity of these papers was developed.*

(*iv*) *Some properties of the newly developed paper are explained.*

## Introduction

This paper describes the development of a new paper for laminates, which is made from cotton flock and flax, having large crystalline regions and a high degree of polymerization in the cellulose.

It has been ascertained from our studies that when cotton flock is cooked in sodium dihydroxide solution, the relation between the amount of NaOH (%) and relative viscosity (cuprammonium solution or between the amount of NaOH (%) and the amount of $\alpha$-cellulose is given by the following formula:

$$y=ae^{bx}$$

where $y$ is the relative viscosity or the amount of $\alpha$-cellulose, $a$ and $b$ are constants, and $x$ is the amount of NaOH (%).

It has also been ascertained that the maturing of the cooked pulps has a good effect on increasing the absorptivity of the paper. Colored papers and papers filled with wear resistant fillers were obtained. Also, a method of decreasing the water extract conductivity of these papers was developed. And, some properties of newly developed paper are explained.

## 1. Raw Materials and Cooking Method

It was previously reported[1][2] how phenol resin laminate was brought to practical use as card and ladder material of WA type relays or switches for cross-bar automatic telephone switching apparatus.

This laminate has good dimension-stability, high insulation resistance, good punching characteristics, and good water proof charac-

* MS in Japanese received by the Electrical Communication Laboratory, May 2, 1960. Originally published in the *Kenkyû Zituyôka Hôkoku* (*Electrical Communication Technical Journal*), N.T.T., Vol. 9, No. 5, pp. 125–138, 1960.

† Plastics Application Research Section.

teristics. The papers for laminates described in this paper are also used for the fabrication of cards and ladders.

In view of the characteristics necessary for card and ladder materials, the author found it was desirable to use those cellulosic raw materials which had large crystalline regions and a high degree of polymerization; and to choose cotton flock and flax, as the basic raw materials.

Figs. 1 and 2 show the characteristics of pulps made from cotton flock. Cooking was carried out under the following conditions:

cotton flock : 100g
NaOH : 8−16%
water : 1 *l*
temperature : 150° C
time : 5 hrs

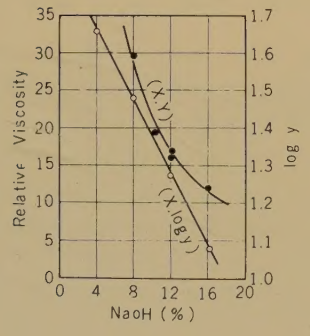


**Fig. 1**—Relative viscosity vs. NaOH (%)

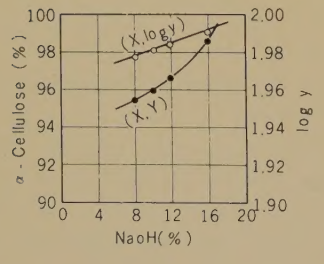


**Fig. 2**—α-cellulose (%) vs. NaOH (%).

The relation between the amount of NaOH (%) and the relative viscosity is shown by

$$y=53.3e^{-0.07x} \qquad (1)$$

where $y$ is the relative viscosity and $x$ the amount of NaOH (%).

For α-cellulose, the same relation is shown by

$$y=86.9e^{0.01x}. \qquad (2)$$

The characteristics of the papers are shown in Fig. 3.

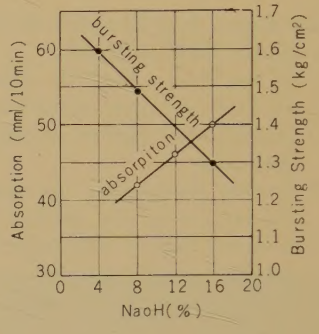


**Fig. 3**—Properties of paper made from cotton flock pulps.

The degree of polymerization in cellulose calculated for the cotton flock pulps is as follows:

NaOH 12%·····2600
NaOH 16%·····2000

From these results, it may be seen that the most desirable amount of NaOH (%) for cotton flocks is 8–12% (150° C–5 hrs).

### 2. Effect of Maturing

The maturing of the cooked cotton flocks (containing little alkali) is carried out in air for 10 days.

The characteristics of the matured pulps are shown in Figs. 4, 5, and 6.

Figs. 4 and 5 show that the values of

relative viscosity, the amount of $\alpha$-cellulose, and the tensile strength (single fiber) do not decrease because of maturing.

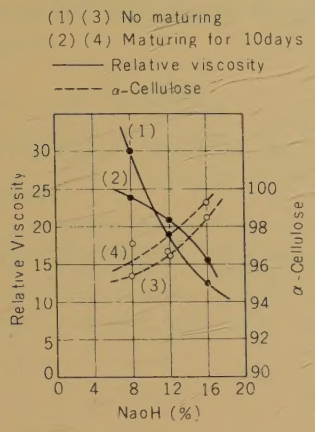


**Fig. 4**—Effect of the maturing of pulps made from cotton flock.

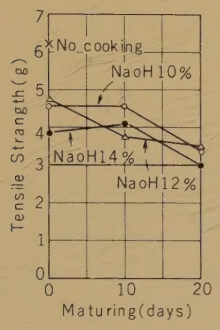


**Fig. 5**—Effect of the maturing of pulps made from cotton flock.

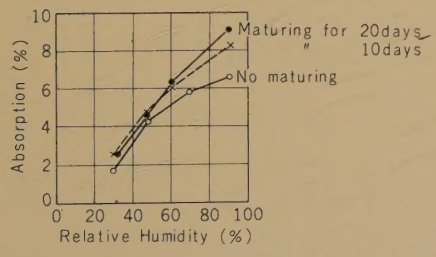


**Fig. 6**—Absorption of cooked pulps made from cotton flock.

### 3. Characteristics of the Paper

Figs. 7 and 8 show the characteristics of the papers made from cotton flock or from flax pulps. The pulps are made under the following conditions.

NaOH ·····10% (2% solution)
cooking temp····156° C
〃 time ····8 hrs
maturing time ··9–10 days

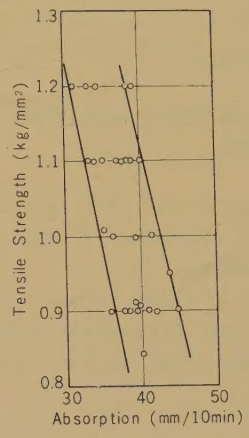


**Fig. 7**—Properties of cotton paper (cross-wise).

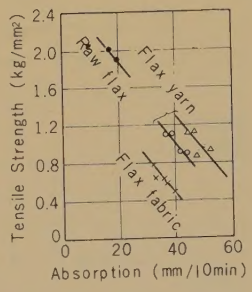


**Fig. 8**—Properties of flax papers (cross-wise).

### 4. Coloring

The black colored papers are made by beater coloring, using water-soluble direct dyestuffs. The color of the finished paper is

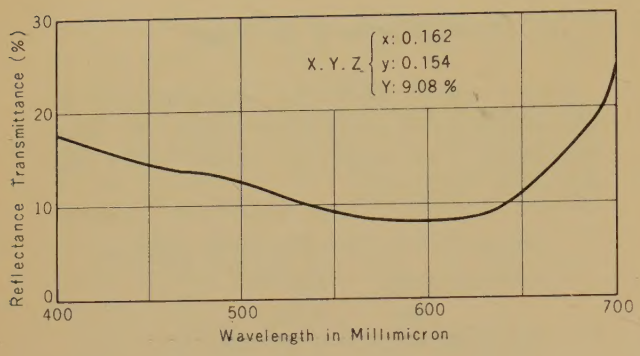


**Fig. 9**—Color of papar.

shown in Fig. 9.

### 5. Papers Filled with Wear Resistant Fillers

Water mixed with 3% graphite and 7% molybdenum disulphide is added to the paper by beater adding.

The wear of these papers, when use for laminatas (card or ladder materials),[2] decreased to one-third of the wear of unfilled laminated papers.

### 6. Water Extract Conductivity

Relationship between the water extract conductivity of paper and the washing time

**Table 1**

WATER EXTRACT CONDUCTIVITY OF FLAX PAPERS

| Raw Materials | Water Extract Conductivity ($\mu\mho$/cm), 20° C | Washing Time of Pulp (min) |
|---|---|---|
| Raw Flax | 48.3–58.8 | 55 |
| Flax Yarn | 48.0–51.5 | 60 |
| 〃 | 54.5–73.2 | 〃 |
| 〃 (3% $M_0 S_2$ added) | 67.5–82.7 | 〃 |
| Flax Fabric (add $MoS_2$–7% graphite 3%) | 21.2 | 210 |

**Table 2**

PROPERTIES OF THE FINISHED PAPERS

| Raw Materials | Paper Type | Thickness (mm) | Density (g/cm$^3$) | Tensile Strength (kg/mm$^2$) | | Elongation (%) | | Absorption (mm/10min) | | Water Extract Conductivity ($\mu\mho$/cm), 20°C |
|---|---|---|---|---|---|---|---|---|---|---|
| | | | | L. W | C. W | L. W | C. W | L. W | C. W | |
| Cotton Flock | Middle paper | 0.099 | 0.50 | 1.69 | 0.95 | 1.9 | 2.9 | 50 | 43 | 33.9 |
| | | 〃 | 0.49 | 1.60 | 0.90 | 2.3 | 3.0 | 45 | 41 | 36.3 |
| | | 〃 | 0.48 | 2.20 | 0.90 | 2.9 | 4.4 | 48 | 39 | 29.5 |
| | Surface paper | 0.103 | 0.47 | 1.68 | 0.91 | 1.4 | 2.9 | 44 | 39 | 27.4 |
| | | 0.100 | 0.50 | 2.20 | 0.90 | 3.0 | 4.7 | 46 | 38 | 32.2 |
| | Colored paper | 0.102 | 0.50 | 1.60 | 1.00 | 2.1 | 3.6 | 45 | 39 | 40.4 |
| | | 0.099 | 0.47 | 2.20 | 0.90 | 3.0 | 4.5 | 45 | 34 | 49.4 |
| Flax | Middle paper | 0.107 | 0.47 | 1.70 | 1.10 | 1.9 | 3.1 | 48 | 43 | 50.0 |

of the pulps is shown in Table 1. The longer the pulps are washed in water the smaller the water extract conductivity of the paper will be.

### 7. Physical Properties of the Finished Papers

The physical properties of the finished laminating papers are shown in Table 2.

### Conclusion

The finished papers for laminates have large crystalline regions, high degree of polymerization in the cellulose, high tensile strength, and low water extract conductivity. These papers, when used for laminates, show good dimension stability, high electric insulation resistance, good punching characteristics, and high wear resistances.

### References

(1) M. Katagiri, K. Koyama, and A. Komine, "Cards for WA type Relays (Report No. 1)," *Reports of the E.C.L.*, N.T.T., Vol. 6, No. 4, pp. 94–98, April, 1958.
(2) M. Katagiri, K. Koyama, and A. Komine, "Studies on Cards for WA Type Relays," *Reports of the E.C.L.*, N.T.T., Vol. 6, No. 8, pp. 287–292, August, 1958.

* * * *

U.D.C. 621.318.424:621.374.32].001.8

# Non-Stationary Parametrons*

*Kazushi ONOSE*†

*The parametron logical circuits used in electronic telephone exchanges and in electronic computers are constructed of stationary parametrons; but in order to select the addresses of memories it is necessary to use parametrons whose oscillations are not stationary. For this purpose a non-stationary exiting system was used but there were difficulties in exciting current adjustments (amplitude and phase). In order to eliminate the above defect d.c. controlled and diode controlled parametrons were experimented on as one method of non-stationary oscillation, and their design data were obtained.*

*The speed of operation of parametron logical circuits; i. e., the modulation frequency of the parametron is restricted by build up and decay time of parametric oscillation, and it is shown that the decay time of diode controlled parametrons is high resulting in a high speed of operations.*

## Introduction

In general, parametrons[1] are classified into 3 groups; namely, I, II, and III, and excitation is applied to these groups in the rhythm I, II, and III. Parametrons oscillate following the same rhythm and information (i.e. oscillation mode) is transmitted from one group to the next group. The oscillation mode is controlled by the phase of small control signals. Such parametron, oscillating with the rhythm of the 3 phase exciting current, is usual and is called a stationary parametron. Parametron logical circuits, which operate on the majority principle, consist only of stationary parametrons.

But in order to select addresses, it is necessary to oscillate the parametron at a desired time. Such an irregularly oscillated parametron is called non-stationary parametron.

Some systems of non-stationary parametrons and their experiments are described in this paper.

* MS in Japanese received by the Electrical Communication Laboratory, Jan. 19, 1960. Originally published in the *Kenkyû Zituyôka Hôkoku* (*Electrical Communication Techinical Journal*), N.T.T., Vol. 8, No. 6, pp. 584–594, 1960.

† Electronics Research Section.

## 1. Some Systems of Non-Stationary Oscillation

Fig. 1 shows the fundamental circuit of a parametron. When a d.c. bias current $I_{d.c.}$ and a high frequency current ($2f$ c/s) $i_{2f}$ flow in the primary windings with appropriate amplitudes, the inductance $L$ of the secondary windings changes periodically according to the following equation:

$$L=L_0(1-2\Gamma\cos 2\omega t). \tag{1}$$

The impedance locus of the secondary winding is shown in Fig. 2. The condition of oscillation for the parametron is given by Eq. (2):

$$\Gamma Q>1 \tag{2a}$$

$$\omega L_0\left(1+\frac{\sqrt{\Gamma^2Q^2-1}}{Q}\right)\geq\frac{1}{\omega C}$$

$$\geq\omega L_0\left(1-\frac{\sqrt{\Gamma^2Q^2-1}}{Q}\right) \tag{2b}$$

where

$$Q=\frac{\omega L_0}{R'}.$$

$R'$: Loss due to load resistance $R_L$ and secondary winding resistance.
$C$: Tuning capacity.

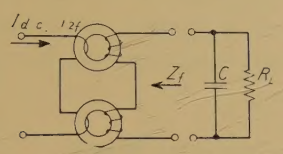


**Fig. 1**—Fundamental circuit of parametron.

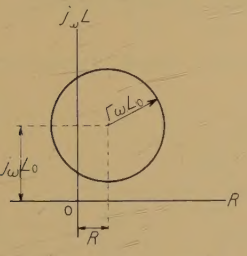


**Fig. 2**—Impedance locus of $Z_f$.

Therefore in order to oscillate the parametron non-stationarily, we have only to control $\Gamma$, $L_0$, or $Q$.

As $\Gamma$ and $L_0$ are functions of $I_{d.c.}$ and $i_{2f}$, the variation[2] of $I_{d.c.}$ can control the parametric oscillations keeping the value of exciting current $i_{2f}$ in constant.

If $Q$ of parametron circuits is small, and so long as $i_{2f}$ is not very high, the parametric oscillation cannot occur. Then it is possible to obtain a non-stationary oscillation by gating a diode or transistor[3] which is connected the across secondary windings of the parametron.

## 2. D.C. Controlled Parametron

Let $L_0$ be defined by Eq. (1) and let $C_2$ and $C_3$ be the capacitances of upper and lower limits of the two-valued region where the parametron will oscillate. Then from Eq. (2), we have

$$\left.\begin{aligned} \frac{1}{\omega C_0}&=\omega L_0 \\ C_0&=\frac{2C_2C_3}{C_2+C_3} \\ \Gamma_c&=\frac{\sqrt{\Gamma^2Q^2-1}}{Q}=\frac{C_3-C_2}{C_2+C_3} \end{aligned}\right\} \quad (3)$$

and

$$\left.\begin{aligned} C_2&=\frac{1}{\omega^2L_0(1+\Gamma_c)} \\ C_3&=\frac{1}{\omega^2L_0(1-\Gamma_c)}. \end{aligned}\right\} \quad (4)$$

Assuming $i_{2f}$ is supplied from a constant current source, increasing $I_{d.c.}$ from $I_1$ up to $I_1+\Delta I$, and as $L_0$ increasing $C_2$ and $C_3$ up to $C_2+\Delta C_2$, $C_3+\Delta C_3$ respectively; $S$ will be defined by $\Delta C_2/(C_0-C_2)$:

$$S=\frac{\Delta C_2}{C_0-C_2}$$

$$=-\frac{\Delta I}{\Gamma_c}\left(\frac{1}{L_0}\frac{\partial L_0}{\partial I_{d.c.}}+\frac{1}{1+\Gamma_c}\frac{\partial \Gamma_c}{\partial I_{d.c.}}\right)$$

In the same way, decreasing $I_{d.c.}$ from $I_1$, down to $I_1-\Delta I$, and decreasing $C_2$ and $C_3$ to $C_2-\Delta C_2'$, $C_3-\Delta C_3'$ respectively,

$$s=\frac{\Delta C_3'}{C_3-C_0}$$

$$=-\frac{\Delta I}{\Gamma_c}\left(\frac{1}{L_0}\frac{\partial L_0}{\partial I_{d.c.}}-\frac{1}{1-\Gamma_c}\frac{\partial \Gamma_c}{\partial I_{d.c.}}\right)$$

is obtained.

If the tuning capacity is set of $C_0$ at $I_{d.c.}=I_1$ and $I_{d.c.}$ increased up to $I_1+\Delta I$ as $S>1$, parametric oscillation will stop.

As $S>s$ for the same value of $|\Delta I|$ and the larger $I_{d.c.}$ the smaller the hysterisis loss becomes; the system in which parametric oscillation stops when $I_{d.c.}$ increases is better. These relations are shown in Fig. 3.

## 3. Diode Controlled Parametron

In the configuration shown in Fig. 4, as $R_L$ is shorted by a low impedance when square wave is applied, oscillation does not occur.

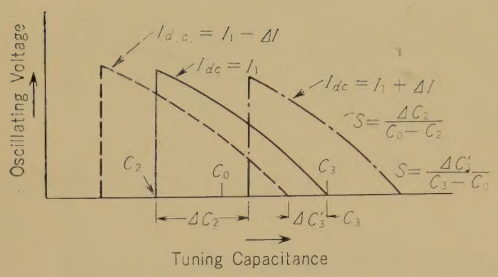


**Fig. 3**—Relation between d.c. bias and tuning capacitance.

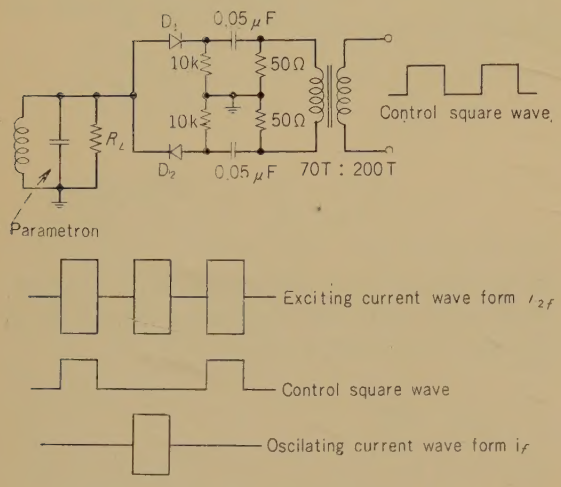


**Fig. 4**—Diode controlled parametron circuit and relations between $i_{2f}$, $i_f$ and control square wave.

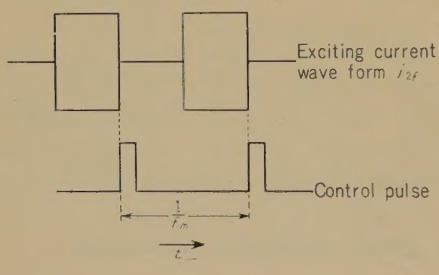


**Fig. 5**—Relation between exciting period and control pulse to improve decay time.

Clock frequency; i.e., the modulation frequency of the parametron $f_m$ is restricted by the build-up time of the oscillation $\tau_r$ and the decay time $\tau_d$. Therefore, if load resistance $R_L$ of the parametron is large and the control square wave is applied as shown in Fig. 5, the speed of operation will be high keeping $2f$ constant.

## 4. Experimental Results

### 4.1. D.C. Controlled Parametron

#### 4.1.1. Static Characteristics

The binocular type parametron[4] circuit

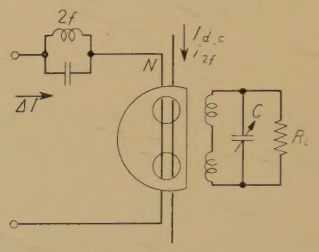


**Fig. 6**—d.c. controlled parametron circuit.

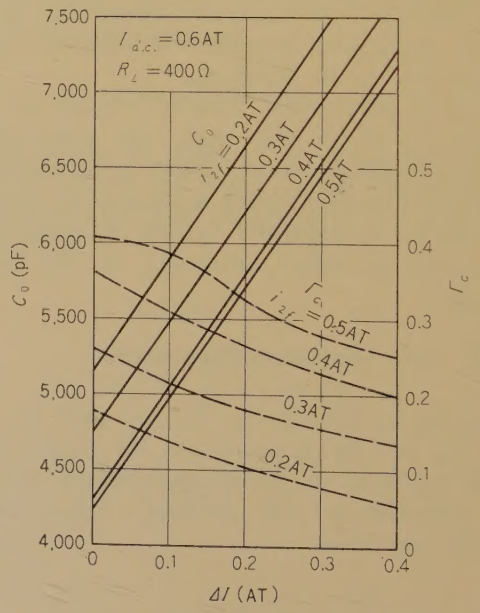


**Fig. 7—(a)**—Variation of $C_0$ and $\Gamma_c$ vs. $I_{d.c.}$.

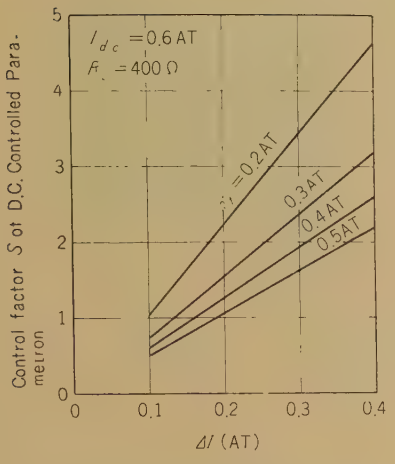


(b)

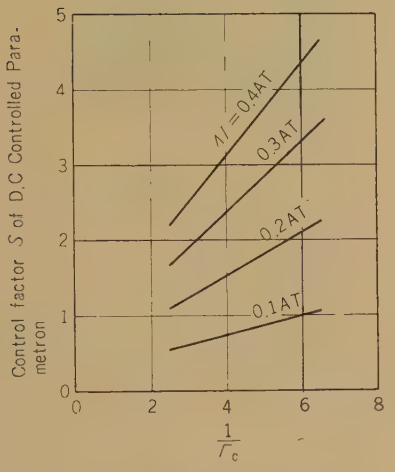


(c)

**Fig. 7 (b) and (c)**—Static characteristics of d.c. controlled parametron.

shown in Fig. 6 was used in the experiment at $2f=2$ Mc/s, $f_m=10$ kc/s. In order to prevent interference between the exciting windings and the control windings $N$, a tuned circuit (resonant frequency $2f$) was connected in series with $N$. The static characteristics are shown in Fig. 7. The experimental results show that oscillations can be controlled when $I_{d.c.}=0.55$ AT, $i_{2f}=0.35$ AT, $R_L=400\ \Omega$, and $\Delta I>0.15$ AT.

#### 4.1.2. Dynamic Characteristics

The control pulse train used in our experiments was produced from parametron information in the following way: the output signal of the parametron is converted to the ON OFF signal according to the phase of the parametron and its output is used as a control pulse. In Fig. 8, when switch "S" is upper position, the width of control pulse "A" is narrower than that of the excitation period due to build-up time of the oscillation; but when "S" is in the lower position, the pulse width of "B" is wider than the excitation period as shown in Fig. 9. Fig. 10 (a), (b) show the value of control factor $S$ for $\Delta I$ using the "A" pulse train and the "B" pulse train respectively.

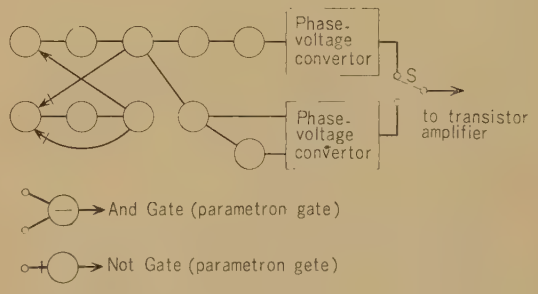


**Fig. 8**—Control pulse generator logical circuit.

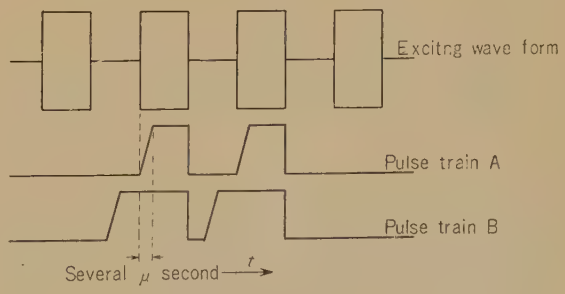


**Fig. 9**—Relations between exciting current and control pulse train.

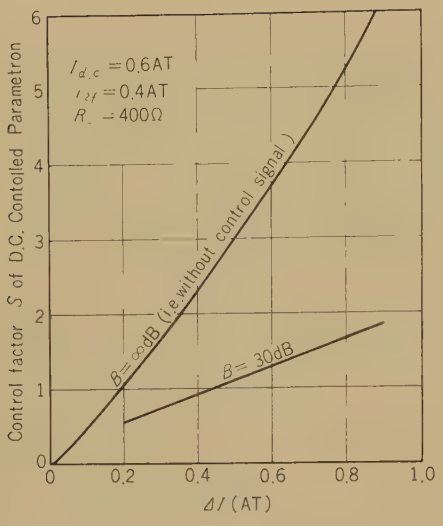


**Fig. 10 (a)**—Control factor $S$ used in control pulse train "A."

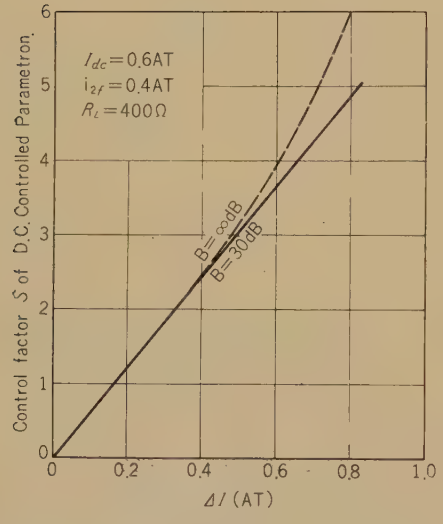


**Fig. 10 (b)**—Control factor $S$ used in control pulse train "B."

When the control pulse width is narrow, as the control signal (it determines the phase of the oscillation) level becomes large, non-stationary control is not successful as shown in Fig. 11 (a). An example of the operational margin of the d.c. controlled parametron is shown in Fig. 13.

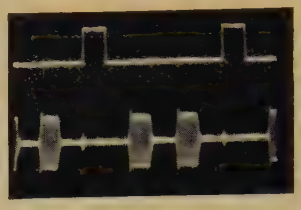

$I_{d.c.}$=0.6AT, $i_{2f}$=0.4AT
$C$=5,000pF, $\Delta I$=0.37AT
$B$=42dB, $R_L$=400Ω

(a)

$I_{d.c.}$=0.6AT, $i_{2f}$=0.4AT
$C$=5,000pF, $\Delta I$=0.37AT
$B$=30dB, $R_L$=400Ω

(b)

**Fig. 11**—Oscillating wave form when width of the square control wave is narrower than that of the exciting wave.

$I_{d.c.}$=0.6AT, $i_{2f}$=0.4AT
$C$=4500pF, $\Delta I$=0.37AT
$B$=30dB, $R_L$=400Ω

**Fig. 12 (a)**—Oscillating wave form when width of the square control wave is narrower than that of the exciting wave.

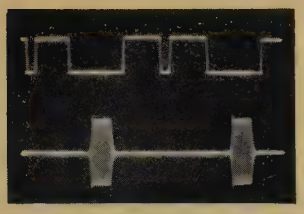


**Fig. 12 (b)**—Oscillating wave form when wave of the square control wave is wider than that of the exciting wave.

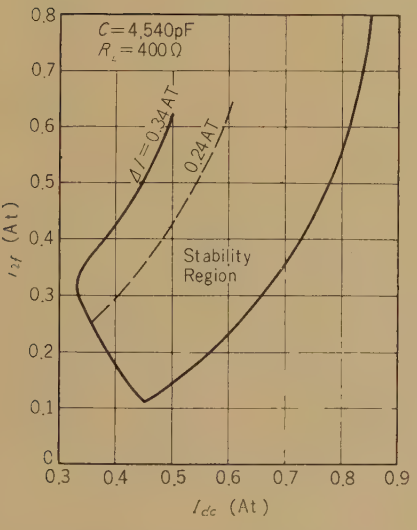


**Fig. 13**—Marginal characteristics.

### 4.2. Diode Controlled Parametron

In our experiments, a pair of toroidal cores, outer diameter 4 mm inner diameter 2 mm, are used. Oscillation of a parametron excited continuously can be interrupted by applying a square wave whose frequency is 50 kc/s and whose peak voltage is 12 V across the primary winding of the transformer in Fig. 4.

If the control pulse is applied as shown in Fig. 5, as the decay time of the oscillation is greatly improved, as shown in Fig. 14, when the peak value of the control pulse is larger than 5 V, the maximum modulation frequency is only restricted by the build-up time. Fig. 15 shows the maximum modulation frequency restricted by build-up time only for various values of $i_{2f}$. Then when $2f$= 2 Mc/s, $I_{d.c.}$=1.0 AT, $i_{2f}$=0.8 AT, $R_L$=1.5 kΩ, $B^*$=30 dB, the maximum modulation frequency becomes 92 kc/s. The larger the value of $i_{2f}$, the higher the modulation frequency becomes, but as the excitation power becomes large also, the limit of the maximum modulation frequency will be about 100 kc/s. Fig. 16 shows that parametric oscillation is improved by diode control.

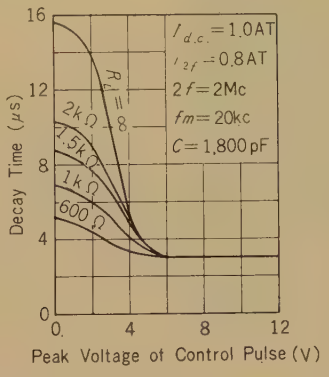


**Fig. 14**—Decay time characteristics.

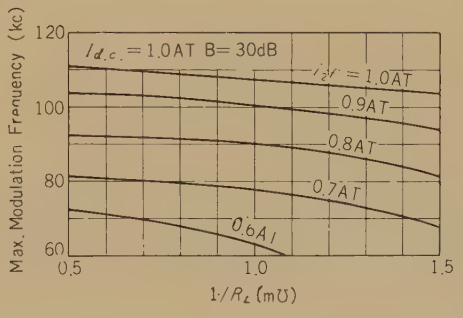


**Fig. 15**—Maximum modulation frequency restricted by build-up time only.

* $B$ is the value concerned with the sensitivity of parametrons, and is defined as $20 \log |I_0/I_s|$, where $I_0$ is the oscillating current flowing through the load resistance of the parametron, and $I_s$ is small signal current which flows in the load resistance of the following parametron as a result of $I_0$.

(a) Exciting Wave Form
$f_m = 50kc$

(b) Oscillating Wave Form
Without Diode Control
$I_{dc} = 1.0AT$, $I_{2f} = 0.8AT$
$R_L = 1.5k\Omega$, $B = 60dB$

(c) Control Pulse
Peak Voltage Value = 12V

(d) Oscillating Wave Form
with Diode Control
$I_{dc} = 1.0AT$, $I_{2f} = 0.8AT$
$R_L = 1.5k\Omega$, $B = 30dB$

**Fig. 16**—Oscillating wave form of diode controlled parametron.

## Conclusion

The problem and design data of the d.c. and diode controlled non-stationary parametrons have been carefully studied. The features of these systems are that the leakage current when the parametron is not oscillating is very small and exciting circuit used for the conventional parametrons can also be used with the non-stationary parametrons.

Moreover, the diode controlled parametrons can speed up the clock frequency of parametron logic without increasing the power consumption.

## References

(1) Goto, "On the Application of Parametrically Excited Non-Linear Resonators," *The Journ. of the Inst. of Electr. Comm. Eng. of Japan.* **38**, 10, p. 770, 1955.

(2) Kiyasu and Yamada, "Memory in Electronic Computer," *The Symposium of the National Meeting of the I.E.C.E.J.*, 1967-11.

(3) Oshima, Nakagome, and Inohana, "Transistor Input and Output Circuits for Parametron and their Applications," *The Journ. of the Inst. of Electr. Comm. Eng. of Japan.* **41**, 9, p. 856, 1958.

(4) Fukui, Shindo, Kurata, and Habara, "Binocular Type Parametron," *The Reports of the E.C.L.*, N.T.T., **7**, 5, pp. 152–166, May, 1959.

* * * *

U.D.C. 621.318.57:621.314.7
621.395.345

# Properties of Compound Transistors for Speech-Path Switches*

*Ichiro ENDO*,† *Kingo YAMAGISHI*,‡ *Shozi YOSHIDA*,‡ and *Kazuhiko GOTO*‡

*The properties of compound transistors, which are hook connections of pnp and npn transistors, are examined for applications to speech-path switches in space-division all-electronic telephone exchange systems. The static characteristics and the switching speeds are first considered from the equivalent circuit of the compound transistors for the case of a three terminal configuration. The automatic lock-out functions and the properties of the multistage cascade connections, which may be available for end marking systems of speech-path networks, are considered. Furthermore, some properties of two terminal configurations are also described.*

## Introduction

Various kinds of elements which are suitable for speech-path switches in all-electronic space-division telephone exchange systems have been investigated in many countries. Some of them, for example silicon pnpn diodes,[1] show useful features; but the stability of their breakdown voltages and their control methods seem not to have been developed yet. Compound transistors (Fig. 1) may be of considerable interest for applications as speech-path switches. Since their general properties[2] are similar to those of pnpn diodes, they may be easily modified with additional devices.

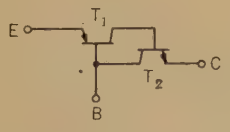


**Fig. 1**—Compound transistor configuration.

For example, the breakdown voltages can be fixed with external voltage sources.

In the following the static characteristics, transmission characteristics, and the switching speed are first described from the equivalent circuit of the single stage three terminal configuration; and the significant properties of automatic lock-out operations as well as multistage cascade connections are described. Furthermore, descriptions of two terminal configurations are given.

In experiments using low-frequency alloy junction transistors as the circuit elements our expectations were realized.

## 1. Properties of the Basic Configuration

In this section, an elementary three terminal connection for speech-path use is considered, and from its equivalent circuit static and dynamic properties may be described.

### 1.1. Equivalent Circuit of the Three Terminal Configuration

Fig. 2 (a) shows the basic three terminal compound transistor configuration for speech-path switches. Its small signal equivalent circuit[3] may be represented as shown in

* MS in Japanese received by the Electrical Communication Laboratory, N.T.T. March 3, 1959. Originally published in the *Electrical Communication Laboratory Technical Journal*, N.T.T. Vol. 8, No. 6, pp. 567–583.

† Chief, Electronics Research Section.
‡ Switching Research Section.

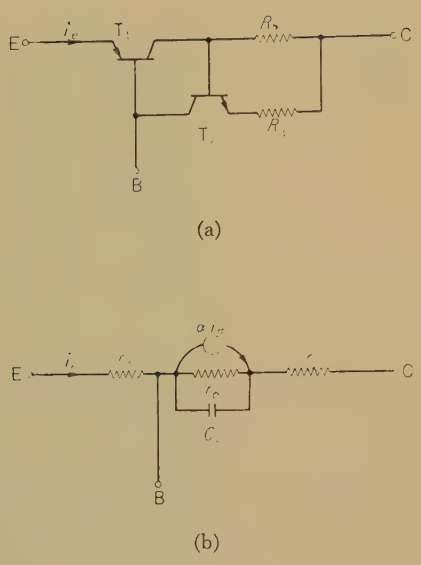


**Fig. 2**—Basic three terminal compound transistor configuration for speech-path switches (a), and its equivalent circuit (b).

Fig. 2 (b), when $R_3$ and $R_4$ are small sufficiently compared with the collector resistances of transistors $T_1$ and $T_2$, and where the small signal parameters $\alpha$, $r_e$, $r_c$, etc. are given as follows:*

$$\alpha = \frac{\alpha_1}{1-\sigma\alpha_2} \tag{1}$$

$$r_e = r_{e1} + (1-\alpha_1) r_{b1} \tag{2}$$

$$r_c = r_c'(1-\sigma\alpha_2) = \frac{r_c'\alpha_1}{\alpha} \tag{3}$$

$$C_c = \frac{C_c'}{1-\sigma\alpha_2} = \frac{C_c'\alpha}{\alpha_1} \tag{4}$$

$$r = \{r_{e2} + (1-\alpha_2) r_{b2} + R_4\}\sigma \tag{5}$$

$$\sigma = \frac{R_3}{r_{e2} + (1-\alpha_2) r_{b2} + R_3 + R_4} \tag{6}$$

$$r_c' = \frac{r_{c1} r_{c2}}{r_{c1} + r_{c2}} \tag{7}$$

$$C_c' = C_{c1} + C_{c2}. \tag{8}$$

In these equations, $\alpha_1$, $r_{e1}$, $r_{c1}$, $C_{c1}$, and $r_{b1}$ are the small signal current amplification factor, emitter resistance, collector resistance, collector capacitance, and base resistance of $T_1$; and $\alpha_2$, $r_{e2}$, $r_{c2}$, $C_{c2}$, and $r_{b2}$ are the small signal current amplification factor, emitter resistance, collector resistance, collector capacitance, and base resistance of $T_2$.

From above equations it is found that the current amplifications of compound transistors can be larger than unity similar to those of point contact transistors, and bistable circuits may be obtained with the same designs.

### 1.2. Properties of the Current Amplification Factor

As shown in Equation (1), $\alpha$ depends not only on the current amplification factors $\alpha_1$ (of $T_1$) and $\alpha_2$ (of $T_2$), but on $\sigma$ of Equation (6), and the emitter imput impedance of the grounded-base connection of $T_2$ determines $\sigma$ when $R_3$ and $R_4$ remain constant. Therefore $\alpha$ increases with increase in the emitter bias current $I_e$.

Fig. 3 shows the low frequency small signal

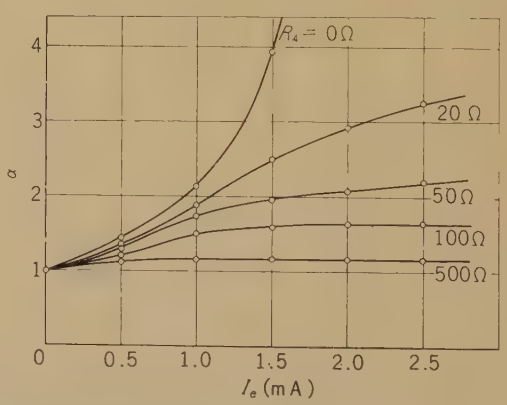


**Fig. 3**—Small signal current amplification factor of three terminal compound transistor.

* In this description, effects of the base resistance of $T_1$ and $T_2$ are considered as the form of input impedances of grounded emitter amplifiers, that is, the emitter resistances of $T_1$ and $T_2$ are assumed to be $r_{e1}+(1-\alpha_1)r_{b1}$, and $r_{e2}+(1-\alpha_2)r_{b2}$, respectively, and the base resistances of $T_1$ and $T_2$ are zero. This assumption is taken in most cases of our research.

characteristics of $\alpha$, employing 2T64 and HJ17D transistors for $T_1$ and $T_2$ respectively, for several values of $R_4$ with constant $R_3$ ($=100\Omega$). The other parameters are also found to vary with $I_e$.

If $\alpha_1$ and $\alpha_2$ are assumed to be

$$\alpha_1=\frac{\alpha_{10}}{1+j(f/f_{c1})},\quad \alpha_2=\frac{\alpha_{20}}{1+j(f/f_{c2})} \tag{9}$$

where

$\alpha_{10}$, $\alpha_{20}$: values of $\alpha_1$ and $\alpha_2$ at low frequencies,

$f_{c1}$, $f_{c2}$: cut off frequencies of $\alpha_1$ and $\alpha_2$,

$f$: frequency in cycles per second,

then frequency characteristics of $\alpha$ are derived as follows:

$$\alpha=\frac{\alpha_{10}}{1+j\frac{f}{f_{c1}}}\left(1+\frac{\frac{\alpha_{20}R_3}{r_{e2}+(r_{b2}+R_3)(1-\alpha_{20})+R_4}}{1+j\frac{r_{e2}+r_{b2}+R_3+R_4}{r_{e2}+(r_{b2}+R_3)(1-\alpha_{20})+R_4}\cdot\frac{f}{f_{c2}}}\right)$$

$$=\frac{\alpha_{10}}{1+j\frac{f}{f_{c1}}}\left(1+\frac{K_1\alpha_{20}}{1+j\frac{f}{(f_{c2}/K_2)}}\right) \tag{10}$$

$$K_1=\frac{R_3}{r_{e2}+(r_{b2}+R_3)(1-\alpha_{20})+R_4}$$

$$=\frac{1}{\alpha_{20}}\left(\frac{\alpha_0}{\alpha_{10}}-1\right) \tag{11}$$

$$K_2=\frac{r_{e2}+r_{b2}+R_3+R_4}{r_{e2}+(r_{b2}+R_3)(1-\alpha_{20})+R_4}$$

$$=1+K_1\left(1+\frac{r_{b2}}{R_3}\right) \tag{12}$$

where

$\alpha_0$: values of $\alpha$ at low frequencies.

When $R_3(1-\alpha_{20})\gg r_{e2}, R_4, r_{b2}(1-\alpha_{20})$ is assumed, then

$$K_1\fallingdotseq K_2=\frac{1}{1-\alpha_{20}} \tag{13}$$

And if $f_{c1}$ and $f_{c2}$ are assumed to be identical,

$$\alpha=\frac{\alpha_0}{1+j\frac{f}{(\alpha_{10}/\alpha_0)f_{c1}}} \tag{14}$$

$$\alpha_0=\frac{\alpha_{10}^2}{1-\frac{\alpha_{20}R_3}{r_{e2}+R_3+R_4}} \tag{15}$$

From Equation (10), $|\alpha|$ becomes

$$|\alpha|=\left(\frac{\alpha_{10}^2}{1+\left(\frac{f}{f_{c1}}\right)^2}\left\{1+\frac{K_1\alpha_{20}(K_1\alpha_{20}+2)}{1+\left(\frac{f}{f_{c2}/K_2}\right)^2}\right\}\right)^{\frac{1}{2}} \tag{16}$$

This equation shows that $|\alpha|$ approaches $|\alpha_1|$ with increase in frequency.

In Fig. 4, the experimental values of $|\alpha|$ are shown compared with curves calculated from the above equations.

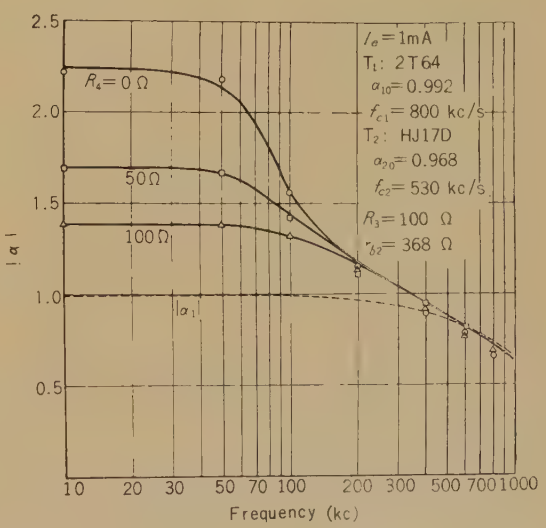


**Fig. 4**—Experimental (○ □ △), and calculated (solid line) values of $|\alpha|$.

### 1.3. Static Characteristics and their Variation with Temperature

As mentioned above, the current amplification factors of the three terminal compound transistors may be larger than unity and they may be suitable for use in bistable switching circuits and negative resistance circuits similar to those used for point contact transistors. Fig. 5 (a) shows a switching circuit for speech-path switches. When $R_3$ and $R_4$ are sufficiently small compared with the collector impedance of the compound transistor, the relation of small signal input voltage $v_e$ and current $i_e$ in the active region may be expressed approximately as follows:

$$v_e = \{r_e + (1-\alpha)R_2\} i_e. \qquad (17)$$

Therefore the input resistanse is negative in the range of $(\alpha-1)R_2 > r_e$.

In the cutoff region, the input impedance of the circuit is determined by the reverse impedances of emitter and collector sides, and it becomes several megohms in the voice frequency range when $T_1$ and $T_2$ are low-frequency alloy junction transistors. In the saturation region, the emitter to collector impedance shows a very low value depending upon $R_3$ and $R_4$, for example several tens of ohms.

Fig. 5 (b) shows the experimental results of the circuit in Fig. 5 (a) when $R_L$ is zero. The peak point $(V_p, I_p)$ and the valley point $(V_v, I_v)$ are given approximately by the following expressions:[4]

$$I_p \fallingdotseq 0, \quad V_p \fallingdotseq E_2 - R_2 I_{c0} \qquad (18)^*$$

$$\left.\begin{aligned} I_v &\fallingdotseq \frac{E_2}{R_2(\alpha-1)+(r+R_L)\alpha} \\ V_v &\fallingdotseq \left\{1 - \frac{R_2(\alpha-1)-r_e}{R_2(\alpha-1)+(r+R_L)\alpha}\right\} E_2. \end{aligned}\right\} \qquad (19)$$

In these equations, $I_{c0}$ is the dark current flowing from collector $C$ to base $B$ of the circuit, and is most sensitive to temperature.

As shown in Equation (18), $I_{c0}$ reduces the peak point voltage, and therefore decreases the circuit stability. In the case where $R_3$ is not zero, $I_{c0}$ may become larger than $I_{c01}+I_{c02}$ which is the sum of the dark current of the each transistor, because the emitter current of $T_2$ originates from the voltage drop in $R_3$ when $I_{c01}+I_{c02}$ flows through it.

Fig. 6 shows the experimental result of the relation between $I_{c0}$ and $R_3$ when the

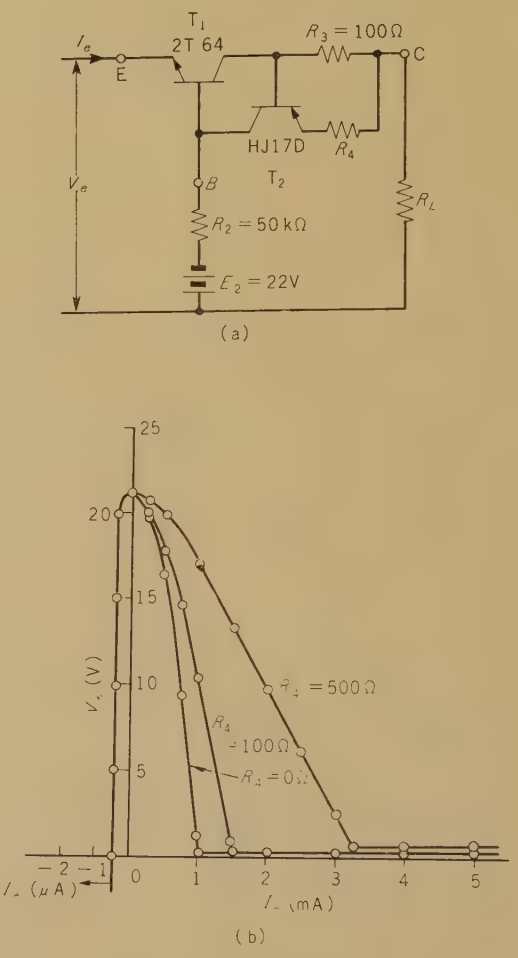


**Fig. 5**—Switching circuit for speech-path switches (a), and its static characteristics when $R_L$ is zero (b).

* More precisely, the peak point occurs when $r_e+(1-\alpha)R_2$ becomes zero, and $V_p$ and $I_p$ are both somewhat larger than the values of Equation (18).

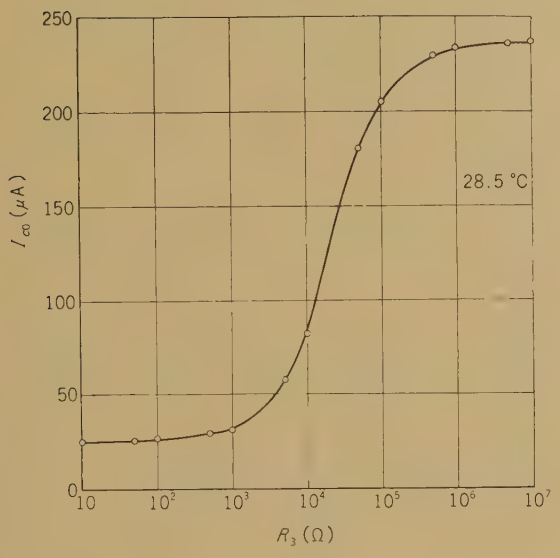


**Fig. 6**—Relation between $I_{c0}$ and $R_3$. ($R_4=100\Omega$)

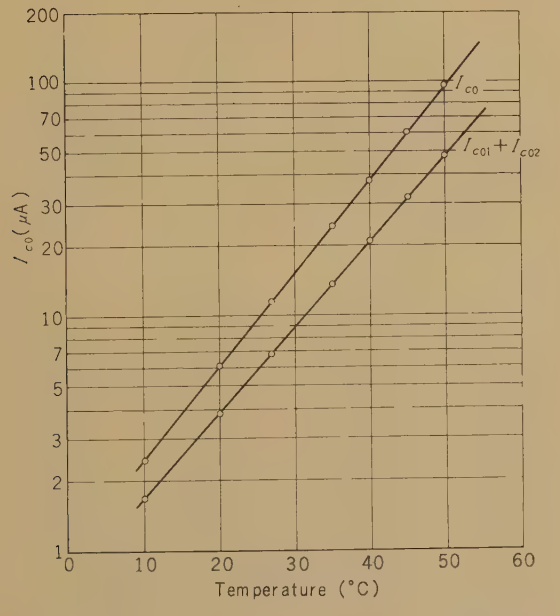


**Fig. 7**—Variation of $I_{c0}$ with temperature. ($R_3=R_4=100\Omega$)

circuit of Fig. 5 (a) is in the cutoff region; and the variation of $I_{c0}$ with temperature is given in Fig. 7 comparing that of $I_{c01}+I_{c02}$. The circuit may be used at temperatures under 40° C for speech-path switches.

### 1.4. Switching Characteristics

Approximate calculations for the circuit shown in Fig. 8 (a) may be worked out as follows:

For simplification, it is assumed that the base resistances of $T_1$ and $T_2$ are zero, cutoff frequencies of both transistors are identical, and the external base resistance $R_2$ is sufficiently small compared with the collector impedance of the compound transistor. Then

$$\left.\begin{aligned}\alpha&=\frac{\alpha_0}{1+j\dfrac{f}{(\alpha_{10}/\alpha_0)f_{c1}}}\\ \alpha_0&=\frac{\alpha_{10}}{1-\dfrac{\alpha_{20}R_3}{r_{e2}+R_3+R_4}}.\end{aligned}\right\}\quad(20)$$

This shows that the calculations may be worked out similar to those for point contact-transistor switching circuits.[5] The minimum amplitude $E_p$ and the minimum pulse width $\tau$, which can switch the circuit from the off to the on state, may be expressed as follows:

$$E_p=\frac{\Delta V}{1-\exp(-\tau/\tau_0)},\quad(21)$$

or

$$\tau=\tau_0 ln\frac{E_p}{E_p-\Delta V}.\quad(22)$$

In these equations,

$$\left.\begin{aligned}\Delta V&=E_2-E_1-R_2I_{c0}\\ \tau_0&=\frac{\alpha_0(R_2+R_1+r_e)}{2\pi f_{c1}\alpha_{10}\{(\alpha_0-1)R_2-R_1-r_e\}}.\end{aligned}\right\}\quad(23)$$

Fig. 8 (b) shows the experimental values and the calculated curves when $R_3$ is 0, 100Ω, and 500Ω. These approximations may be

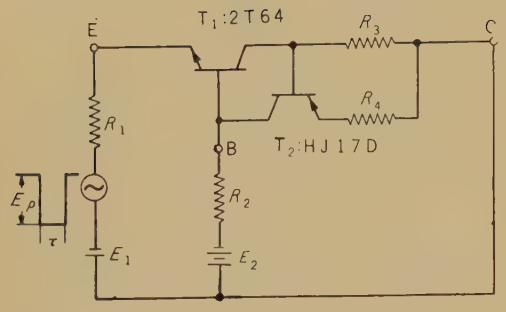


(a)

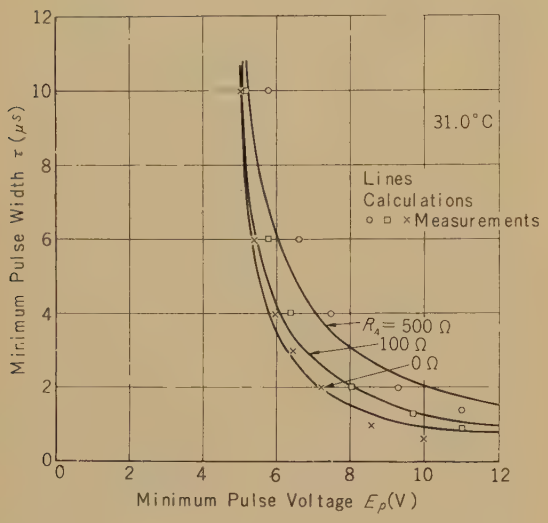


(b)

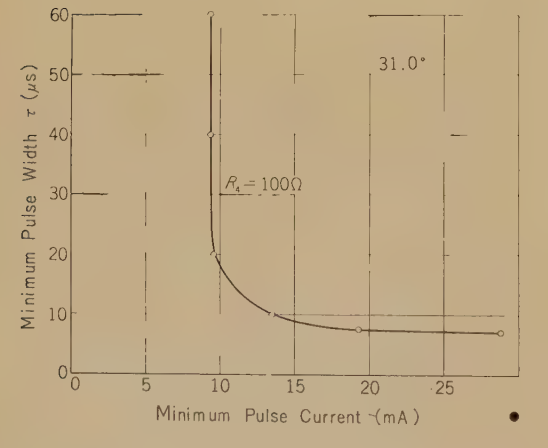


(c)

**Fig. 8**—Compound transistor switching circuit (a), and properties of its control pulses for turn on (b), and turn off (c).

regarded as satisfactory as far as our study is concerned. The turn-off time may be larger than the turn-on time because of carrier storage. Fig. 8 (c) shows the experimental result of the minimum control pulse current and control pulse width which can switch the circuit from the on to the off state.

### 2. Application as Speech-path Switches

As noted above, compound transistors have bilateral low resistivities in the on condition, and their switching ratios (that is, the impedance ratio of the off and the on states) are very high. Furthermore, the breakdown voltages can be fixed with external voltage sources. Therefore they may be expected to be excellent speech-path switches in all-electronic telephone exchange systems.

Fig. 9 shows a speech-path configuration connected with $(n+1)$ cascade stages of compound transistors. The last stages are used for the marking of the trunks and the reset of the speech-paths. When the circuit is expected to turn on, a trigger pulse is impressed on terminal $T_a$, and at the same time a trunk marking pulse is applied to terminal $T_c$ as shown in the figure. Switch $T_b$ may be closed when the circuit is expected to turn off.

In the following sections, the automatic lock-out operations and the properties of the direct cascade connections will be described.

#### 2.1. Principle of Automatic Lock-Out Operations

When switches are arranged in a matrix for speech-path switches, it is necessary that the incoming lines (rows) and the outgoing lines (columns) must be locked out to prevent double connections (that is, to prevent the further connection of other rows and columns to rows and columns that are already connected). Using compound transistors, the lock-outs for the rows may be easily carried out by the voltage drop in a common resistor connected with their direct

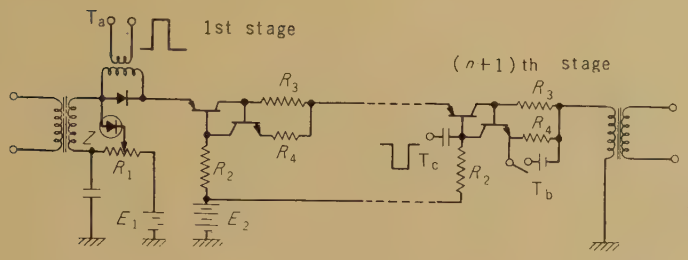


**Fig. 9**—A speech-path configuration of compound transistors.

current source, say $R_1$, in Fig. 9, but the lock-outs of the columns can not be accomplished in the same manner.

The circuit in Fig. 8 (a) has the static characteristics shown in Fig. 5. And in order to switch it from the off to the on state, the emitter voltage should exceed the peak point voltage of the circuit; that is, the sum of $E_1$ and $E_p$ must exceed $E_2 - R_2 I_{c0}$. If the amplitude of the control pulse $E_p$ is held constant, the lock-out may be carried out by changing the location of the peak point. Fig. 10 shows voltage type lock-out characteristics, in which the peak point of curve *a* is shifted to that of curve *b* by applying a higher base voltage $E_2'$ instead of $E_2$.

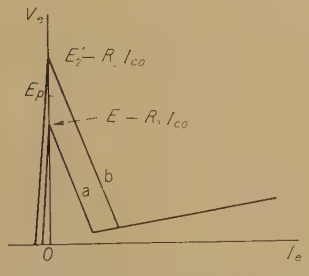


**Fig. 10**—Characteristics of voltage type lock-out.

Fig. 11 shows two current type lock-out configurations. Voltage $E_3$ prevents the npn transistor from active behavior until $I_e$ becomes greater than $E_3/\alpha_1 R_3$. In this case, the change in the static characteristic may be expected as shown in Fig. 12. In this figure the peak point of curve *a* is shifted to that of curve *b* by applying $E_3$ to the terminals shown in Fig. 11.

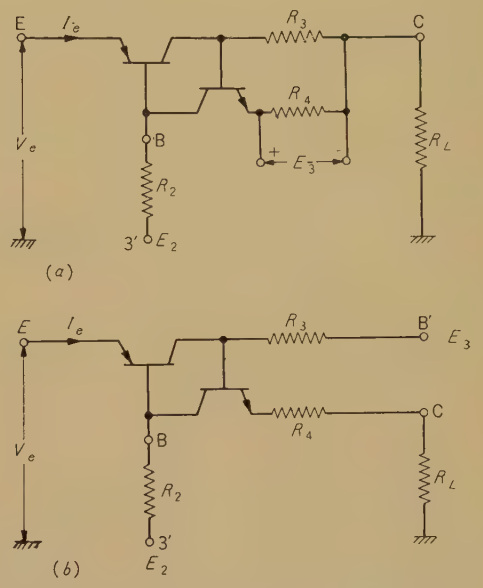


**Fig. 11**—Current type lock-out configurations (a) and (b).

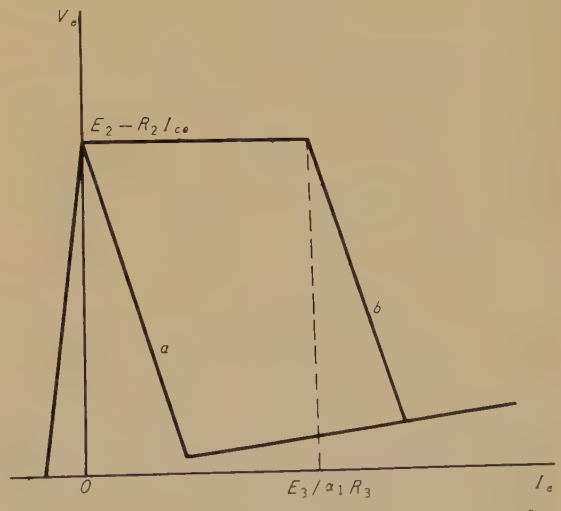


**Fig. 12**—Characteristics of current type lock-out.

### 2.2. Application of Voltage Type Lock-Out to Speech-Path Switches

In practical applications to speech-path switches, the above conditions may be modified for convenience. Fig. 13 shows a speech-path configuration having two incoming lines and an outgoing line, to which the voltage type lock-out is applied. In this figure, A and B are assumed to be identical compound transistors, and $E_2 > E_1$. A negative voltage pulse $E_{p2}$ is applied to terminal 2 and at the same time, a positive voltage pulse $E_{p1}$ is applied to terminal 1 (or 1′). If $E_{p1}, E_{p2} < (E_2 - E_1) < (E_{p1} + E_{p2})$, A (or B) may turn on with coincidence of $E_{p1}$ and $E_{p2}$. When B (or A) is already in the on state, $E_{p2}$ may disappear at the base of A (or B) through the common impedance $z$. Therefore A (or B) can not turn on. Thus the voltage type lock-out may be applied employing two kinds of pulses.

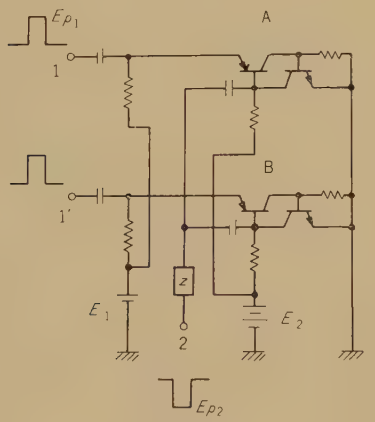


**Fig. 13**—A speech-path configuration employing voltage type lock-out.

### 2.3. The Application of Current Type Lock-Out to Speech-Path Switches

Fig. 14 shows a current type lock-out configuration of speech-path switches having two incoming lines and an outgoing line. When A and B are both in the off state, A (or B) may turn on with a control current pulse $I_p$ at terminal 1 (or 2). When B (or A) is already in the on state and the conductive current $I_B$ (or $I_A$) is flowing through $R_1$ to B (or A), the peak point of the static characteristic of A (or B) may shift to $R_4\ I_{B(\text{or } A)}/(R_3+R_4)$ along the current axis; therefore A (or B) can not turn on unless the control pulse $I_p$ is large enough to exceed the value of $R_4 I_{B(\text{or } A)}/(R_3+R_4)$. This automatic lock-out may be expected to employ a suitable control current pulse amplitude.

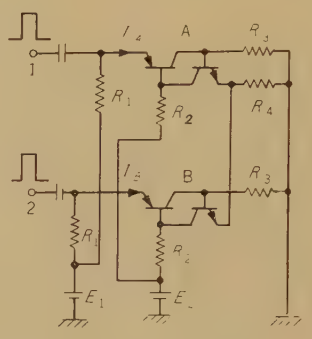


**Fig. 14**—A speech-path configuration employing current type lock-out.

Fig. 15 shows the experimental static characteristics of the circuit shown in the same figure. In the conductive state of A (or B), the impedance between a incoming line and an outgoing line of the circuit may not be so low as that in Fig. 13 because of $R_4$. This effect may be avoided by connecting a diode parallel with $R_3$.

### 2.4. Cascade Connection of Compound Transistors

In the application of compound transistor switches to space-division all-electronic telephone exchanges, cascade connections of the switches may be used in large systems. In this section, characteristics of the three stage cascade connection will be considered.

Fig. 16 shows a three-stage direct cascade of the switches. In the figure, $R_0$'s are

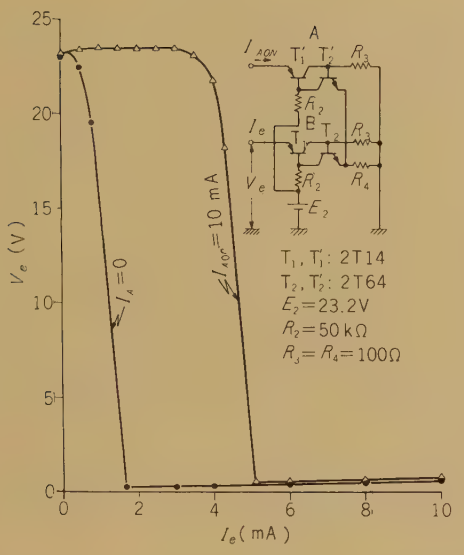


**Fig. 15**—Experimental static characteristics of speech-path configuration employing current type lock-out.

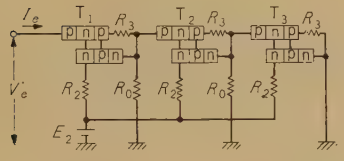

**Fig. 16**—Three-stage direct cascade of the compound transistor switches.

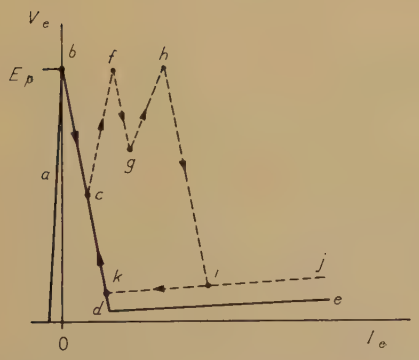

**Fig. 17**—Approximate static characteristics of the circuit shown in Fig. 16.

resistances for by-passing the leakage current of the switches to ground. In Fig. 17, the expected static characteristic of the circuit shown in Fig. 16 is illustrated with dotted line compared with that of the single stage (with solid line). The peak and the valley points ($V$, $I$) in the figure are approximately calculated as below, when the leakage current of the switches is assumed to be zero, and when $|\overline{R}|$ is the value of the negative resistance of the switches.

$$b \cdots\cdots (E_2,\ 0)$$

$$c \cdots\cdots \left(\frac{R_0 \cdot E_b}{R_0+|\overline{R}|},\ \frac{E_b}{R_0+|\overline{R}|}\right)$$

$$f \cdots\cdots \left(E_b,\ \frac{E_b}{R_0}\right)$$

$$g \cdots\cdots \left(\frac{(R_0+\overline{R})\cdot E_b}{R_0+2\overline{R}},\ \frac{2(R_0+|\overline{R}|)\cdot E_b}{R_0(R_0+2\overline{R}|)}\right)$$

$$h \cdots\cdots \left(E_b,\ \frac{2E_b}{R_0}\right)$$

The static characteristic of the multistage connection switch may approach that of the single stage as the $R_0$'s become larger. Similar considerations apply to the switching speed. The Switching properties of the multistage circuit may be considered to be the same as that of a single stage in the case of $R_0=\infty$. If $R_0 \neq \infty$ and is comparatively low, the static and dynamic properties of the multistage connection may be considerably different from those of the single stage, and hysteresis may occur in the static curve as shown in Fig. 17. Fig. 18 shows an experimental verification of the static characteristics described in Fig. 16.

### 3. Two Terminal Configuration

In the foregoing, properties and applications of three terminal compound transistors are discussed. A basic two terminal circuit shown in Fig. 19 (a) may also be applied to speech-path switches in a manner similar to those mentioned above, except that the breakdown voltage may increase in the

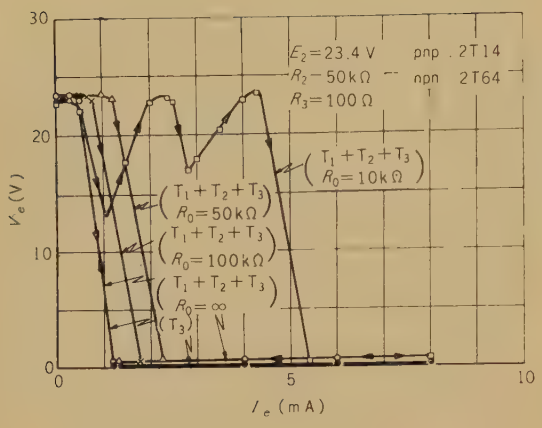


**Fig. 18**—An experimental varification of the static characteristic of the circuit shown in Fig. 16.

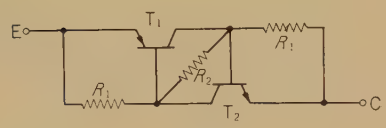


(a)

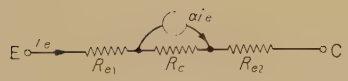


(b)

**Fig. 19**—Basic two terminal compound transistor configuration (a), and its equivalent circuit (b).

case of a multistage connection.

The equivalent circuit may be approximately described as in Fig. 19 (b), and its parameters may be obtained as follows:

$$\alpha=\frac{\alpha_1 R_1}{r_{e1}+(1-\alpha_1)r_{b1}+R_1}+\frac{\alpha_2 R_1}{r_{e2}+(1-\alpha_2)r_{b2}+R_1} \tag{24}$$

$$\left.\begin{aligned} R_{e1}&=\frac{\{r_{e1}+(1-\alpha_1)r_{b1}\}R_1}{r_{e1}+(1-\alpha_1)r_{b1}+R_1} \\ R_{e2}&=\frac{\{r_{e2}+(1-\alpha_2)r_{b2}\}R_1}{r_{e2}+(1-\alpha_2)r_{b2}+R_1} \end{aligned}\right\} \tag{25}$$

$$R_c=\frac{1}{\frac{1}{r_{c1}}+\frac{1}{r_{c2}}+\frac{1}{R_2}}. \tag{26}$$

In these equations, $r_{e1}$, $r_{c1}$, and $\alpha_1$ are emitter resistance, collector resistance, and current amplification factor of $T_1$, and $r_{e2}$, $r_{c2}$, and $\alpha_2$ are emitter resistance, collector resistance and current amplification factor of $T_2$ respectively. From these equations, the voltage and current characteristics are equated as

$$v_e/i_e=R_{e1}+R_{e2}+(1-\alpha)R_c. \tag{27}$$

The value of $v_e/i_e$ can be negative in the case of $\alpha$ being greater than unity. The peak point may occur when the small signal input impedance of the grounded base circuit of $T_1$ or $T_2$ is equal to $R_1$, and the location of the valley point may occur in the case where the direct current input impedance of the same circuit is equal to $R_1$. The experimental results are shown in Fig. 20. The peak point can be fixed with a zener diode as shown in Fig. 21.

In speech-path use, the automatic lock-out function may be obtained with a series connection of a resistance to the emitter of $T_2$ common to the columns of the matrix in a manner similar to those mentioned in the case of the three terminal switches.

## Conclusion

The circuit properties of compound transistors have been examined for applications as speech-path switches. When low-frequency junction germanium transistors are employed, the following characteristics may be realized:

Very low impedance (several to several tens of ohms) in the on state, and very high impedance (several to several tens of megohms) in the off state, are obtained.

Holding voltage and current of the on state can be low (less than 1 volt and less than 1 ma), and the power consumption

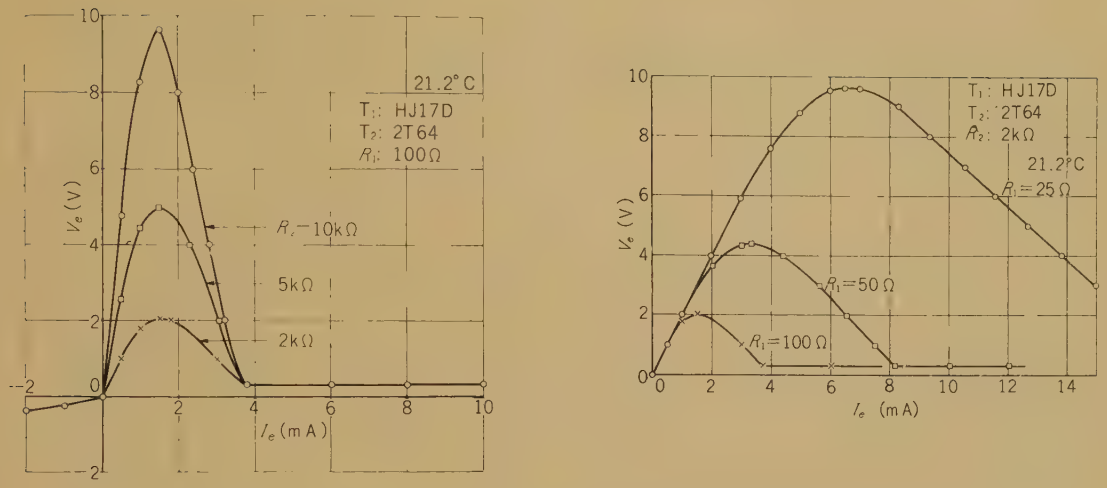


**Fig. 20**—Experimental static voltage-current characteristics of the two terminal compound transistor shown in Fig. 19 (a).

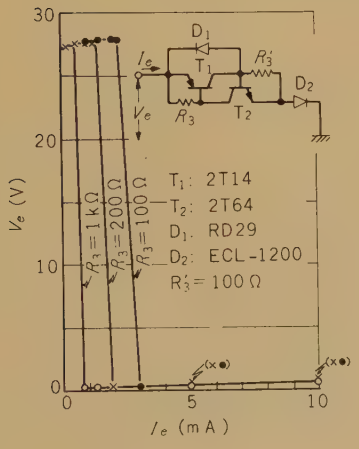


**Fig. 21**—Experimental static voltage-current curves of the two terminal compound transistor with a zener diode $D_1$.

may be very small (about 10 mW in the on state and several $\mu$W in the off state).

The breakdown voltage can be fixed with an external voltage source, and it remains constant in the case of multistage cascade connections.

Automatic lock-out functions may be easily provided for speech-path switches. From a technical viewpoint, the compound transistors may be found to be excellent devices for speech-path switches in all-electronic telephone exchange systems.

They may be also used for negative resistance circuits and their properties may be modified with additional elements. Therefore, wide applications may be expected, for example, to bilateral amplifiers, to oscillators, and to circuits for the compensation of speech-path losses.

**References**

(1) J. L. Moll, M. Tanenbaum, J. M. Goldey and N. Holonyak, "P-N-P-N Transistor Switches," *Proc. I.R.E.*, **44**, 9, p. 1174, 1956.
(2) I. Endo and S. Yoshida, "Semiconductor Speech-Path Switches Suitable for Direct Coupled Connection," Review of the Electr. Comm. Labor. N.T.T., **8**, No. 3-4, p. 105, 1960.
(3) J. J. Ebers, "Four Terminal P-N-P-N Transistors," *Proc. I.R.E.*, **40**, 11, p. 1361, 1952.
(4) L. P. Hunter, *Handbook of Semiconductor Electronics*, McGraw-Hill Co., p. 15–10, 1956.
(5) L. L. Lebow and R. H. Baker, "The Transient Response of Transistor Switching Circuits," *Proc. I.R.E.*, **42**, 6, p. 938, 1954.

* * * *

621. 371. 029, 6:621. 812. 62:621. 381. 812. 4

# Characteristics of Beyond-Horizon Propagation Over Sea (I)*

*Tadasu FUKAMI*† *Seiji IEIRI*‡ *Fumio IKEGAMI*‡ *Hirofumi FUJIMURA*‡

*This paper describes the results of propagation tests carried out for about one year from October, 1957, to August, 1958, on beyond-horizon over-sea paths between Miyazaki, Muroto-misaki, and Wakayama. General descriptions of the tests and the equipments used are presented: diurnal, day-to-day, and seasonal variations, as well as distributions of the median field intensity; comparison of the measured values with those predicted by conventional theories and empirical propagation curves; and relations of the median signal strength to frequency and distance.*

*It is pointed out by comparison with the results of the meteorological observations that the seasonal variation of the received field intensity is correlated with that of the refractive index of the atmosphere at the earth's surface; and that an enhancement in the field intensity is related to an abrupt change in the refractive index of the atmosphere.*

## Introduction

It has been recognized that communication links utilizing tropospheric beyond-horizon propagation is of a large significance for the future communication-network program of the N.T.T.; thus a plan was made to perform propagation tests to investigate the characteristics of beyond-horizon propagation. Over-sea paths were chosen for the propagation tests, partly because the geographical conditions of this country frequently require practical use of over-sea links; and partly because a simple path profile makes easy the analysis of the data obtained.

Planning of the test and preparation of equipments such as antennas, transmitters, and receivers started in August, 1956. The tests were carried out four times, each for about one month in each season of the year:

1st test (autumn): October 10 – November 5, 1957.
2nd test (winter) : January 29 – February 18, 1958.
3rd test (spring) : April 26 – May 22, 1958
4th test (summer): July 18 – August 15. 1958.

A large amount of data obtained from these observations was analysed to give a more or less clear picture of the problem.

* MS in Japanese received by the Electrical Communication Laboratory, Feb. 15, 1959. Originally published in the *Electrical Communication Laboratory Technical Journal*, Vol. 8, No. 6, pp. 714–759, 1960.
† Radio Section.
‡ Radio Propagation Research Section.

## 1. Outline of Tests

### 1.1. Propagation Paths

The test paths are entirely over the sea one transmitting and two receiving points, being located nearly on a straight line as shown in Fig. 1. The path profile is shown in Fig. 2, in which the half-power beam width in the free space, of a 5m × 5m antenna, is illustrated for two frequencies.

### 1.2. Items of Tests

The problems of beyond-horizon propagation may roughly be classified as follows:

(i) characteristics of the received field intensity,
(ii) characteristics of the available frequency

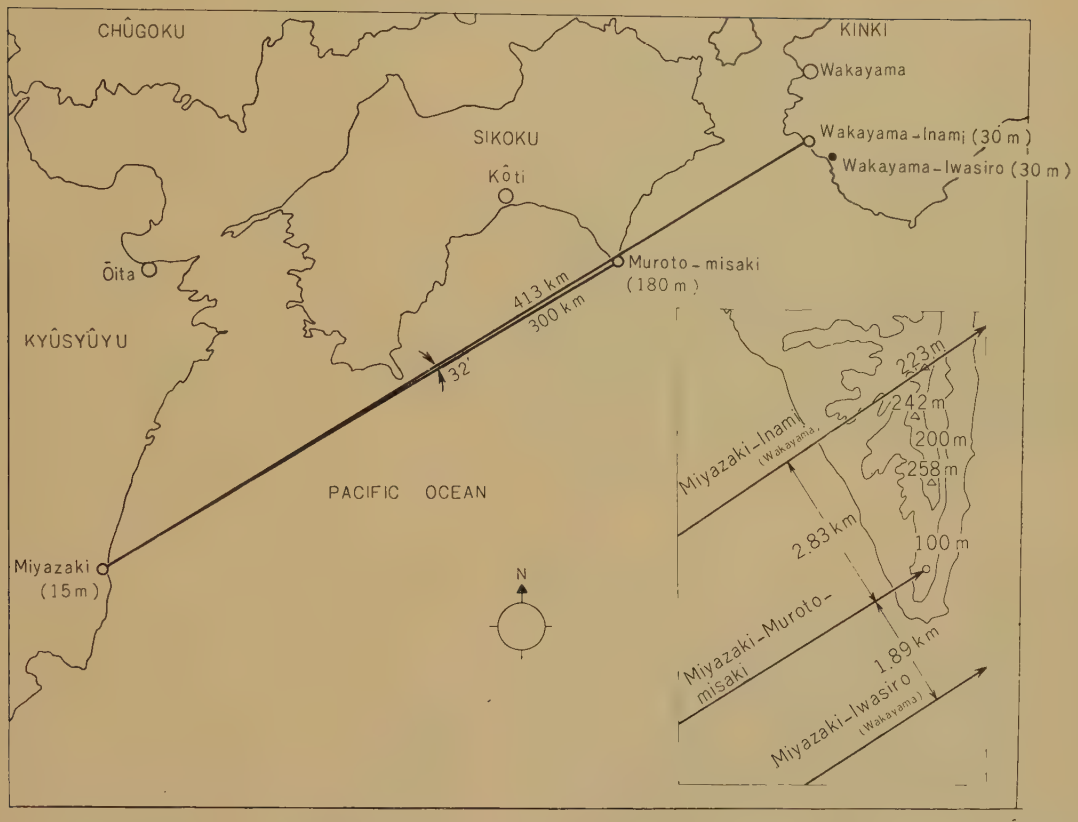


**Fig. 1**—Map of propagation paths.

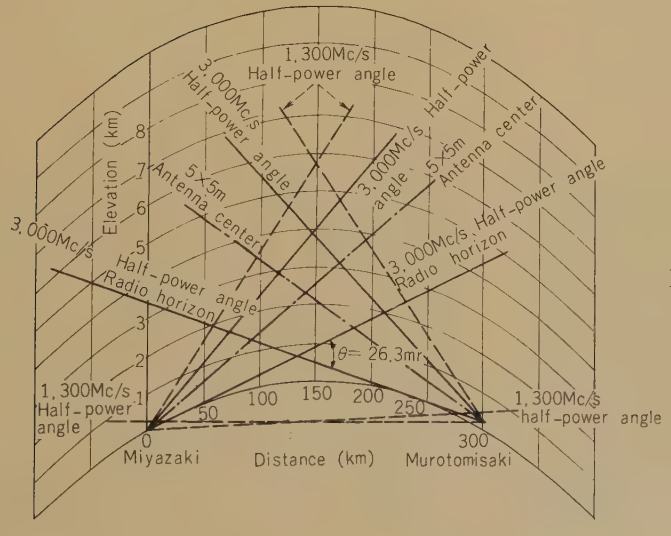


**Fig. 2 (a)**—Path geometry showing the intersection of half-power beam angles of the 5 m × 5 m antennas. 4/3 earth's radius.

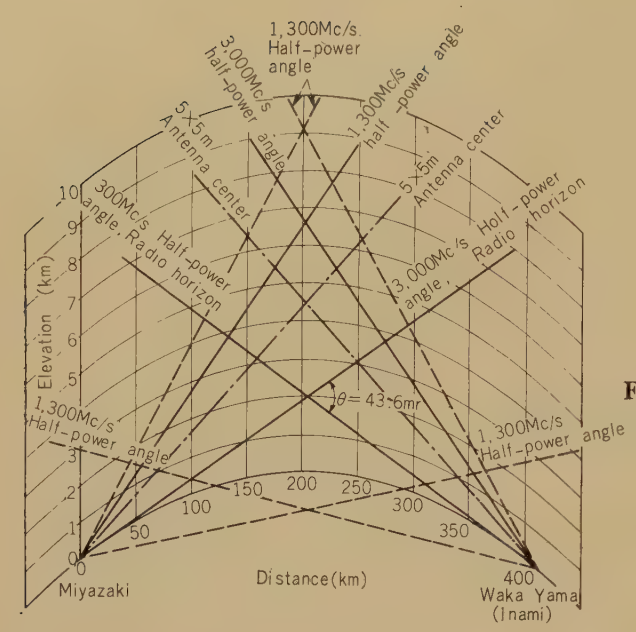


**Fig. 2 (b)**—Path geometry showing the intersection of half-power beam angles of the 5 m×5 m antennas. 4/3 earth's radius.

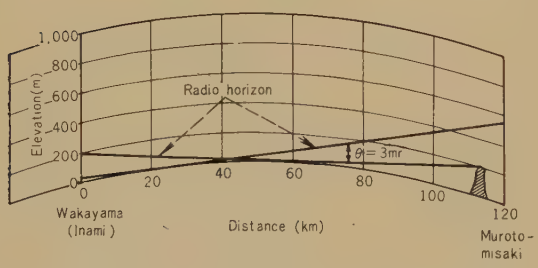


**Fig. 2 (c)**—Path profile from Inami to Muroto-misaki. 4/3 earth's radius.

bandwidth, and

(iii) mechanism of propagation, in particular, its relation to meteorological phenomena.

Out of these three, attention was paid chiefly to items (i) and (iii) as the first step, in view of the equipments available for these tests. The items aimed at are as follows:

(1) Continuous reception with fixed antennas:
distribution of instantaneous field intensity,
seasonal variation of median field intensity,
fading range and fading rate,
relation of the field intensity to distance and scatter angle,
relation of the field intensity to frequency.

(2) Measurements of horizontal and vertical space correlation of instantaneous field intensity.

(3) Comparative measurements of field intensity with various combinations of antenna apertures.

(4) Measurements of effective gain and modified pattern of antenna.

(5) Photographic records of received pulse shape for various propagation conditions and for various combinations of antenna apertures.

(6) Measurements of antenna height pattern (at Muroto-misaki only).

(7) Influence of the waves reflected from flying airplanes on the propagation, for the purpose of analysis of the propagation mechanism (in the 2nd and 4th tests).

(8) Relations of the field intensity to surface meteorological data and aerological data (by radiosonde).

(9) Radiometeorological observations in the lower atmosphere, and the relation of observed data to field intensity (in the 3rd and 4th test at Muroto-misaki).

(10) Comparative observations of the propagation on an open over-sea and an ob-

structed paths (at Inami and Iwasiro, 3rd test only).

(11) Comparative observations of the changes in field intensity with polarization.

### 1.3. Equipments

The 1,300 Mc/s- and 3,000 Mc/s-transmitters used in these tests are equipped with a magnetron oscillator modulated by a pulse of 0.5 microseconds in width at a repetition rate of 2 kc/s, the peak power output being of 500 kw. The pulse width as narrow as 0.5 microseconds was used for the purpose of discriminating the delayed waves, in order to investigate the frequency band capability as well as the mechanism of propagation.

The 5m × 5m antenna used in the tests is shown in Fig. 3, a view of the Muroto-misaki station. Fig. 4 shows the structure of the radiators, for which was used a common reflector.

The receiver was provided with a level counter, a high-speed three-element recorder and a movie camera for recording the pulse shape. The maximum sampling rate of the level counter is of 32 c/s. Samples are recorded by each register corresponding to the sample level, at the stepped-down rate of 4 c/s, obtaining the exact cummulative distribution of instantaneous field strength even for very rapid fadings peculiar to propagation beyond the horizon. The camera films the whole set of registers automatically every hour. Fig. 5 gives the front view of the level counters including the registers.

The high-speed recorder simultaneously records three signals on the same recording chart which travels at a maximum speed of 2 cm/s to ensure a good response to rapid variations in the received signal strength. This recorder was used for the measurements of fading rate and short-term distribution of field intensity, for the simultaneous measurements of cross- and auto-correlations, as well as for the comparison of instantaneous field strength with the received pulse shape. The pulse shape recording device consists of a synchroscope and a 16 mm movie camera. The former displays the received pulse shape,

**Fig. 3**—View of Muroto-misaki Station.

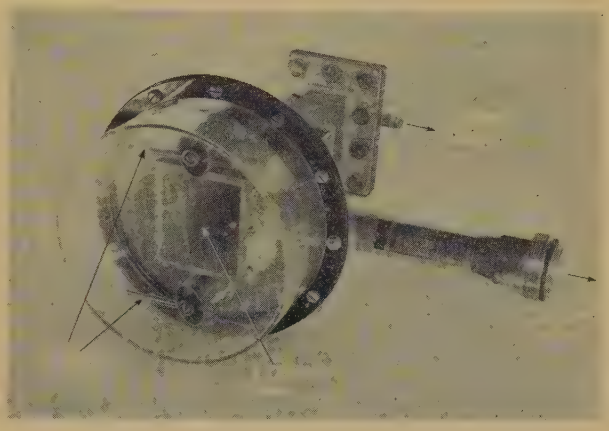

**Fig. 4**—1,300 Mc/s- and 3,000 Mc/s-primary radiator of 5 m × 5 m paraboloidal antenna.

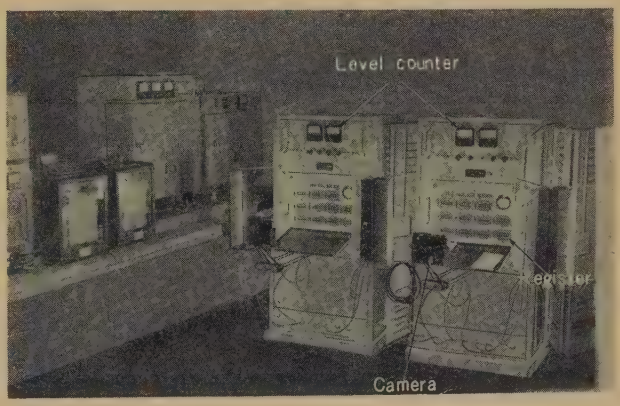


**Fig. 5**—Lever counter.

**Table**

PROPAGATION TEST

| | Mark | Test Path | | Frequency (Mc/s) | Distance (km) | Transmitting Antenna Height (m) | | Receiving Antenna Height (m) | |
|---|---|---|---|---|---|---|---|---|---|
| | | Transmitter | Receiver | | | Above Sea Level | Above Ground | Above Sea Level | Above Ground |
| 1 | 250 Mc/s | Wakayama | Muroto-misaki | 254.6 | 113 | 30 | 20 | 180 | 20 |
| 2 | 970 Mc/s | Wakayama | Muroto-misaki | 970 | 113 | 30 | 5 | 180 | 20 |
| 3 | 50 Mc/s | Miyazaki | Muroto-misaki | 48.71 | 300 | 15 | 10 | 180 | 8 |
| 4 | 1,300 Mc/s | Miyazaki | Muroto-misaki | 1310 | 300 | 15 | 5 | 180 | 5 |
| 5 | 3,000 Mc/s | Miyazaki | Muroto-misaki | 2995 | 300 | 15 | 5 | 180 | 5 |
| 6 | 1,300 Mc/s | Miyazaki | Wakayama | 1310 | 413 | 15 | 5 | 30 | 5 |
| 7 | 3,000 Mc/s | Miyazaki | Wakayama | 2995 | 413 | 15 | 5 | 30 | 5 |

i) At the 1st test (autumn) 197.12 Mc/s was used instead of 250 Mc/s. ii) Transmitting and

while the latter films them at a rate of 64 frames per second. The measured pulse shape, particularly the distortion and the broadening in pulse width were carefully analysed to investigate the multi-path propagation.

At Muroto-misaki, space correlations were measured by moving one of a pair of receiver sets in horizontal and vertical directions, along the track and the duralumin tower shown in Fig. 3.

Fig. 6 gives the block diagram of the whole measuring system, and Table 1 summarizes the characteristics of transmitters, receivers and antenna.

For radiometeorological observations in the lower atmosphere, six pairs of dry and wet-bulb thermometers were installed at various heights ranging from the sea surface up to 210 meters above the sea level. Air temperature and humidity at each height were remote-recorded. For observations in the higher atmosphere, a drop radiosonde was used in order to measure air temperature, humidity and pressure up to the height of 5,000 or 7,000 meters above the sea level; Fig. 7 illustrates its structure. This radiosonde is designed to be released from the balloon at a predetermined height by means of a pressure-controlled relay, and to descend on a parachute.

## 2. Characteristic of the Median Received Field Intensity

### 2.1. Treatment of Data.

The received signal in beyond-horizon propagation is characterized by the composite form of fading in which rapid fadings superimpose on a long-term slow fading. Some authors reported that the hourly median value of the field intensity with slow fading is subject approximately to the dB-nomal distribution, while the distribution of the instantaneous field intensity with rapid fadings can be approximated by the Rayleigh-distribution if variations in small intervals of time is considered.[1]

For the long-term distributions of instantaneous field intensity, Norton and others proposed a distribution as determined by the combination of a constant vector and Rayleigh-

1

FACILITIES

| Scatter Angle (mr) | Transmitting Antenna | | Receiving Antenna | | Transmitter | | Receiver | |
|---|---|---|---|---|---|---|---|---|
| | Type | Gain (dB) | Type | Gain (dB) | Power | Remarks | Noise Figure (dB) | Band-Width (Mc/s) |
| 2.9 | Yagi, 4 elements | 10.0 | Yagi, 4 elements | 10.0 | 30 W | CW | 7.3 | 0.455 |
| 3.5 | Paraboloid, 1.8 m dia. | 23.0 | Paraboloid, 1.8 m dia. | 23.0 | 5 kW | Pulse, 4 $\mu s$ | 15 | 2 |
| 26.3 | Yagi, 5 elements | 14.2 | Yagi, 5 elements | 11.2 | 600 W | CW | 8 | 0.03 |
| 26.5 | Paraboloid, 5 m×5 m | 34.8 | Paraboloid, 5 m×5 m | 34.8 | 500 kW | Pulse, 0.5 $\mu s$ | 15 | 6 |
| 26.5 | Paraboloid, 5 m×5 m | 42.7 | Paraboloid, 5 m×5 m | 42.7 | 500 kW | Pulse, 0.5 $\mu s$ | 16 | 6 |
| 43.6 | Paraboloid, 5 m×5 m | 34.8 | Paraboloid, 5 m×5 m | 34.8 | 500 kW | Pulse, 0.5 $\mu s$ | 15 | 6 |
| 43.6 | Pabaraloid, 5 m×5 m | 42.7 | Paraboloid, 5 m×5 m | 42.7 | 500 kW | Pulse, 0.5 $\mu s$ | 15 | 6 |

receiving antenna gains are expressed by free space gains in decibels relative to an isotropic antenna.

distributed vectors.[2]

Analysis of our data reveals, however, that the distributions are not always normal nor of the Rayleigh type. They depend in fact on distance, frequency and the season of the year.

To obtain long-term distributions, many a writer use hourly medians instead of instantaneous values of the received field intensity. It is chiefly because the measurement of instantaneous field intensity involves practical difficulties, such as requiring the small time constant of recorders and troublesomeness in statistical treatment, on account of the very rapid fadings involved. We minimized such difficulties by use of the level counter mentioned above.

In view of the practical design of radio links, it is necessary to use the distribution of instantaneous field intensities for the precise estimation of the time percentage of deep fades. This also meets the recommendation by the CCIR to establish the transmission standards on the basis of the average of the instantaneous field intensity over a short period of one minute.

### 2.2. Expression for Field Intensities

For expressing the measured and the calculated field intensities, it is convenient to use the concept of "basic transmission loss" defined for ideal isotropic antennas.[3] For converting the transmission loss into the basic transmission loss, use of the effective antenna gain is necessary, which is given by reducting the antenna aperture-to-medium coupling loss from the free space antenna gain.

The coupling loss can be experimentally determined in principle by comparing the signal strength received by use of the antenna in question with that received using a practically small-sized antenna. On the other hand, formulas for the coupling loss, based on the scatter theory, have been given by Booker and deBettencourt,[4] and by Norton.[5] Table 2 shows the coupling loss calculated for the 5m × 5m paraboloidal antenna and for the paths between Miyazaki and Murotomisaki, and between Miyazaki and Wakayama. As is seen in the table, the values computed by the Booker - deBettencourt theory are greater than those computed by Norton's

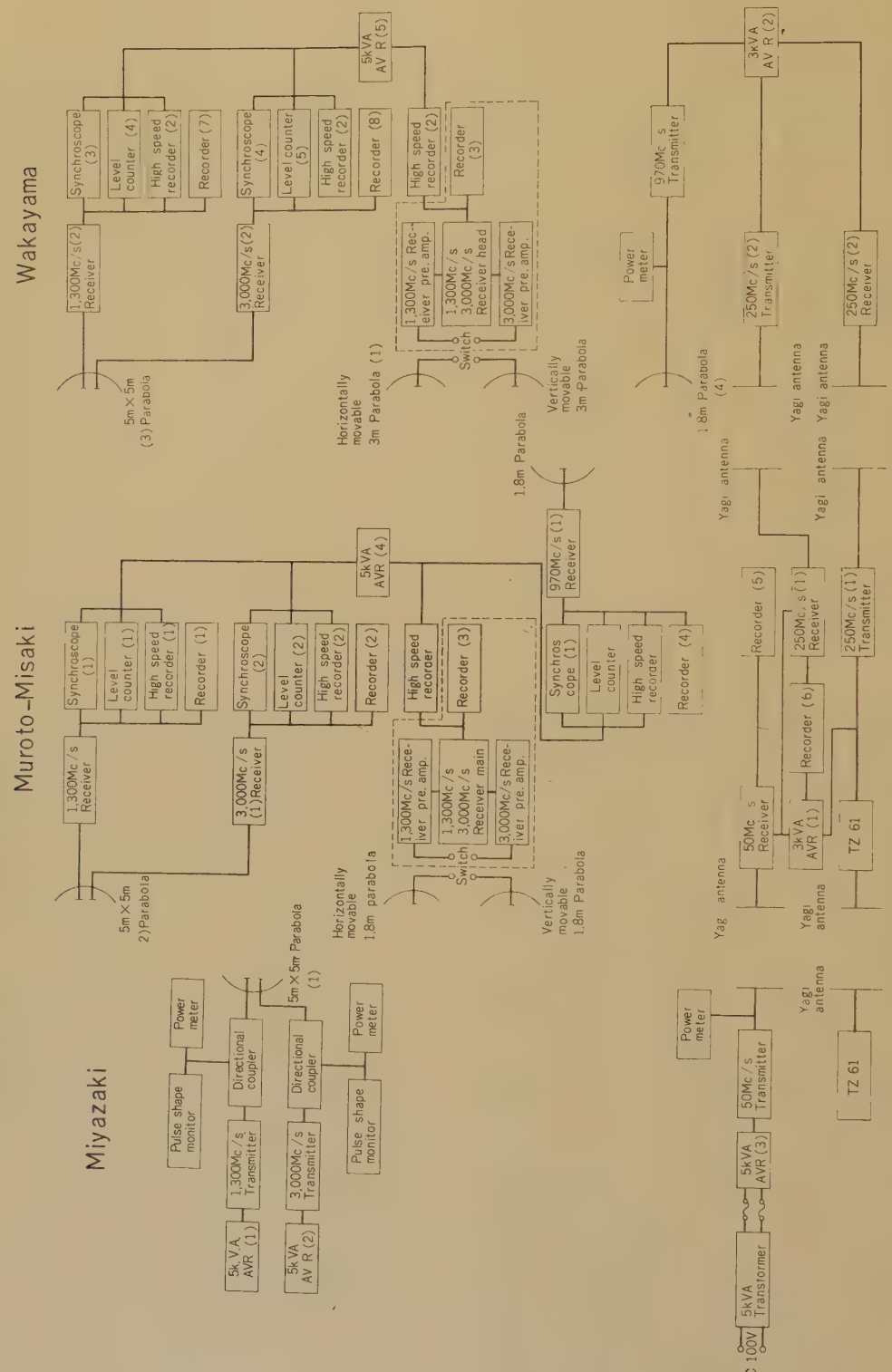


**Fig. 6**—Block diagram of transmitting and receiving system.

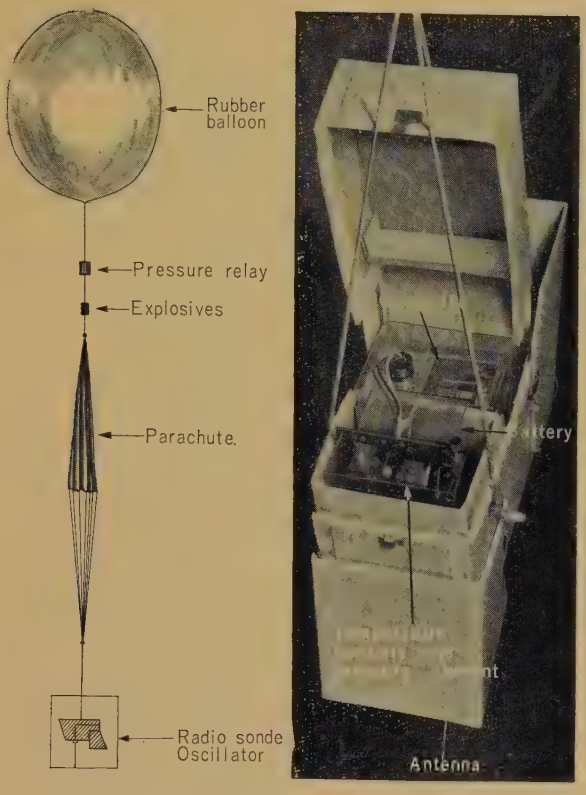


**Fig. 7**—Drop radiosonde.

**Table 2**

ANTENNA-TO-MEDIUM COUPLING LOSS (COMPUTED VALUES)

| Test Path | Frequency (Mc/s) | Booker-deBetencouart | Norton |
|---|---|---|---|
| Miyazaki–Muroto-misaki | 1,300 | 4.5 | 2.5 |
| | 2,000 | 9.7 | 7.5 |
| Miyazaki–Wakayama | 1,300 | 7.7 | 4.0 |
| | 3,000 | 14.4 | 12.0 |

formula, though at present there is no experimental nor theoretical means to decide which is better fitted. In this report, however, the theoretical formula given by Booker and deBettencourt will be used for determining the basic transmission loss, since reliable statistic values are not available for the empirical coupling loss.

### 2.3. Mode of Variations in Received Signals

Fig. 8 - 14 give some samples of the received signals, recorded by conventional recorders at a speed of 24 cm/hour.

On the near-horizon path between Wakayama and Muroto-misaki, the average signals at 250 Mc/s and 97 Mc/s are lowest and most stable in winter. The period of rapid fadings is very small, and the fading range is of about 4.5 dB at 250 Mc/s and of 20 dB at 970 Mc/s. In autumn, the slower fading becomes more conspicuous, the period of rapid fadings being more prolonged than in winter. The average signal level during this season is about 4.5 dB higher than in winter. In spring and summer, rapid fadings almost disappear as shown in Figs. 8 and 9; sometimes appear those variation modes observed in winter and autumn. The mean signal level is about 30 to 40 dB higher in spring and summer than in winter; and in these seasons, there often appears and lasts for several hours a stable state where the fading range is less than several decibels. This stable state was more frequently observed in summer than in spring, and, on these occasions, the signal level at 970 Mc/s reached as high as 2 dB below the free space value (see Figs. 8 and 9).

On the path between Miyazaki and Muroto-misaki, the received signals at 50 Mc/s during all seasons display apparently similar modes of variation, as seen in the samples of Fig. 10. But a careful examination reveals that the period of fadings is smaller in summer than in winter. The average signal level in each season is at its highest in summer and at its lowest in winter; the difference between them being of about 15 dB. At 1,300 Mc/s and 3,000 Mc/s, the average signal levels are stable in winter, spring and autumn; and rapid fadings of about 20 dB are superposed on the average level. This characteristic mode of variation will, in this paper, be referred to as "scatter propagation". Rapid fadings of


**Fig. 8**—Sample records of the signal received on the Wakayama~Muroto-misaki path at 250 Mc/s.

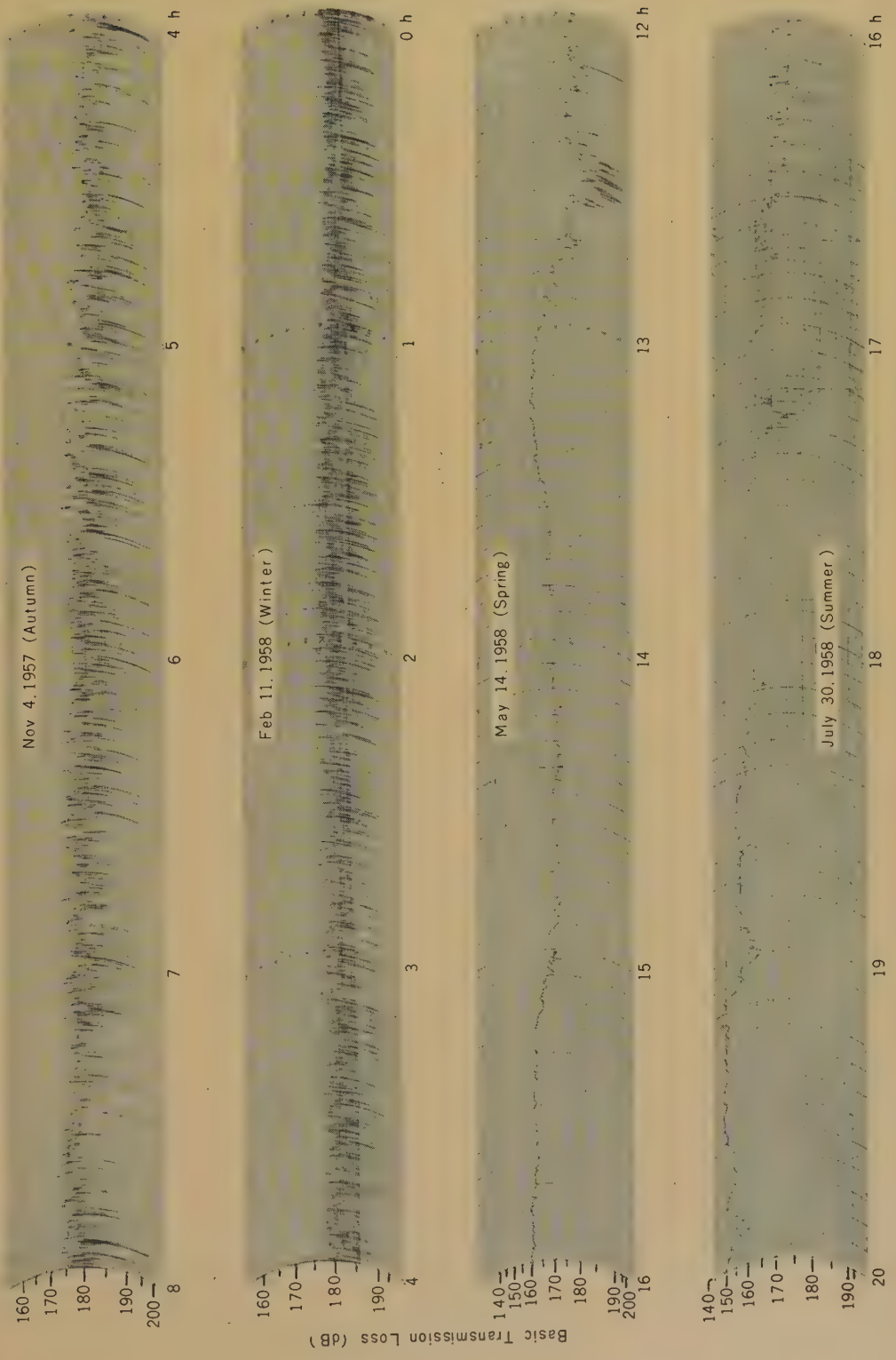


**Fig. 9**—Sample records of the signal received on the Wakayama~Muroto-misaki path at 970 Mc/s.

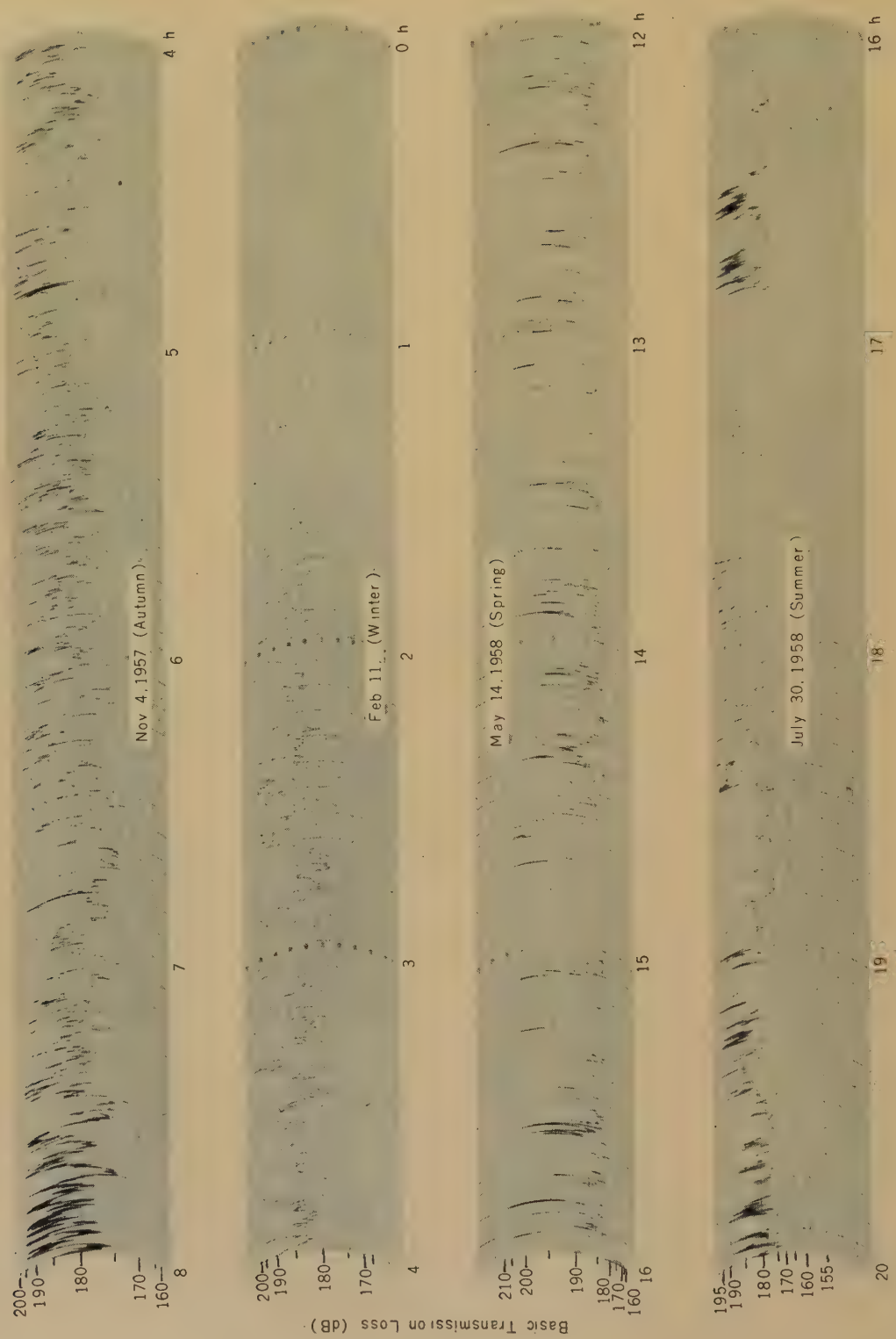


**Fig. 10**—Sample records of the signal received on the Miyazaki~Muroto-misaki path at 50 Mc/s.

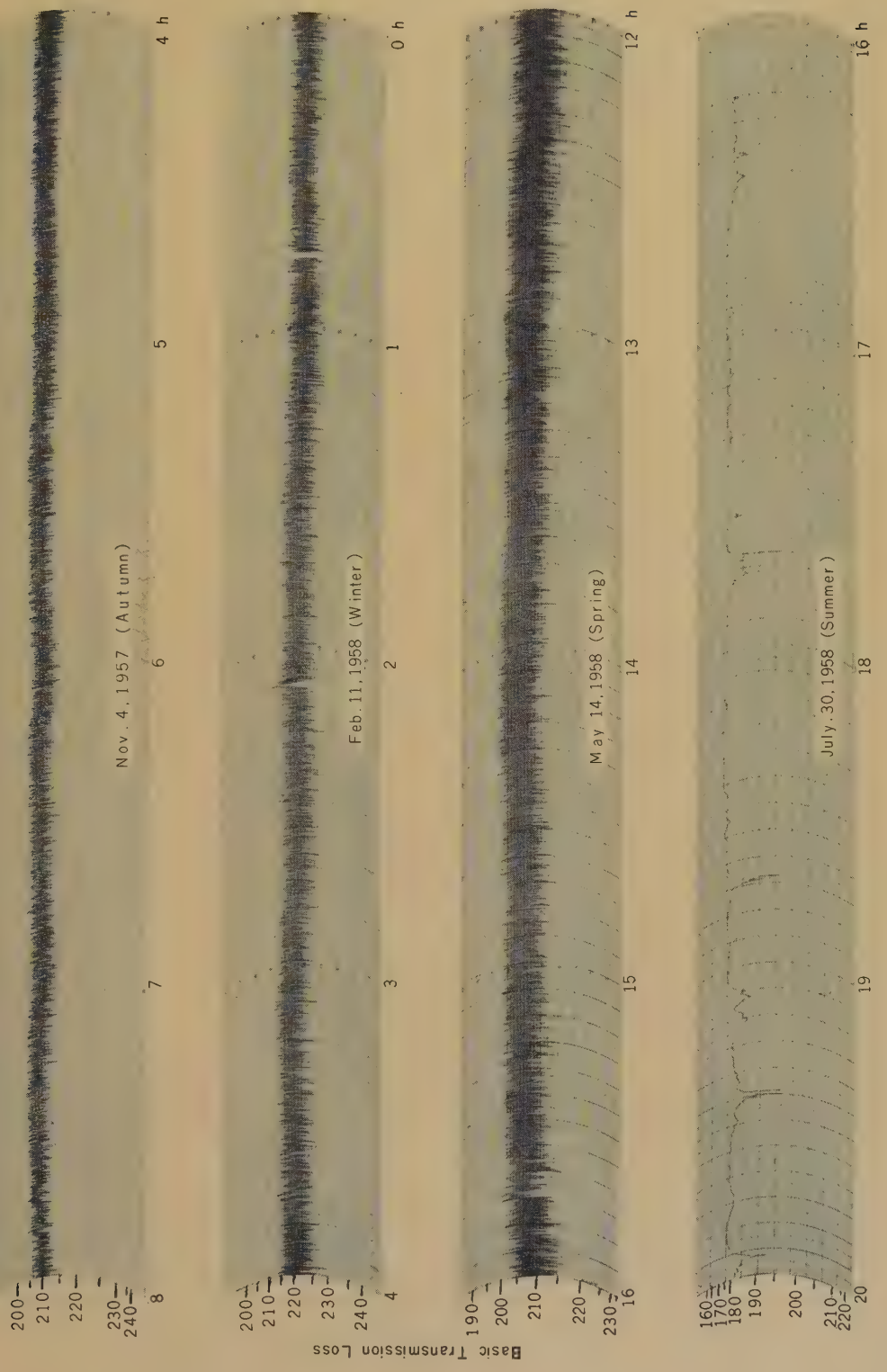


**Fig. 11**—Sample records of the signal received on the Miyazaki~Muroto-misaki path at 1,300 Mc/s.

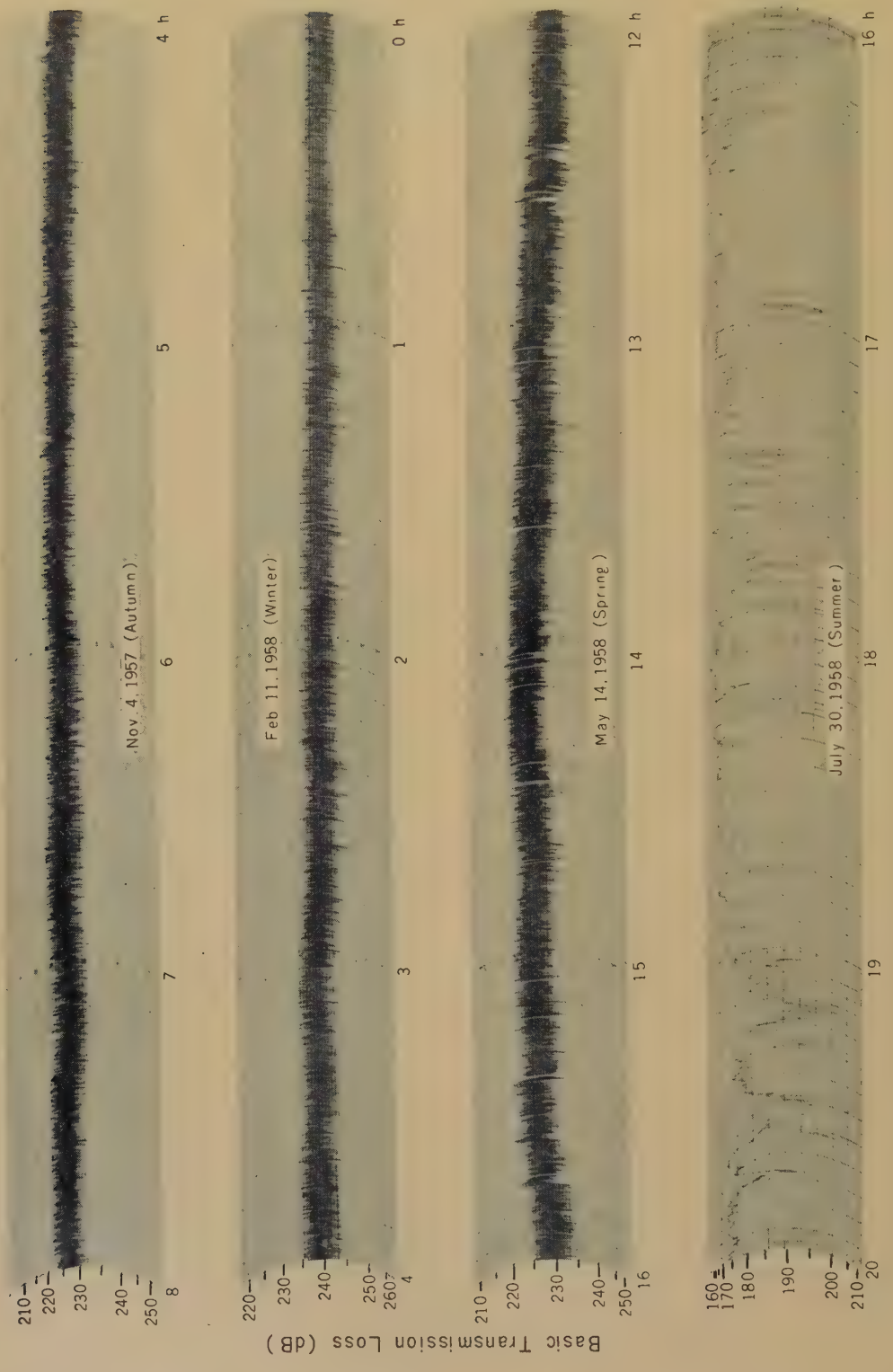


**Fig. 12**—Sample records of the signal received on the Miyazaki~Muroto-misaki path at 3,000 Mc/s.

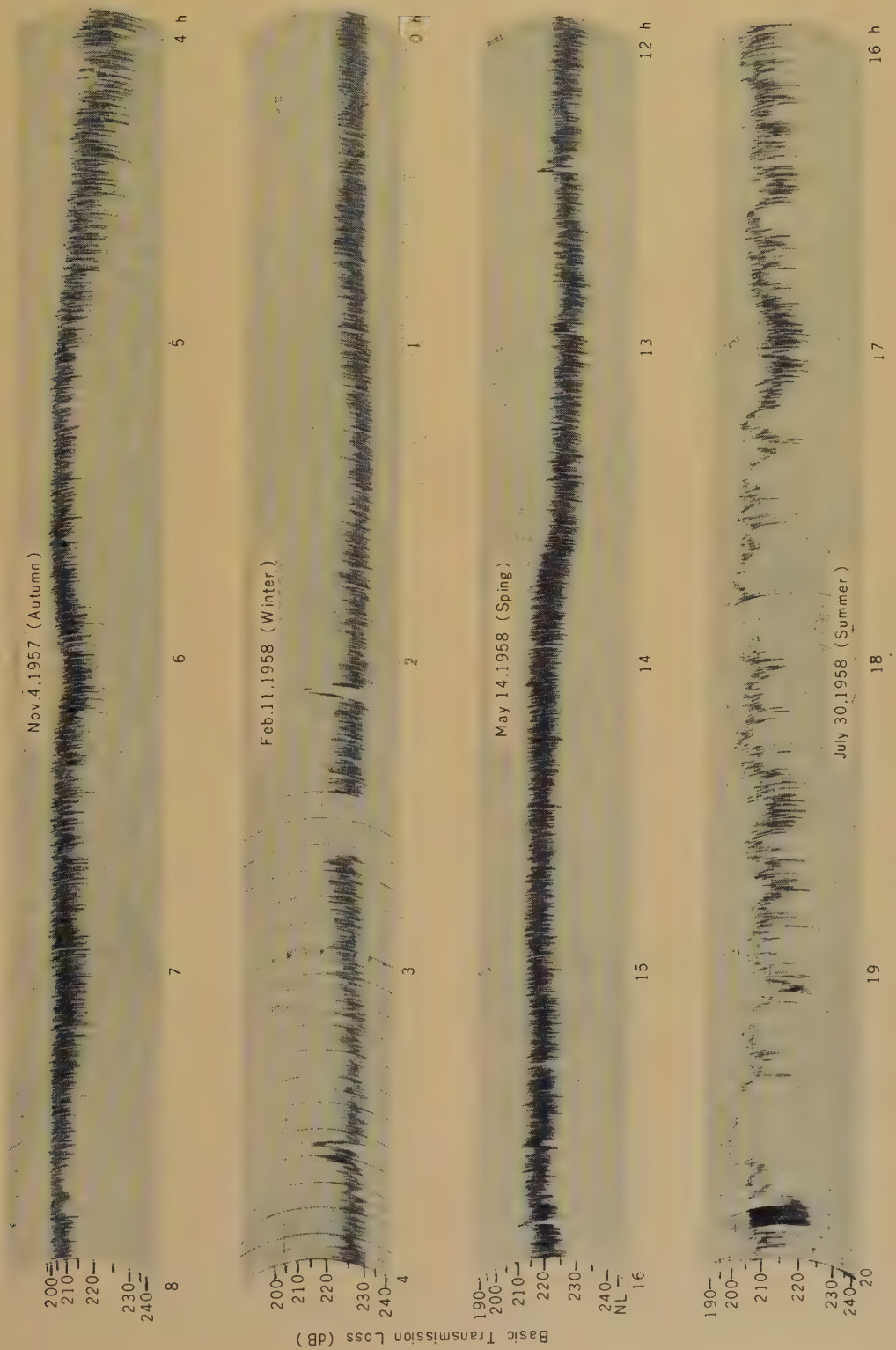


**Fig. 13**—Sample records of the signal received on the Miyazaki～Wakayama path at 3,000 Mc/s.

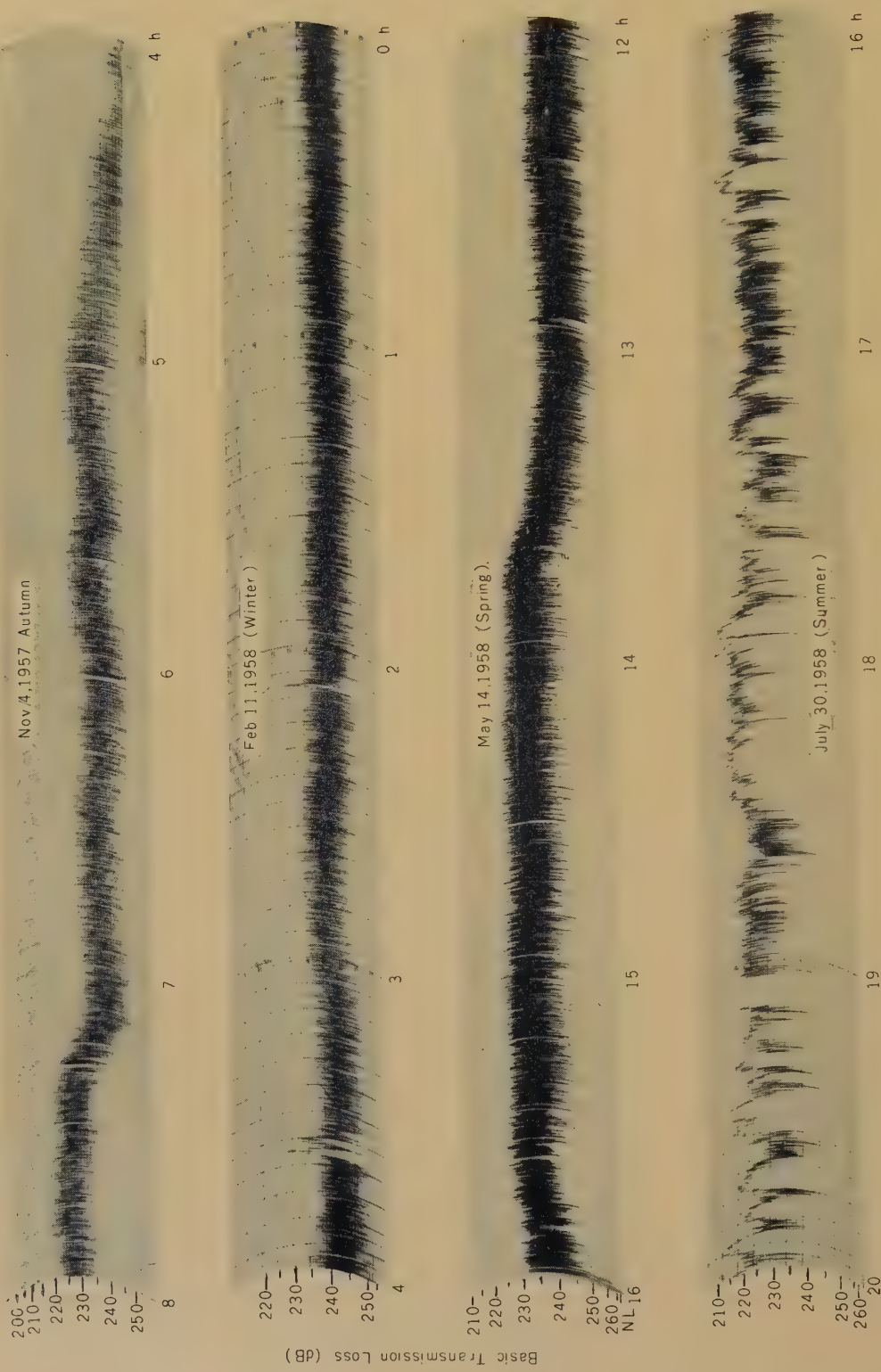


**Fig. 14**—Sample records of the signal received on the Miyazaki～Wakayama path at 3,000 Mc/s.

this mode have the smallest rate of 0.5 c/s at 1,300 Mc/s and 1.2 c/s at 3,000 Mc/s both in winter; while in spring and autumn, the rate is two or three times as high as that in winter. The mean signal level is at its lowest in winter and several decibels higher in spring and autumn. The received signal in summer shows a peculiar mode of variation, as apparent in the samples shown at the bottom of Figs. 11 and 12. The signal level becomes almost constant, fluctuations being within the range of several decibels, and continues so for some hours. This mode of variation is similar to that of the so-called duct propagation. When this type of propagation occurs, the average level becomes several tens decibels higher than that in winter, the maximum levels at 1,300 Mc/s and 3,000 Mc/s reaching 8 and 5 dB below the free space value, respectively.

On the path between Miyazaki and Wakayama, the received signals in winter, in spring, as well as in autumn show the same mode of variation as on the path between Miyazaki and Muroto-Misaki. In winter, the average level is also at its lowest and rapid fadings have the smallest rate of about 0.5 c/s at 1,300 Mc/s, and about 1.0 c/s at 3,000 Mc/s. In spring and autumn, the average level is several decibels higher than in winter, and the rate of rapid fadings is smaller than in winter. In summer, there happens a peculiar mode of variation, in which the signal level increases abnormally as shown in Fig. 13 and 14. However, it occurs less frequently on this path, and when it occurs, it lasts for a shorter time, compared with the path between Miyazaki and Muroto-misaki.

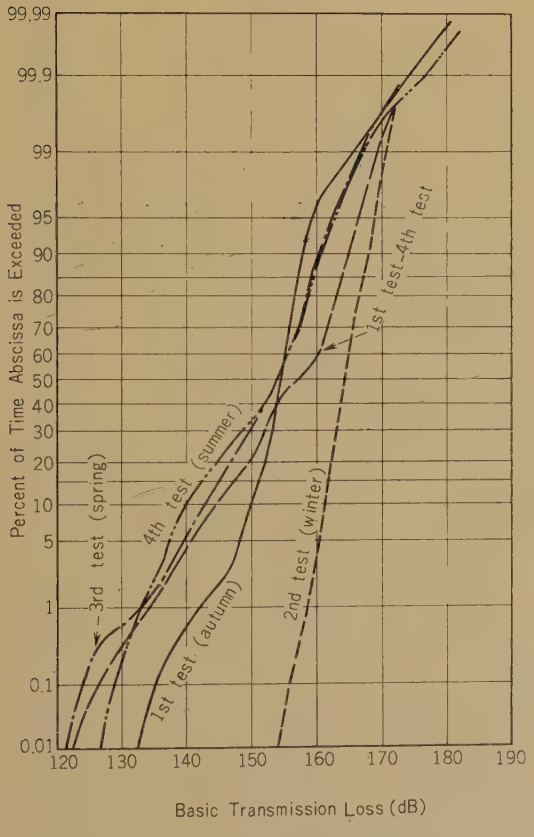


**Fig. 15**—Distributions of instantaneous signal levels on Wakayama~Muroto-misaki path at 250 Mc/s.

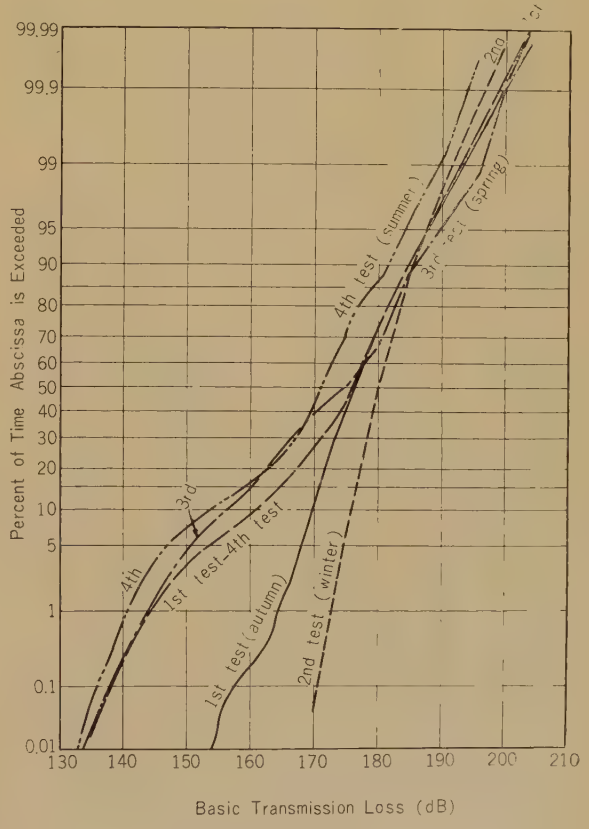


**Fig. 16**—Distributions of instantaneous signal levels on Wakayama~Muroto-misaki path at 970 Mc/s.

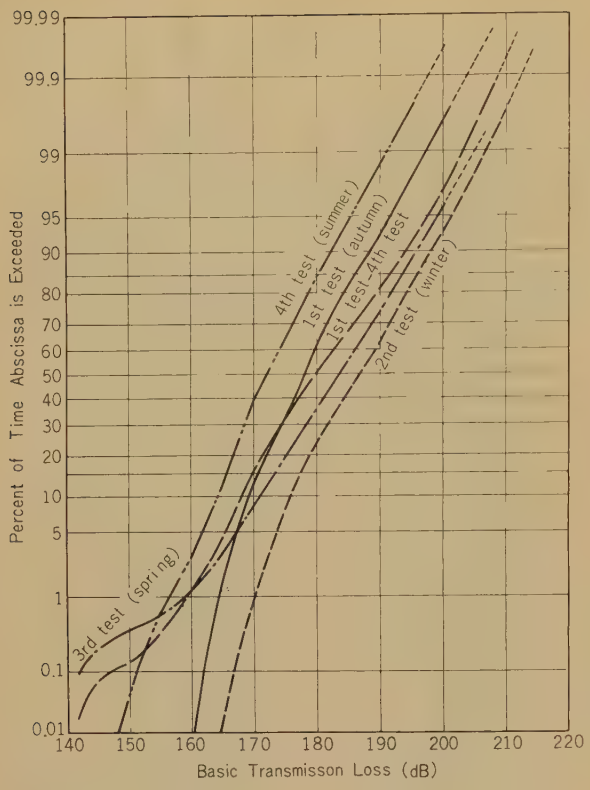


**Fig. 17**—Distributions of the instantaneous signal levels on Miyazaki~Muroto-misaki path at 50 Mc/s.

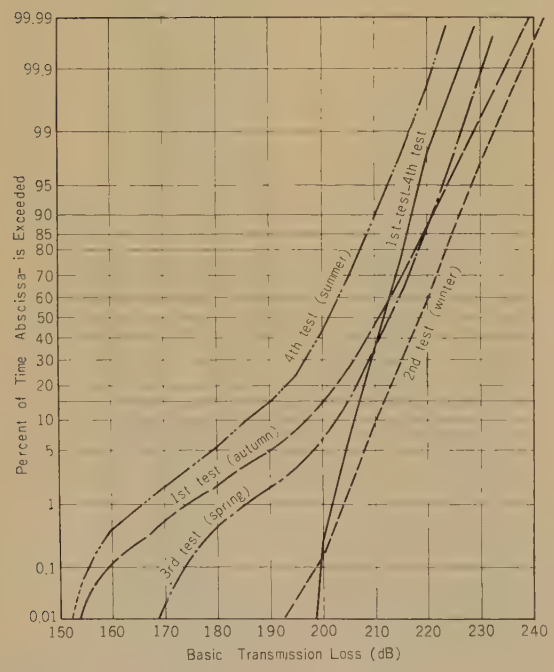


**Fig. 18**—Distributions of the instantaneous signal levels on Miyazaki~Muroto-misaki path at 1,300 Mc/s.

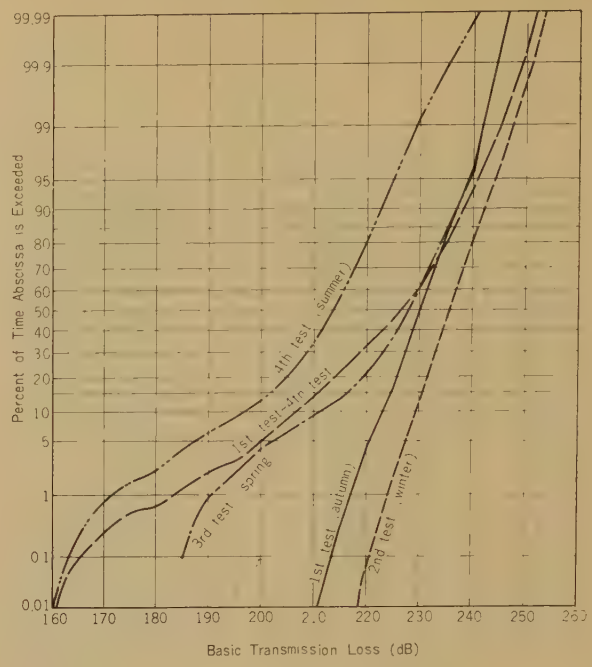


**Fig. 19**—Distributions of the instantaneous signal levels on Miyazaki~Muroto-misaki path at 3,000 Mc/s.

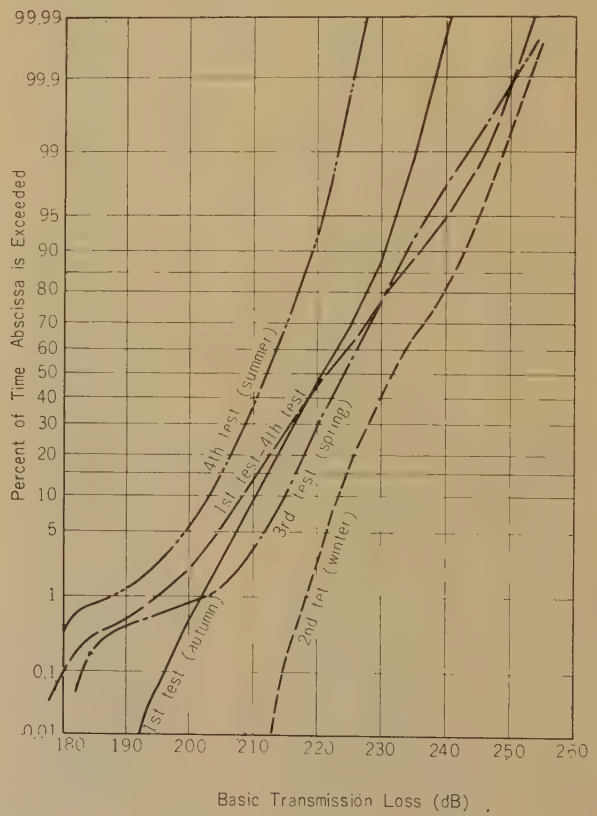


**Fig. 20**—Distributions of the instantaneous signal levels on Miyazaki~Wakayama (Inami) path at 1,300 Mc/s.

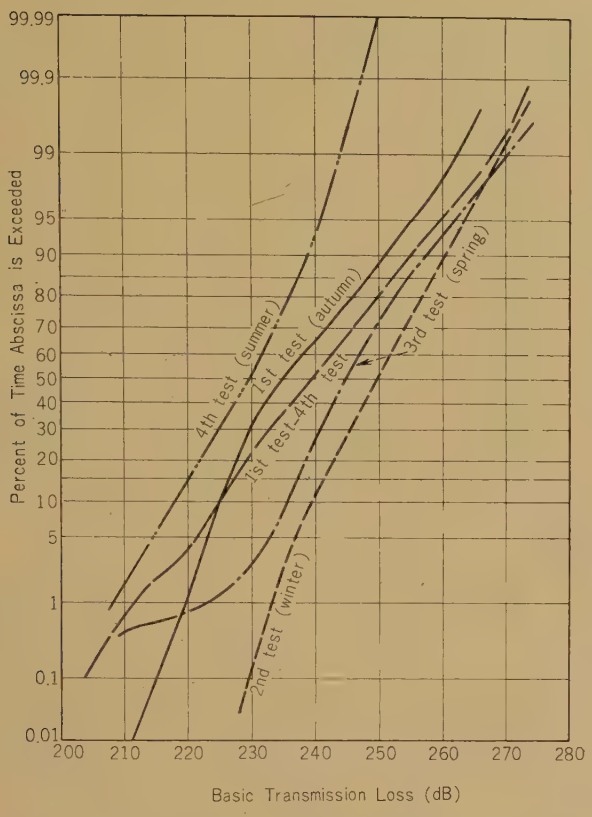


**Fig. 21**—Distributions of the instantaneous signal levels on Miyazaki~Wakayama (Inami) path at 3,000 Mc/s.

### 2.4. Seasonal and Yearly Distributions of Basic Transmission Loss

In Figs. 15–21 are given seasonal and yearly distributions of instantaneous field intensities determined for each frequency and for each propagation path. In calculating the basic transmission loss, the antenna-to-medium coupling loss is not taken into consideration.

The cummulative distribution curve for winter is found in good accord with the normal distribution while the curves for other seasons manifest some deviations. Particularly in summer, the deviation is most marked, giving a large percentage of time of the enhanced field intensity. This tendency is most conspicuous on the path between Miyazaki and Muroto-misaki, followed by that on the near-horizon path between Wakayama and Muroto-misaki, and that on the path between Wakayama and Miyazaki in decreasing order.

The above characteristics are summarized as follows:

(i) The scatter propagation is dominant, under normal conditions, on the 300 km-path between Miyazaki and Muroto-misaki. On warm days, however, there sometimes appears the duct propagation in which the received signal shows the features entirely different from those in scatter propagation.

(ii) On the near-horizon path between Wakayama and Muroto-misaki, the field due to the diffraction by the earth is decreased in winter because of relatively small value of the effective radius of the earth, and relatively rapid fadings are produced in the received signal. During the other seasons, propagation by diffraction is as dominant as the duct propagation.

(iii) On the path between Miyazaki and Wakayama, the scatter propagation is dominant all through the year. Duct propagation takes place in summer, but the signal levels are not so enhanced as on the path between Miyazaki and Muroto-misaki.

Distributions of field intensities, accumulated for the whole period of the tests, possibly include all the types of propagation mentioned above. Therefore, for obtaining the cummulative distributions solely of the scatter propagation, it was necessary to choose out only the data of scatter propagation by a careful examination of records of the low-speed recorder. The distribution curves thus obtained for the Miyazaki - Muroto-misaki and Miyazaki - Wakayama paths at 1,300 Mc/s and 3,000 Mc/s are shown in Figs. 22–25. The signal strength for spring and summer as well as those for a whole year are found normal-distributed, the 50 - 90 % value and the 50 - 1 % value being of about 15 dB. Therefore, the long-term distribution of instantaneous field intensities, as determined of the scatter propagation, may be considered as nearly normal-distributed.

### 2.5. Seasonal Variation of Basic Transmission Loss

In general, the median transmission loss

shows a marked variation with season; it is smallest in summer, and largest in winter. This tendency is observed at all frequencies and over all propagation paths as shown in Fig. 26.

The median value on the near-horizon path between Muroto-misaki and Wakayama is at its maximum in winter, while the values for summer, spring, and autumn are almost equal, the difference being only of about 1 dB from one another at both 259 and 970 Mc/s. The difference between the median value for summer and that for winter is of about 10 dB at 250 Mc/s, and about 8 dB at 970 Mc/s.

The magnitude of seasonal variations on the path between Miyazaki and Muroto-misaki increases with frequency; that is, the difference between the median values for summer and for winter is of about 15 dB at 50 Mc/s, about 17 dB at 1,300 Mc/s and about 22 dB at 3,000 Mc/s.

On the path between Wakayama and Miyazaki, the range of seasonal variation is of about 19 dB at 1,300 and 3,000 Mc/s. The variation, in this case, does not increase with frequency as on the path between Miyazaki and Muroto-misaki.

Comparison is made in Fig. 27 and in Table 3 of the range of seasonal variations obtained in our tests with the data published before in Japan and abroad. As is obvious from this figure and this table, the seasonal

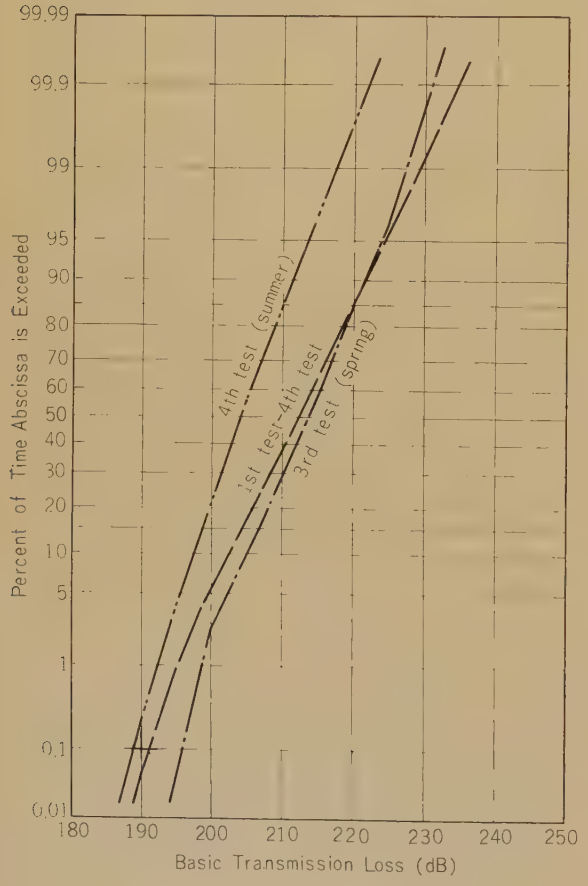


**Fig. 22**—Distributions of the instantaneous signal levels excluding abnormal propagation on Miyazaki~Muroto-misaki path at 1,300 Mc/s.

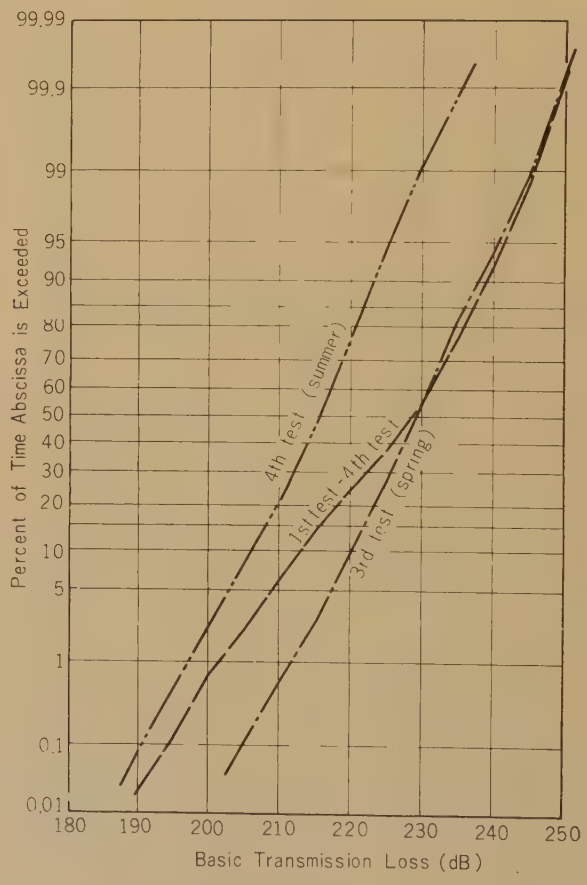


**Fig. 23**—Distributions of the instantaneous signal levels excluding abnormal propagation on Miyazaki~Muroto-misaki path at 3,000 Mc/s.

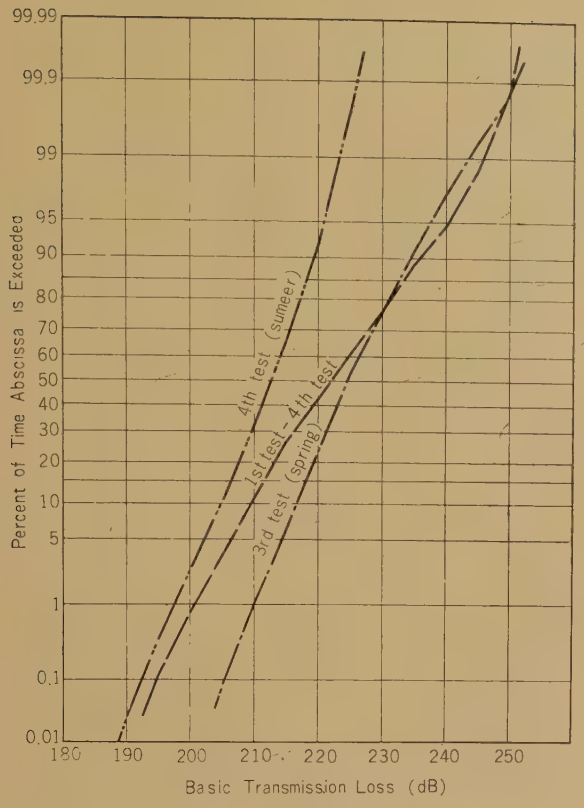


**Fig. 24**—Distributions of the instantaneous signal levels excluding abnormal propagation on Miyazaki~Wakayama (Inami) path at 1,300 Mc/s.

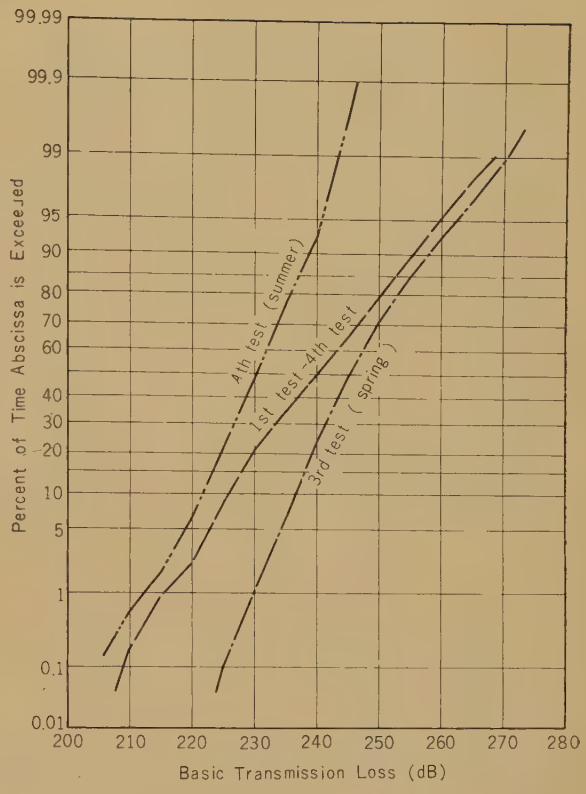


**Fig. 25**—Distributions of the instantaneous signal levels excluding abnormal propagation on Miyazaki~Wakayama (Inami) path at 3,000 Mc/s.

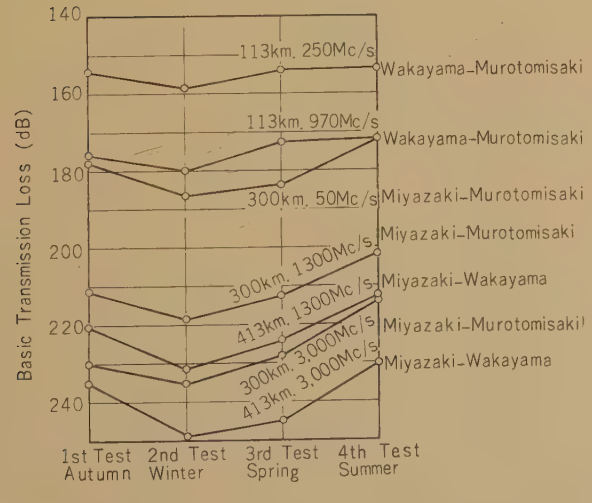


**Fig. 26**—Seasonal variations of median signal levels.

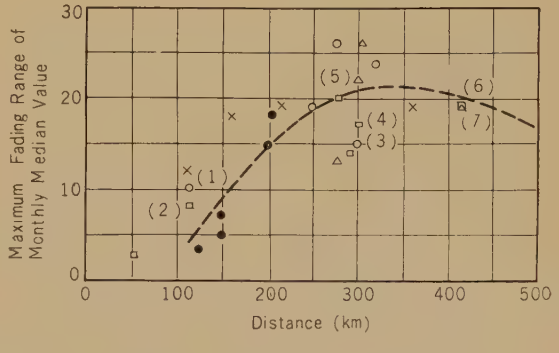


VHF: ● Overland ○ Oversea
UHF: × do □ do
SHF: △ do

(1) 250 Mc/s (4) 1,300 Mc/s (Muroto-misaki)
(2) 970 Mc/s (5) 3,000 Mc/s (Muroto-misaki)
(3) 50 Mc/s (6) 1,300 Mc/s (Wakayama)
(7) 3,000 Mc/s (Wakayama)

**Fig. 27**—Seasonal variation range vs. distance.

**Table 3**

MAXIMUM RANGE OF MONTHLY MEDIAN LOSSES BETWEEN WORST AND BEST MONTHS

| Frequency (Mc/s) | Distance (km) | Path | Range (dB) |
|---|---|---|---|
| 250 | 113 | Oversea | 10.1 |
| 970 | 113 | do | 7.9 |
| 50 | 300 | do | 14.8 |
| 1,300 | 300 | do | 17.2 |
| 3,000 | 300 | do | 21.9 |
| 1,300 | 413 | do | 19.4 |
| 3,000 | 413 | do | 18.9 |
| 100 | 150 | Overland | 7.0 |
| 100 | 200 | do | 15.0 |
| 100 | 100 | do | 5.0 |
| 100 | 240 | Coastline | 19.0 |
| 107 | 205 | Overland | 18.0 |
| 107.75 | 280 | Oversea | 26.0 |
| 153 | 125 | Overland | 3.5 |
| 220 | 320 | Coastline | 24.0 |
| 385.5 | 290 | do | 14.0 |
| 412 | 160 | Overland | 18.0 |
| 418 | 215 | do | 19.0 |
| 505 | 278 | Coastline | 20.0 |
| 535 | 53 | Overland | 3.0 |
| 1,046 | 110 | do | 12.0 |
| 1,046 | 360 | do | 19.0 |
| 3,670 | 302 | Coastline | 26.0 |
| 4,090 | 278 | do | 13.0 |

variation on over-sea paths is generally greater than that on the overland paths, though there is a slight discrepancy probably due to the character or the local conditions of the propagation path. The range of seasonal variation reaches its maximum value of about 20 dB at a distance between 200 and 300 km, and increases with frequency. At longer distances, it becomes constant independent of frequency.

The cause of such seasonal variations is not clear at present, because of the lack of our knowledge on the mechanism of the beyond-horizon propagation. On a qualitative basis, however, we may presume that the seasonal variations arise from variations in gradients of the atmospheric refractive index or from those in its irregular distributions, [6] though we are not throughly aware of the factor that plays the most important role.

To check this, the daily variation of median transmission loss is compared in Fig. 28 with that of the surface refractive index $N_s = (n_s - 1) \times 10^6$, observed at the Tosa-simizu Meteorological Observatory. A good correlation in seasonal trend appears to exist between them. In drawing the curves, the $N_s$ values at the mid-path point have been used, because they seem to represent the average $N_s$ over the propagation path, if the time average over a comparatively long period is taken. The correlations between the transmission loss and the surface refractive index are also shown in Fig. 29, in the form of scatter diagrams, for each frequency and for each distance.

The correlation is found to increase with increasing frequency and with increasing distance; this suggests that the mean refractive index at the surface will be a good tool for estimating the seasonal variation of the UHF field strength at a long distance.

### 2.6. Day-to-Day Variation

In general, the median field intensity manifests a marked day-to-day variation, with a cycle of several days, simultaneously on all paths and at all frequencies. The day-to-day variation of the 1, 10, 50, 90, and 99 % values of the basic transmission loss is shown in Figs. 30–36. The correlation coefficients of the 50 % values for pairs of frequencies are tabulated in Table 4.

There exist relatively good correlations between each pair of frequencies at given dis-

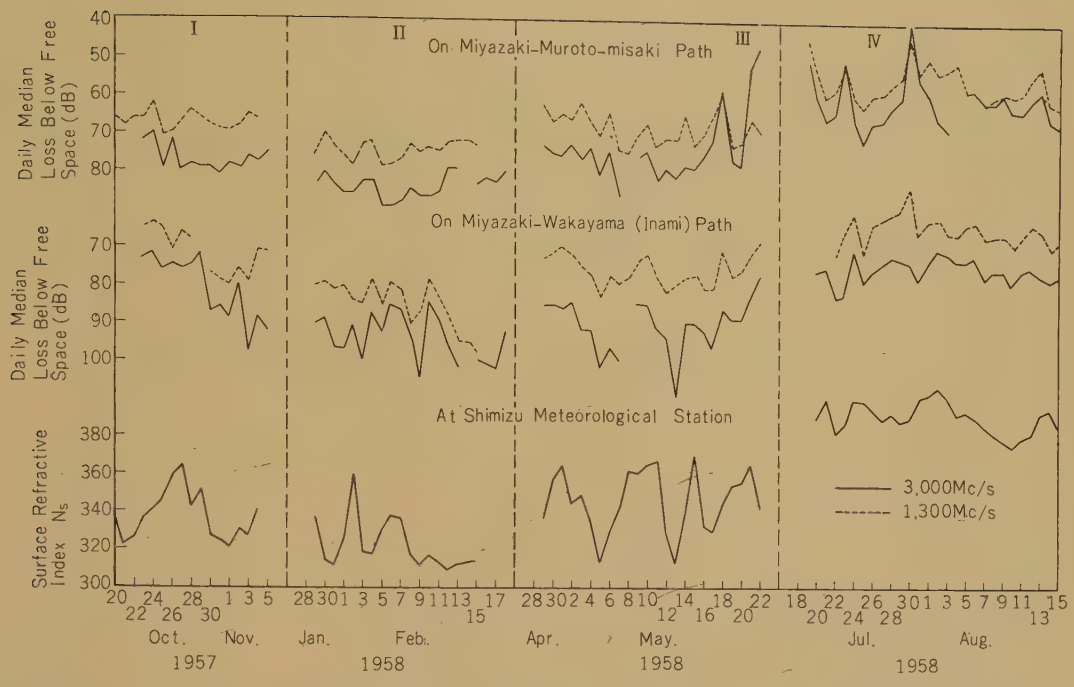


**Fig. 28**—Comparison of daily median transmission loss with surface refractive index, $N_s$.

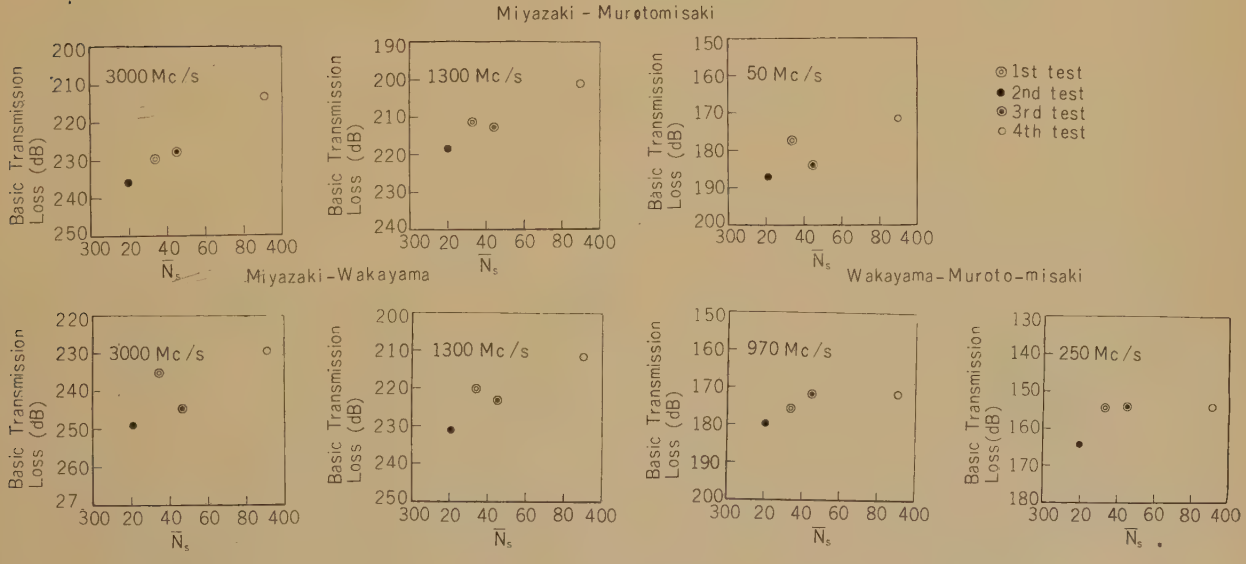


**Fig. 29**—Correlation between median basic transmission loss and surface refractive index, $N_s$.

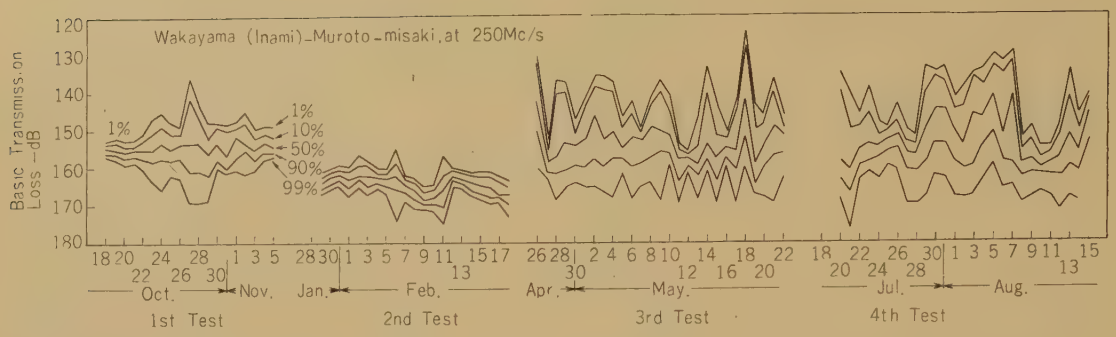


**Fig. 30**—Daily variation of basic transmission loss (1, 10, 50, 90, and 99% values).

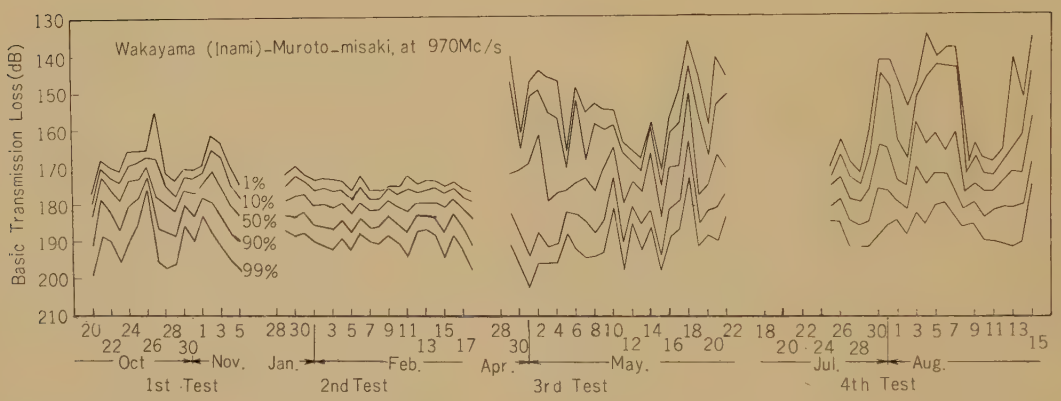


**Fig. 31**—Daily variation of basic transmission loss (1, 10, 50, 90, and 99% values).

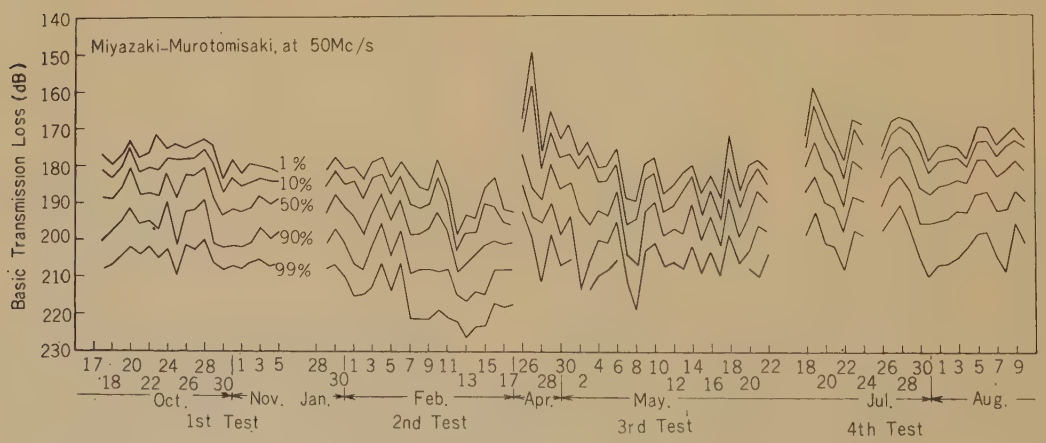


**Fig. 32**—Daily variation of basic transmission loss (1, 10, 50, 90, and 99% values).

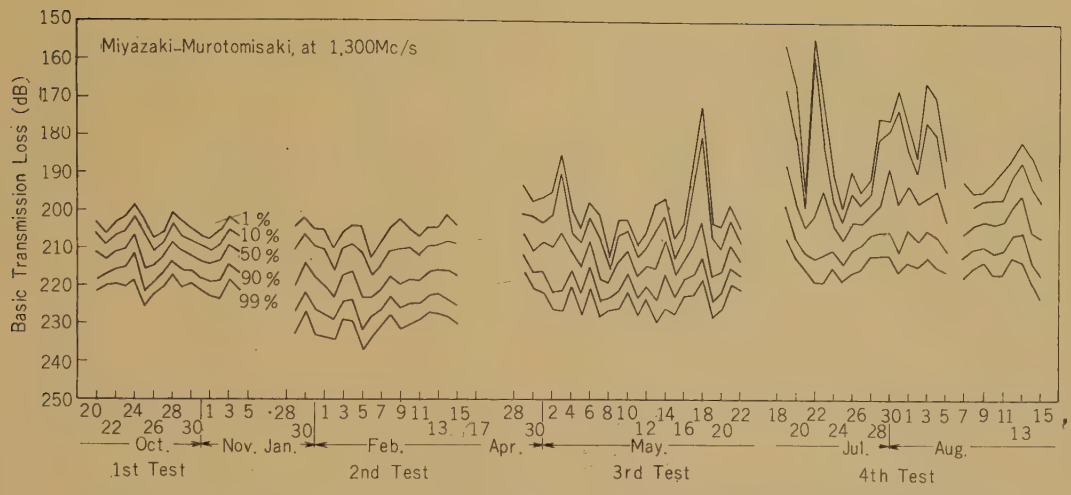


**Fig. 33**—Daily variation of basic transmission loss (1, 10, 50, 90, and 99% values).

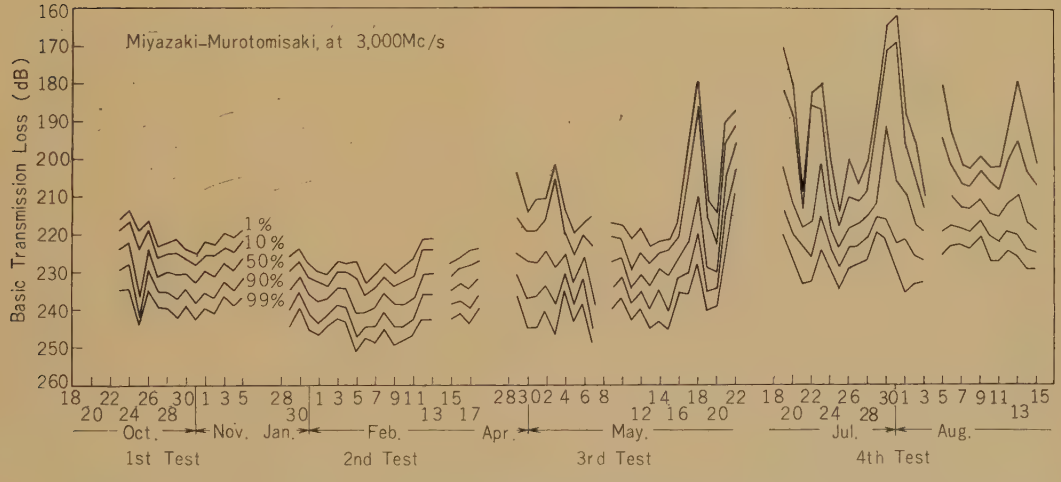


**Fig. 34**—Daily variation of basic transmission loss (1, 10, 50, 90, and 99% values).

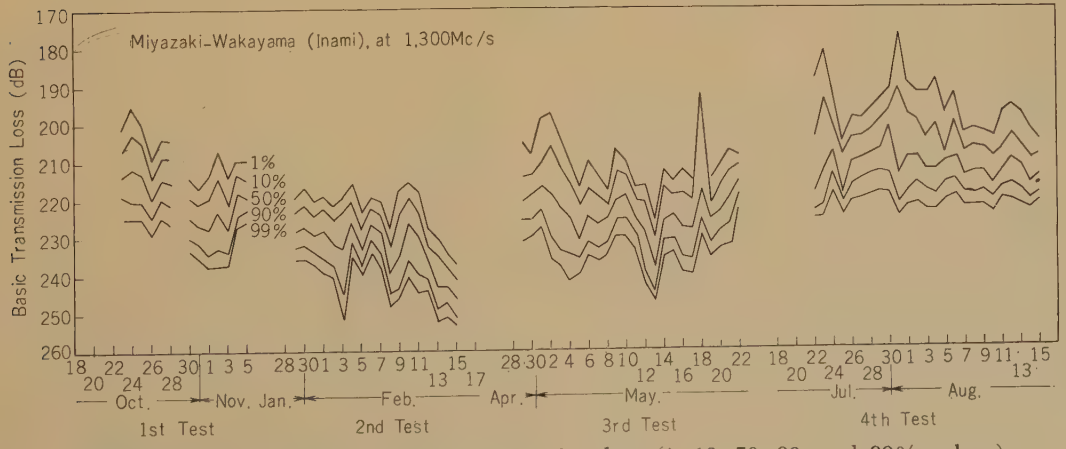


**Fig. 35**—Daily variation of basic transmission loss (1, 10, 50, 90, and 99% values).

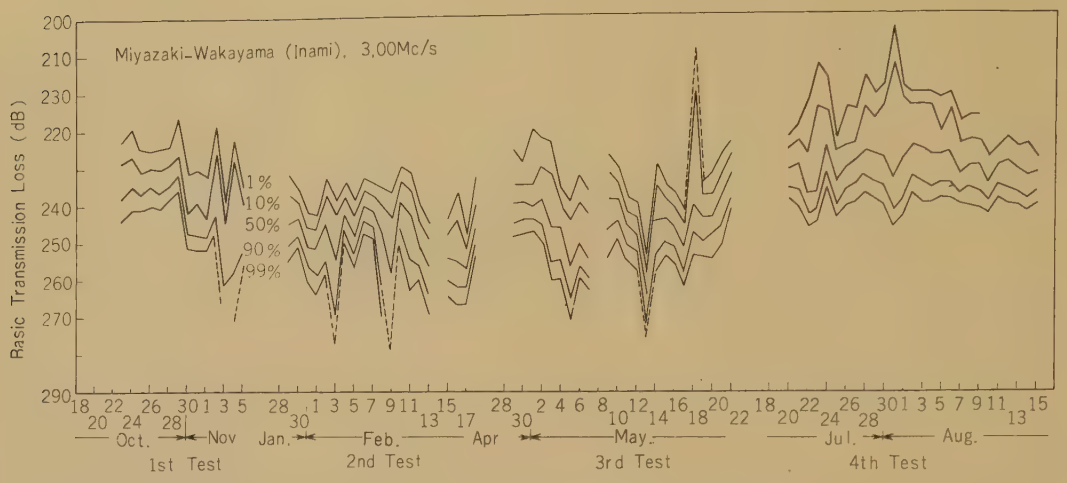


**Fig. 36**—Daily variation of basic transmission loss (1, 10, 50, 90, and 99% values).

**Table 4**

CORRELATION COEFFICIENTS FOR TWO FREQUENCIES AND FOR TWO DISTANCES

| Site | Distance (km) | Frequency (Mc/s) | Correlation Coefficient | Correlation Coefficient* |
|---|---|---|---|---|
| Muroto-misaki | 113 | 970, 250 | 0.88 | — |
| | 300 | 1,300, 50 | 0.62 | 0.63 |
| | 300 | 3.000, 1,300 | 0.85 | 0.87 |
| Wakayama | 413 | 3,000, 1,300 | 0.88 | 0.89 |

| Site | Frequency (Mc/s) | Distance (km) | Correlation Coefficient | Correlation Coefficient* |
|---|---|---|---|---|
| Muroto-misaki | 1,300, 970 | 113, 300 | 0.72 | — |
| Muroto-misaki Wakayama | 1,300 | 300, 413 | 0.78 | 0.74 |
| Muroto-misaki Wakayama | 3,000 | 300, 413 | 0.53 | 0.52 |

* Values after the elimination of abnormal propagation.

tances, except in the case of 50 and 1,300 Mc/s at a distance of 300 km. This seems to arise from a frequency-dependent nature of the irregular distributions in the refractive index of the atmosphere.

The correlation between the day-to-day variations of the transmission loss on the two paths (Miyazaki–Muroto-misaki and Miyazaki–Wakayama) is relatively good at 1,300 Mc/s, but it is not good at 3,000 Mc/s. This may be attributed to the fact that the effect of the receiving antenna height on duct propagation will vary with frequency. Thus, in this case, the correlation becomes worse with increasing frequency, at a sufficiently long distance and at frequencies above the UHF.

Fig. 28 shows the daily variation of the basic transmission loss and that of the average refractive index at the earth's surface during each test period. There is not a good correlation between them as was found in the seasonal variations of the transmission loss and $N_s$. The correlation, however, seems better on the path between Miyazaki and Wakayama than on the path between Miyazaki and Muroto-misaki.

In any case, it will be difficult to predict the day-to-day variations on the basis of the $N_s$ values.

Comparison was made of the hourly median field intensity with the aerological data which were obtained in the 3rd test by means of the drop radiosonde. It is found that an enhancement in the field strength is correlated with the formation of an abrupt change in the refractive index of the atmosphere. In the upper part of Fig. 37 are illustrated the hourly median signal strength measured during the 3rd test on the paths between Miyazaki and Muroto-misaki, and between Miyazaki and Wakayama, at 1,300 and 3,000 Mc/s. The layers with steep gradient of the refractive index for every 500m ($\Delta N$/500m) are shown just below the figure. Comparison of these two graphs shows that the field intensity increases when a layer of steep N-gradient appears in the upper atmosphere, and that this phenomenon often continues for one or two days after an interval of several days. This fact suggests that the day-to-day variation of the field intensity is closely related to the appearance of a layer with steep N-gradient.

These layers of steep N-gradient are attributed to a sudden change in humidity caused by a very dry air mass lying above a wet

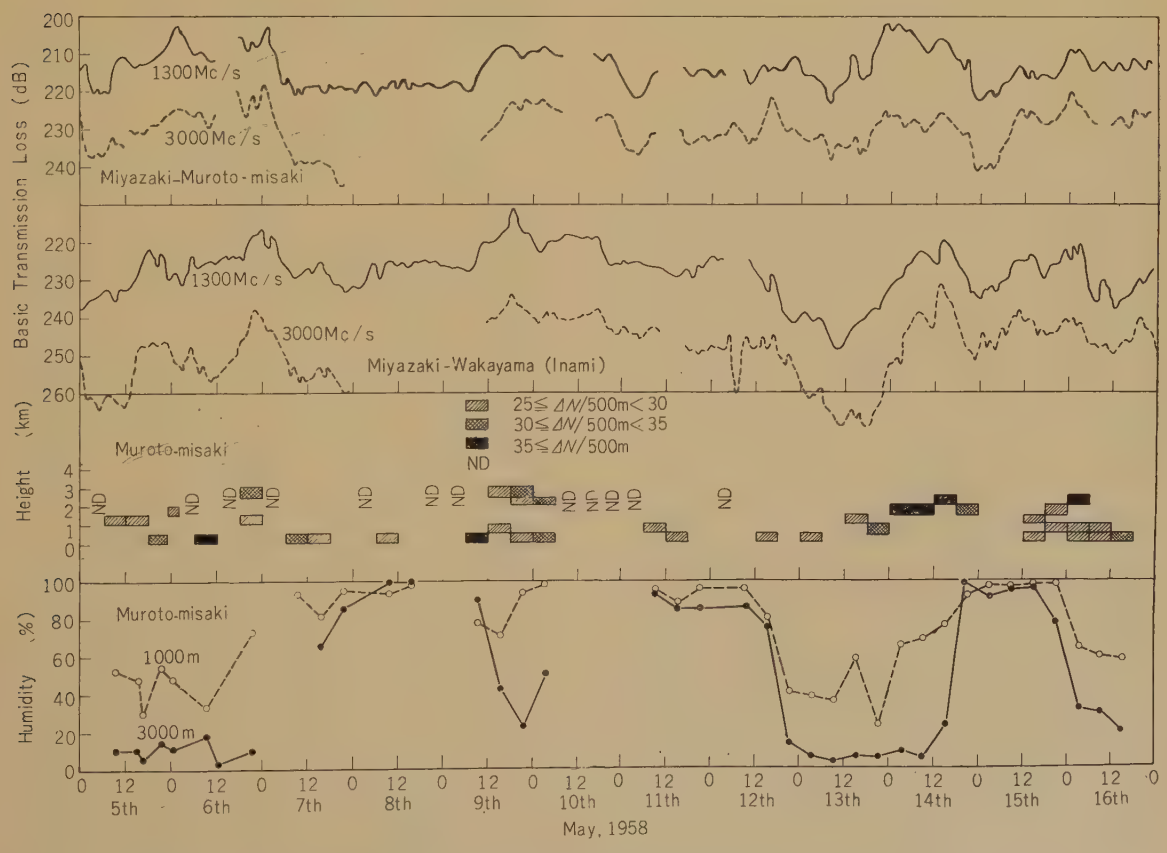


**Fig. 37**—Comparison of daily variation of field intensity with meteorological data.

air mass. At the bottom of Fig. 37 are shown the variations of the relative humidity at the heights of 1,000 and 3,000 m above the sea level. It is obvious that a layer of steep N-gradient is formed when the upper atmosphere (at 3,000m) is very dry in comparison with the lower atmosphere (at 1,000m). This sort of very dry air mass is presumably formed in connection with the subsidence in a high pressure area, and the layer of steep N-gradient is apt to occur in a high pressure area, in particular, in its rear part.

During the season of the 3rd test, high pressure areas often traversed this country from west to east at fairly regular intervals. When the propagation path lies in the high pressure area, the field intensity increases as a layer with an abrupt change of refractive index is formed. After the high pressure area has passed away, the field intensity decreases again, when the layer disappears.

The day-to-day variation of field intensity takes place in this way corresponding to coming and going high pressure areas which are characteristic in this season of the year.

Of course, the layer with steep N-gradient will not be enough to account for the day-to-day variation of the field intensity, because the mechanism of beyond-horizon propagation may involve many other factors, and because the dominant factors may vary with season.

However, it can safely be said that the layer with an abrupt change of refractive index is one of the important factors which control the day-to-day variation of the field strength, since it is observed more or less in every season of the year.

### 2.7. Diurnal Variation

No obvious diurnal variation of the field intensity is found in our data in contrast to the case of overland propagation.[7] This seems to suggest that the distribution of refractive index in the lower atmosphere exhibits less diurnal variation over the sea than over the land. If the field intensity is more influenced by the upper atmosphere than by the lower atmosphere, it would manifest very little diurnal variations. This is so because the meteorological conditions are more stable in the upper atmosphere than in the lower atmosphere.

It is sometimes observed, however, that the field intensity level is several decibels higher at night than in the daytime, and that an abnormal increase of the field intensity is likely to occur at night rather than in the daytime. This phenomenon may be attributed to the fact that the night cooling of the earth's surface, sometimes together with the subsidence effect, strengthens the discontinuity in the atmospheric refractive index.

### 2.8. Comparison of Experimental Data with Conventional Theoretical Formulas and Propagation Curves

Median values for the basic transmission loss obtained in our tests will be compared with theoretical values and with the values predicted by propagation curves. Theoretical values were obtained from Norton's formula [8] which is based on Booker-Gordon's theory and on the modified theory by Weisskopf and Villars. As the propagation curves, we have adopted the ones presented by Bullington,[9] by Gerks[10] and by Norton.[11]

Theoretical formulas and propagation curves can be summarized as follows:

(a) Booker-Gordon-Norton's theoretical formula[12]

The mean value of the basic transmission loss, $L_{bas}$, is given by the following formula;

(i) If the scattering volume lies at a level higher than 700 m above the ground:

$$L_{bas} = -122.52 + 20\log_{10} f + 30\log_{10} d + 40\log_{10}\theta - 10\log_{10}\left[A(s) + A\left(\frac{1}{s}\right)\right] - H_{ot} + H_{or} - F\left[\left(\frac{l_o}{\lambda}\right)\theta\right] - 10\log_{10} B \qquad (L_{bas} \text{ in dB, } d \text{ in km}) \qquad (1)$$

(ii) If the scattering volume lies at a level lower than 700 m:

$$L_{bas} = -55.77 - 20\log_{10} f - 10\log_{10} d + 20\log_{10}\theta - 10\log_{10}\left[\frac{C(o)}{L_o}\right] - F\left[\left(\frac{l_o}{\lambda}\right)\theta\right] - H_{ot} - H_{or}$$

($L_{bas}$ in dB, $d$ in km) (2)

(b) Weisskopf-Villars-Norton's theoretical formula[13]

$$L_{bas} = -20.79 + 30\log_{10} f + 49.1\log_{10}\theta + 29.1\log_{10} d - F(s) - H_{ot} - H_{or} - F\left[\left(\frac{L_o}{\lambda}\right)\theta\right].$$

($L_{bas}$ in dB, $d$ in km) (3)

(c) Bullington's propagation curves

Curves are given for two different frequency bands: 40 to 300 Mc/s and 300 to 4,000 Mc/s.

(d) Gerks' propagation curve

The transmission loss, $L_{sc}$, relative to the free space is given by

$$L_{sc} = 57 + 0.075\,(d - 160), \quad (4)$$

where $L_{sc}$ in dB, $d$: distance (km) $>160$ km.

(e) Norton's propagation curve

The loss is expressed in terms of the distance between the transmitter's and the receiver's horizons.

Values of the basic transmission loss calculated from the twe theoretical formulas and from the three propagation curves are shown in Table 5, together with the observed values, for the evaluation of which account has not been taken of the antenna aperture-to-medium-coupling loss. An appreciable discrepancy is seen between the measured and the predicted values. Even the median values measured in winter, which are expected to fit the scatter theory best, deviate from the theoretical values by about 10 dB.

Booker-Gordon-Norton's formula is in a good agreement with the observed data if the scattering volume is not so elevated, while Weisskopf-Villars-Norton's formula is in a better agreement for a sufficiently high volume if account is taken of the antenna aperture-to-mediam coupling loss. The Bullington's propagation curve, amongst the three, appears to be best fitted to the measured values. In particular, if the antenna aperture-to-mediam coupling loss of several decibels is taken into consideration, the discrepancy reduces to within a few decibels. In general, the agreement appears better with the propagation curves than with the theoretical formulas.

The above results suggest that, between the observed and the predicted values, a discrepancy within a range of 10 dB is inevitable. It is presumably due to the abnormal propagation which sometimes occurs in spring and in summer, and to the meteorological and the terrestrial localities along the path.

### 2.9. Frequency Characteristics of Median Basic Transmission Loss

Earlier scatter theory predicted the received field intensity relative to the free space value be independent of frequency. Although the recent studies have revealed the loss to increase with increasing frequency, the quantitative relation is not yet clarified.

The frequency dependence found in our tests is as the following: Fig. 38 gives the frequency characteristics obtained for the transmission loss relative to the free space and Table 6 their numerical values with the antenna aperture-to-medium coupling loss disregarded.

a) On the near-horizon path between Wakayama and Muroto-misaki, the basic transmission loss is found to increase with frequency as more than the third power of the latter. This might be attributed to a non-standard structure of the lower atmosphere which presumably modifies the frequency dependence.

In winter when the atmosphere is considered almost homogeneous, the observed frequency dependence is of the form of $f^{2.7}$ where $f$ represents the frequency, while the pre-

**Table**

COMPARISON OF COMPUTED AND OBSERVED

| Frequency (Mc/s) | Distance (km) | Free Space Loss (dB) | Computed Values (Basic | | | |
|---|---|---|---|---|---|---|
| | | | *W-V-N*[1] | *B-G-N*[2] | Norton's Curve | Bullington's Curve |
| 250 | 113 | 121.6 | 143.3 | 162.5 | 165.1 | 161.6 |
| 970 | 113 | 133.2 | 156.2 | 173.6 | 178.7 | 179.2 |
| 50 | 300 | 115.7 | 176.9 | 204.0 | 177.0 | 181.7 |
| 1,300 | 300 | 144.3 | 210.5 | 221.0 | 205.8 | 214.3 |
| 3,000 | 300 | 151.5 | 221.3 | 222.7 | 213.0 | 221.5 |
| 1.300 | 413 | 147.1 | 225.2 | 233.9 | 220.5 | 226.1 |
| 3.000 | 413 | 154.3 | 236.0 | 236.6 | 227.8 | 233.5 |

1) *W-V-N*: Theory by Weisskopf, Villars and Norton 2) *B-G-N*: Theory by Booker, Gordon

**Table**

FREQUENCY CHARACTERISTICS OF

| Distance (km) | Frequency (Mc/s) | Computed Values ($x$)[1] | | | |
|---|---|---|---|---|---|
| | | *W-V-N* | *B-G-N* | Norton's Curve | Ballington's Curve |
| 113 | 250<br>970 | 1.9 | 1.8 | 2.3 | 3.0 |
| 300 | 50<br>1,300 | 2.3 | 1.2 | 2.0 | 2.3 |
| 300 | 1,300<br>3.000 | 3.0 | 0.8 | 2.0 | 2.0 |
| 413 | 1.300<br>3.000 | 3.0 | 0.8 | 2.0 | 2.0 |

1) $L_{bf_1}/L_{bf_2} \propto f^x$

dicted values of the exponent are all of about 2.0 except for Bullington's propagation curves and for Watson-Van der Pol-Bremmer's diffraction theory. The exponent is of 3.0 if one uses Bullington's curves which are prepared for two frequency bands of 40 to 300 Mc/s and 300 to 4,000 Mc/s.

On the other hand, the diffraction theory due to Watson, Van der Pol and Bremmer predicts the value of the exponent to be of about 3.7. But, this value reduces to 3.0 if account is taken of unequal heights of the

5

TRANSMISSION LOSSES

| Transmission Loss) (dB) | | | Observed Values[3] (Basic Trans. Loss) (dB) | | | | |
|---|---|---|---|---|---|---|---|
| Gerks Curve | Bullington's Nomograph | Mean | 1st Test Autumn | 2nd Test Winter | 3rd Test Spring | 4th Test Summer | Mean |
| 174.1 | 153.2 | 160.0 | 154.4 | 163.8 | 154.0 | 153.7 | 156.0 |
| 185.7 | 175.4 | 174.8 | 176.0 | 179.9 | 172.4 | 172.0 | 175.5 |
| 183.2 | | 184.6 | 177.8 | 186.8 | 183.7 | 172.0 | 179.6 |
| 211.8 | | 212.7 | 211.6 | 218.7 | 212.8 | 211.5 | 211.0 |
| 219.6 | | 219.5 | 230.2 | 235.6 | 227.9 | 213.7 | 227.0 |
| 223.1 | | 225.8 | 220.5 | 231.6 | 224.0 | 212.2 | 221.2 |
| 230.3 | | 232.8 | 234.8 | 248.8 | 244.7 | 229.5 | 239.5 |

and Norton 3) With antenna aperture to medium coupling loss disregarded.

6

MEDIAN TRANSMISSIOL LOSSES

| | | Observed Values $(x)$[2] | | | | |
|---|---|---|---|---|---|---|
| Gerks' Curve | Bullington's Nomograph | 1st Test Autumn | 2nd Test Winter | 3rd Test Spring | 4th Test Summer | Mean |
| 2.0 | 3.7 | 3.7 | 2.7 | 3.1 | 3.1 | 3.3 |
| 2.0 | | 2.4 | 2.2 | 2.0 | 2.0 | 2.2 |
| 2.0 | | 5.2 | 4.7 | 4.2 | 3.4 | 4.5 |
| 2.0 | | 4.0 | 4.8 | 5.8 | 4.9 | 5.1 |

2) With antenna aperture-to-medium coupling loss disregarded.

transmitting antennas, 50 m for 250 Mc/s and 35 m for 970 Mc/s.

b) Experimental results indicate that, on the 300 km path between Miyazaki and Muroto-misaki, transmission losses for 50 and 1,300 Mc/s increase with frequency both as $f^2$.

The observed value of the exponent is of about 4.5 for frequencies of 1,300 and 3,000 Mc/s but this value reduces to the one a little larger than 3.0 if account is again taken of the antenna-aperture-to-medium coupling

**Table**

DISTANCE CHARACTERISTICS

| Frequency (Mc/s) | Distance (km) | Computed Values $(x)^{1)}$ | | | |
|---|---|---|---|---|---|
| | | *W V-N* | *B-G-N* | Norton's Curve | Bullington's Curve |
| 1,300 | 300<br>400 | 10.6 | 10.1 | 10.6 | 8.0 |
| 3,000 | 300<br>413 | 10.6 | 10.1 | 10.6 | 8.0 |

1) $L_{bd_1}/L_{bd_2} \propto d^x$.

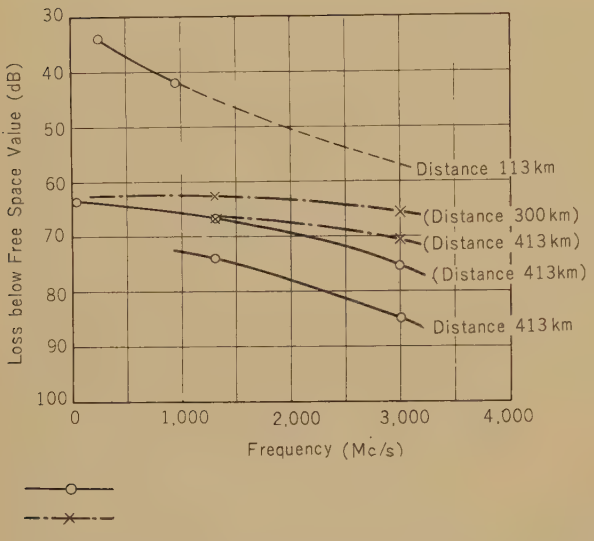


**Fig. 38**—Frequency characteristics of the transmission loss.

loss.

Weisskopf-Villars-Norton's formula predicts the value of about 3 while Booker-Gordon-Norton's formula gives the value of about 1.

If use is made of the propagation curves, an identical value of 2 is obtained.

c) The data obtained at frequencies of 1,300 and 3,000 Mc/s on the 413 km path between Miyazaki and Wakayama indicate that the basic transmission loss increases as the 4.0 to 5.8 power of frequency. If the antenna aperture-to-medium coupling loss is taken into consideration, however, the value reduces to about 3 to coincide approximately with Weisskopf-Villars-Norton's prediction. This value is larger by 1 than that estimated from the propagation curve, and larger by 2 than Booker-Gordon-Norton's prediction.

From these results, it may be concluded that in the VHF band the basic transmission loss increases with frequency approximately as $f^2$, while in the UHF band the exponent is of about 2.5 and, in the SHF band, of about 3.5.

### 2.10. Distance Characteristics of Basic Transmission Loss

The fact that the antenna elevation at Muroto-misaki is very much larger than that at Wakayama may bring complexity in the distance dependence of the basic transmission loss. This is so, in particular, in the case of the duct propagation. In this section, however, this effect will be ignored for simplicity.

Fig. 39 gives the observed relation between the distance and the median transmission loss relative to the free space. Values of the transmission loss for each season, for a year and for frequencies in three bands, VHF (50 and 250 Mc/s), UHF (970 and 1,300 Mc/s) and SHF (3,000 Mc/s), are given.

Values of the loss observed at frequencies of 1,300 and 3,000 Mc/s are tabulated in Table 7 together, for comparison, with those obtained from the theoretical formulas and from the propagation curves.

7

TO MEDIAN TRANSMISSION LOSSES

| Gerks' Curve | Observed Values $(x)^{2)}$ 1st Test Autumn | 2nd Test Winter | 3rd Test Spring | 4th Test Summer | Mean |
|---|---|---|---|---|---|
| 8.0 | 6.5 | 9.4 | 8.1 | 7.8 | 7.4 |
| 8.0 | 3.4 | 9.6 | 12.2 | 11.7 | 9.0 |

2) With antenna aperture-to-medium coupling loss disregared.

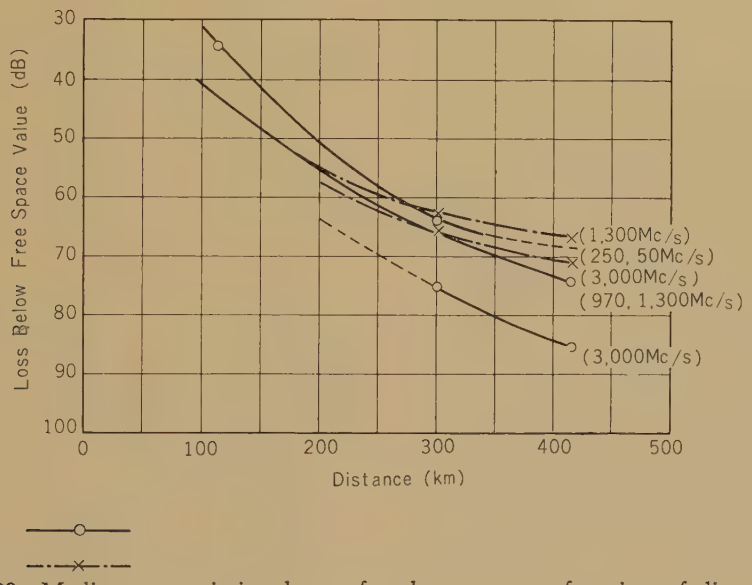


**Fig. 39**—Median transmission losses for the year as a function of distance.

a) In Booker-Gordon-Norton's formula based on the scatter theory, the function that expresses the distance characteristics is given by

$$30 \log_{10} d + 40 \log_{10} \theta - F\left[\left(\frac{l_o}{\lambda}\right)\theta\right]. \quad (5)$$

At higher frequencies, this gives an increase of loss approximately equal to the 7th power of distance. If, in addition, account is taken of the function for unequal antenna heights

$$-10 \log_{10}\left[A(s) - A\left(\frac{1}{s}\right)\right] - H_{ot} - H_{or}, \quad (6)$$

the effective dependence on distance rises to the 10th power.

If Weisskopf-Villars-Norton's formula (3) is adopted, the distance function takes the form

$$49.1 \log_{10} \theta + 29.1 \log_{10} d - F\left[\left(\frac{l_o}{\lambda}\right)\theta\right], \quad (7)$$

which gives the dependence in the 8th power of distance; if the effect of antenna height is considered, it takes the value of 10.

b) Norton's propagation curve takes as abscissa the distance $d - d_t - d_r$ where $d$ is the distance between the transmitter and the

receiver, and $d_t$ and $d_r$ are distances of the transmitter's and the receiver's horizons, respectively. Thus, Norton's propagation curve is prepared with consideration to the effect of antenna elevation, while, it should be noted, other authors' curves are not.

For instance, in the distance range of 300 to 400 km, the loss is expected to increase as the 10.5 power of distance according to Norton's curves, but the loss predicted by Bullington's and Gerks' propagation curves increases only as the 8th power of distance.

On the other hand, the test results show that it is proportional to the 6.5 to 9.4 power of distance at 1,300 Mc/s and to the 3.4 to 12.2 power at 3,000 Mc/s, indicating the value of exponent to widely vary with season. Account taken of the antenna aperture to-medium coupling loss, the value decreases by 2 at 1,300 Mc/s, and by 3 at 3,000 Mc/s.

If the yearly medians are taken, the loss is found to increase as the 5.1 power of distance at 1,300 Mc/s and as the 5.7 power at 3,000 Mc/s both with the antenna apeture-to-medium coupling loss included. Even of the data obtained in winter, the exponents give the value of 7.0 at 1,300 Mc/s and of 6.2 at 3,000 Mc/s, again with the coupling loss taken into consideration.

It is certain, therefore, that, in both cases, observed values of the exponent are smaller than what the theoretical formulas predict to be of 8 to 10.

This discrepancy may partly be accounted for by the fact that most of the propagation curves and the semi-empirical formulas mentioned before are based on data obtained of the overland propagation.

Recently Chisholm[14] has reported that the loss over the sea is more than several decibels smaller than the loss overland and that the distance dependence is less pronounced in the overwater propagation. These features appear in trends to be in a good agreement with what we obtained in these tests.

### Conclusion

This paper describes the characteristics of the median field intensity in beyond-horizon propagation over the sea, as the result of the tests carried out for about one year from August, 1957. The pertinent points are summarized as follows:

(1) The seasonal variation of the median field intensity has following characteristics. The signal levels were highest in summer and lowest in winter at all frequencies and on all test paths. An abnormal increase of the field intensity often took place in spring and in summer, when very rapid fadings disappeared and the signal level became comparatively stationary. This seems to be caused by the occasional duct propagation.

(2) The cumulative distribution of the instantaneous field intensity is found close to the normal distribution except during the abnormal enhancements in signal level. Once an abnormal increase occurs, however, it deviates from the normal distribution in the lower part of time percentage below 1 per cent.

(3) The seasonal variations are more pronounced on over-sea paths than on overland paths and attain the maximum at a distance of 200 to 300 km, then decreasing with distance.

(4) The seasonal variation of the field intensity appears to be closely related to that of the atmospheric refractive lndex at the surface of the earth.

(5) The increase of the field intensity observed in the day-to-day variation seems to be connected with formation of a layer of steep N gradient in the upper atmosphere.

(6) The diurnal variation as frequently observed on overland paths was not found on over-sea paths.

(7) The basic transmission loss is likely to increase approximately in proportion to the square of frequency in the VHF band, in proportion to the 2.5 power of frequency in the UHF band, and in proportion to the 3.5 power in the SHF band.

(8) The basic transmission loss is likely to increase at the rate of the 5 to 7th power of distance, the exponent varying with the season.

(9) The basic transmission loss is smaller

in the over-sea propagation by several decibels than it is in the overland propagation.

It can be said that beyond-horizon propagation manifests various modes of propagation, such as duct propagation, scatter propagation, and other modes of propagation. The dominant mode of propagation is largely affected by the season, the distance and the meteorological conditions.

Under some conditions a certain mode of propagation chiefly contributes to beyond-horizon propagation, while for other conditions two or more different modes of propagation may contribute. Further investigations, therefore, will be necessary to clarify the relation between the mode of propagation and the meteorological conditions, and, moreover, the mechanism of each mode of propagation. Also, for a better understanding of the distance and the frequency dependence in the beyond-horizon propagation, more experimental data are needed to determine the correction terms for theoretical and experimental formulas.

The authors wish to thank the collaborators in the Radio Propagation Research Section of the ECL. They are also gratefully indebted to the members of the Sikoku and the Kyusyu Communications Bureaus of the N.T.T., and to those of the Meteorological Agencies.

### References

(1) For example, K. Bullington, W. J. Inkster and A. L. Durkee, "Results of Propagation Test at 505 Mc and 4090 Mc on Beyond-Horizon Paths," Proc. *I.R.E.*, **43**, 10, p. 1306–1316, 1955.

J. H. Chisholm, P. A. Portmann, J. T. de Bettencourt and J. F. Roche, "Investigation of Angular Scattering and Multipath Properties of Tropospheric Propagation of Short Radio Waves Beyond the Horizon," *Proc. I.R.E.*, **43**, 10, p. 1317–1335, 1955.

(2) K. A. Norton, L. E. Vogler, W. V. Mansfield and P. J. Short, "The Probability Distribution of the Ampiltude of a Constant Vector Plus a Rayleigh-Distributed Vector", *Proc. I.R.E.*, **43**, 10, p. 1354–1361, 1955.

(3) K. A. Norton, "Transmission Loss in Radio Propagation," *Proc. I.R.E.*, **41**, 1, p. 146–152, 1953.

(4) H. G. Booker and deBettencourt, "Radio Transmission by Tropospheric Scattering," *Proc. I.R.E.*, **43**, 3, p. 281–290, 1955.

(5) K. A. Norton, P. L. Rice and L. E. Vogler, "The Use of Angular Distance in Estimating Transmission Loss and Fading Range for Propagation through a Turbulent Atmosphere over Irregular Terrain," *Proc. I.R.E.*, **43**, 10, p. 1511, Fig. 28, 1955.

(6) B. R. Bean and F. M. Meaney, "Some Applications of the Monthly Median Refractivity Gradient in Tropospheric Propagation," *Proc. I.R.E.*, **43**, 10, p. 1419–1431, 1955.

(7) J. H. Chisholm, same as (1), p. 1333, Fig. 25, 1955.

(8) K. A. Norton, same as (7), p. 1488–1526, 1955.

(9) K. Bullington, "Radio Transmission beyond the Horizon in the 40-to-4000 Mc Band," *Proc. I.R.E.*, UHF Issue, **41**, 1, p. 132–135, Fig. 4, Fig. 5, 1953.

(10) I. H. Gerks, "Factors Affecting Spacing of Radio Terminals in a UHF Link," *Proc. I.R.E.*, **43**, 10, p. 1290–1296, Fig. 2 Eq. (1), 1955.

(11) K. A. Norton and others: same as (7), p. 1494, Fig. 7, 1955.

(12) K. A. Norton and others: same as (7), Eqs. (57) and (64), 1955.

(13) K. A. Norton and others: same as (7), Eqs. (63) and (34), 1955.

(14) J. H. Chisholm, "Experimental Investigation of the Angular Scattering and Communications Capacity of Tropospheric Propagation," MIT Report.

* * * *

U.D.C. 621.372.8

# The Cylindrical $TE_{11}$ mode Cavity Including a Semiconductor Sample with Tensorial Electrical Conductivity*

*Naozo WATANABE*†

*The author has derived the impedance matrix and the characteristic matrix (S-matrix) of a cylindrical cavity including a semiconductor sample with tensorial conductivity in which only doubly degenerate $TE_{11n}$ modes are excited. In this paper, the formulae are expressed in terms of $Q_{external}$, $Q_{wall}$, $Q_{sample}$ and the angle $\theta$ between the input* I *and the input* II *wave guides; and special cases are treated in terms of the S-matrix. In Case* I, *$\theta = \pi/2$, the S-matrix is antisymmetric and its off-diagonal components are approximately proportional to the off-diagonal components of the conductivity tensor. This type of cavity is appropriate for the measurement of Hall mobility and other off-diagonal components of the electrical conductivity at microwave frequencies. In Case* II, *$0<\theta<\pi/2$, the cavity may be used as an isolator, if one of the off-diagonal components of the S-matrix equals 0. Proper conditions for an isolator were investigated. Under proper conditions, the maximum transmission coefficient at angle $\theta$ is given by $\cos^2\theta$.*

## Introduction

J. C. Slater developed microwave circuit theory in his work during the war. His work treated the resonant cavity in terms of impedance matrix concepts.(1) The field in the cavity was expanded in terms of orthonormal modes, and the relations between their amplitudes were derived by means of Maxwell's equations. These relations, together with properly defined currents and voltages, gave the impedance matrix.

S. Tomonaga, starting at the same point; that is, from orthonormal modes and Maxwell's equations, introduced the characteristic matrix (*S*-matrix) concept.(2) This matrix related the amplitudes of the incoming waves in all the modes of all the wave guides with the amplitudes of the outgoing waves in all the modes of all the wave guides.

Making use of the methods and concepts of these authors, this paper treats the circular $TE_{11n}$ mode (doubly degenerate) cavity including a semiconductor sample. When a static magnetic field is applied in the direction of the symmetry axis, the electrical conductivity of the semiconductor ceases to be scalar and becomes tensorial. The tensorial conductivity connects otherwise mutually independent $TE_{11n}$ modes of the cavity.

In this paper calculation is done by Slater's formulation, and the impedance matrix of the cavity is derived by using tensorial conductivity in calculating the current in the sample. Then by rearrangement of the matrix, the *S*-matrix is obtained.

## 1. Tensorial Conductivity and Tensorial Surface Impedance on the Free Electron Model

### 1.1. Conductivity

In this section the tensorial conductivity and the tensorial surface impedance are treated on the free electron model.

The basic equations which describe the

* MS received by the Electrical Communication Laboratory, N.T.T., Feb. 23, 1960.

† Semiconductor Research Section.

motions of electrons in semiconductors are as follows:

$$m\frac{d\boldsymbol{v}}{dt}=-\frac{m}{\tau}\boldsymbol{v}+e(\boldsymbol{E}+\boldsymbol{v}\times\boldsymbol{B}) \qquad (1.1)$$

where

$m$: effective mass of an electron
$e$: electric charge of an electron
$\boldsymbol{v}$: velocity of an electron
$\boldsymbol{E}$: electric field strength
$\boldsymbol{B}$: magnetic induction
$\tau$: collision time of an electron.

When an electron is in an alternating electric field and a static magnetic field given by

$$\boldsymbol{E}=\begin{pmatrix}E_x\\E_y\\0\end{pmatrix}e^{j\omega t} \quad \text{and} \quad \boldsymbol{B}=\begin{pmatrix}0\\0\\B\end{pmatrix},$$

the stationary solution of (1.1) in the form

$$\boldsymbol{v}=\begin{pmatrix}v_x\\v_y\\0\end{pmatrix}e^{j\omega t} \quad \text{is given by}$$

$$\begin{pmatrix}v_x\\v_y\end{pmatrix}=\frac{\dfrac{e}{m}}{\left(j\omega+\dfrac{1}{\tau}\right)^2+\left(\dfrac{eB}{m}\right)^2}\begin{pmatrix}j\omega+\dfrac{1}{\tau}, & \dfrac{eB}{m}\\ -\dfrac{eB}{m}, & j\omega+\dfrac{1}{\tau}\end{pmatrix}\begin{pmatrix}E_x\\E_y\end{pmatrix}. \qquad (1.2)$$

If $N/m^3$ charge carriers are present, the conductivity tensor is expressed in the form

$$\begin{pmatrix}i_x\\i_y\end{pmatrix}=Ne\begin{pmatrix}v_x\\v_y\end{pmatrix}=\begin{pmatrix}\sigma_0 & \sigma_1\\ -\sigma_1 & \sigma_0\end{pmatrix}\begin{pmatrix}E_x\\E_y\end{pmatrix}$$

$$=\frac{\dfrac{Ne^2}{m}}{\left(j\omega+\dfrac{1}{\tau}\right)^2+\left(\dfrac{eB}{m}\right)^2}\begin{pmatrix}j\omega+\dfrac{1}{\tau}, & \dfrac{eB}{m}\\ -\dfrac{eB}{m}, & j\omega+\dfrac{1}{\tau}\end{pmatrix}\begin{pmatrix}E_x\\E_y\end{pmatrix}. \qquad (1.3)$$

For an ordinary semiconductor, $\tau$ is of the order of $10^{-13}$ sec at room temperature, so that $\omega\tau\ll 1$ up to the frequency of $10^{11}$ cycles/sec. The conductivity tensor, therefore, is considered to be the same as that in the D. C. case. In this case,

$$\begin{pmatrix}\sigma_0 & \sigma_1\\ -\sigma_1 & \sigma_0\end{pmatrix}=\frac{Neu_0}{1+(u_0B)^2}\begin{pmatrix}1 & u_0B\\ -u_0B & 1\end{pmatrix} \qquad (1.4)$$

so that

$$-\frac{\sigma_1}{\mathrm{Re}(\sigma_0)}=u_0B,$$

which is the usual d.c. Hall angle. In formula (1.4), $u_0=e\tau/m$ is the d.c. Hall mobility, which has the same sign as that of the charge carriers.

### 1.2. Surface Impedance

By using the above mentioned conductivity tensor, the surface impedance tensor of a conductive semiconductor ($\rho\leq 10^{-5}\ \Omega-m$); for example, n-type InSb at room temperature, with magnetic field perpendicular to the surface, can be derived. The basic equations are Maxwell's equations, in the case of conductor with tensorial conductivity.

$$\begin{aligned}&\text{Curl} \quad \boldsymbol{E}+\frac{\partial\boldsymbol{B}}{\partial t}=0\\ &\text{Curl} \quad \boldsymbol{H}-\frac{\partial\boldsymbol{D}}{\partial t}=\boldsymbol{j}.\end{aligned} \qquad (1.5)$$

The boundary of the conductor is at $z=0$. In the region of $z\geq 0$, the medium is characterized by $\varepsilon$, $\mu$, and $\sigma$ (tensor). In the region of $z<0$, the medium is characterized by $\varepsilon_0$, $\mu_0$ and $\sigma=0$, that is, free space. In the case of normal incidence from free space, the surface impedance tensor of the conductor is calculated as follows:

Writing the plane wave solution in the region of $z\geq 0$ in the form

$$\boldsymbol{E}=\begin{pmatrix}E_x\\E_y\\0\end{pmatrix}e^{-\gamma z+j\omega t}, \quad \boldsymbol{B}=\begin{pmatrix}H_x\\H_y\\0\end{pmatrix}e^{-\gamma z+j\omega t}$$

Eqs. (1.5) can be reduced to

$$\begin{pmatrix} \gamma & E_y \\ -\gamma & E_x \end{pmatrix} = -j\omega\mu \begin{pmatrix} H_x \\ H_y \end{pmatrix}$$

$$\begin{pmatrix} \gamma H_y \\ -\gamma H_x \end{pmatrix} = j\omega\varepsilon \begin{pmatrix} E_x \\ E_y \end{pmatrix} + \begin{pmatrix} \sigma_0 & \sigma_1 \\ -\sigma_1 & \sigma_0 \end{pmatrix} \begin{pmatrix} E_x \\ E_y \end{pmatrix} \quad (1.6)$$

From Eqs. (1.6), the equation for $E$ becomes

$$\begin{pmatrix} -\gamma^2 E_x \\ -\gamma^2 E_y \end{pmatrix} = \omega^2\varepsilon\mu \begin{pmatrix} E_x \\ E_y \end{pmatrix} - j\omega\mu \begin{pmatrix} \sigma_0 & \sigma_1 \\ -\sigma_1 & \sigma_0 \end{pmatrix} \begin{pmatrix} E_x \\ E_y \end{pmatrix} \quad (1.7)$$

From (1.7), $\gamma$ satisfies the equation

$$\gamma^2 = -\omega^2\varepsilon\mu + j\omega\sigma_0 \pm \omega\mu\sigma_1 \quad (1.8)$$

For the conductor, $\omega^2\varepsilon\mu \ll \omega\mu\sigma_0$, so the following equation can be obtained.

$$\gamma_\pm = \sqrt{\omega\mu(j\sigma_0 \pm \sigma_1)}. \quad (1.9)$$

$E_x$ and $E_y$ satisfy the relation

$$\frac{E_x}{E_y} = \pm j. \quad (1.10)$$

This means that $\gamma_\pm$ correspond respectively to right and left circularly polarized waves. On the assumption that $E_x = a$, the solutions are

$$\left.\begin{aligned} \boldsymbol{E}_\pm &= ae^{-\gamma_\pm z + j\omega t} \quad (1, \mp j) \\ \boldsymbol{H}_\pm &= \pm a \frac{\gamma_\pm}{\omega\mu} \cdot e^{-\gamma_\pm z + j\omega t} \quad (1, \mp j) \end{aligned}\right\}, \quad (1.11)$$

Introducing $\boldsymbol{e}_\pm$ and $\boldsymbol{h}_\pm$ by

$$\left.\begin{aligned} \boldsymbol{e}_\pm &= e^{-\gamma_\pm z + j\omega t} \quad (1, \mp j) \\ \boldsymbol{h}_\pm &= \pm \frac{\gamma_\pm}{\omega\mu} \cdot e^{-\gamma_\pm z + j\omega t} \quad (1, \mp j) \end{aligned}\right\}, \quad (1.12)$$

the waves in the conductor are expressed by

$$\left.\begin{aligned} \boldsymbol{E} &= a\boldsymbol{e}_+ + b\boldsymbol{e}_- \\ \boldsymbol{H} &= a\boldsymbol{h}_+ + b\boldsymbol{h}_-. \end{aligned}\right\} \quad (1.13)$$

From Eqs. (1.12) and (1.13), the relations between $(H_x, H_y)$ and $(E_x, E_y)$ on the surface are obtained as follows:

$$\begin{pmatrix} E_x \\ E_y \end{pmatrix} = \begin{pmatrix} Z_1 & Z_0 \\ -Z_0 & Z_1 \end{pmatrix} \begin{pmatrix} H_x \\ H_y \end{pmatrix} \quad (1.14)$$

where

$$\left.\begin{aligned} Z_1 &= \frac{1}{2}\left\{\frac{\omega\mu}{\gamma_+} - \frac{\omega\mu}{\gamma_-}\right\} \\ Z_0 &= \frac{j}{2}\left\{\frac{\omega\mu}{\gamma_+} + \frac{\omega\mu}{\gamma_-}\right\} \end{aligned}\right\}. \quad (1.15)$$

These formulae can be reduced to the following form with the aid of Eqs. (1.3) and (1.9):

$$\left.\begin{aligned} Z_1 &= \frac{1}{2}(1-j)\sqrt{\frac{\omega\mu}{2\sigma_0}}\left\{\sqrt{1+j(\omega\tau+u_0B)}\right. \\ &\qquad \left. -\sqrt{1+j(\omega\tau-u_0B)}\right\} \\ Z_0 &= \frac{1}{2}(1+j)\sqrt{\frac{\omega\mu}{2\sigma_0}}\left\{\sqrt{1+j(\omega\tau+u_0B)}\right. \\ &\qquad \left. +\sqrt{1+j(\omega\tau-u_0B)}\right\}. \end{aligned}\right\} \quad (1.16)$$

Moreover, if $\omega\tau \ll 1$,

$$\left.\begin{aligned} Z_1 &= \frac{1}{2}(1+j)\sqrt{\frac{\omega\mu}{2\sigma_0}}\left\{\sqrt{\sqrt{(u_0B)^2+1}+(u_0B)}\right. \\ &\qquad \left. -\sqrt{\sqrt{(u_0B)^2+1}-(u_0B)}\right\} \\ Z_0 &= \frac{1}{2}(1+j)\sqrt{\frac{\omega\mu}{2\sigma_0}}\left\{\sqrt{\sqrt{(u_0B)^2+1}+(u_0B)}\right. \\ &\qquad \left. +\sqrt{\sqrt{(u_0B)^2+1}-(u_0B)}\right\} \end{aligned}\right\} \quad (1.17)$$

In the weak field case they are reduced further to

$$\left.\begin{aligned} Z_1 &= \frac{1}{2}(1+j)\sqrt{\frac{\omega\mu}{2\sigma_0}}\,u_0B \\ Z_0 &= (1+j)\sqrt{\frac{\omega\mu}{2\sigma_0}} \end{aligned}\right\} \quad (1.18)$$

Where $Z_0$ is the same as the ordinary surface impedance, and $Z_1$ is due to the Hall effect. In the approximation $\omega\tau \ll 1$, $Z_1/Re(Z_0)$ takes the form:

$$\frac{Z_1}{Re(Z_0)} = (1+j) \times \frac{\sqrt{\sqrt{(u_0B)^2+1}+u_0B} - \sqrt{\sqrt{(u_0B)^2+1}-u_0B}}{\sqrt{\sqrt{(u_0B)^2+1}+u_0B} + \sqrt{\sqrt{(u_0B)^2+1}-u_0B}} \tag{1.19}$$

which takes the form $\{(1+j)/2\}u_0B$, when $u_0B$ approaches zero.

### 2. Fundamental Equations, Impedance Matrix, and Characteristic Matrix

The cavity treated in this paper is a cylindrical one, in which only doubly degenerate $TE_{11n}$ modes are excited. As a general case, we consider a cavity which has two inputs meeting at an angle $\theta$ with each other as shown in Fig. 1. When the skin depth of a semiconductor sample is larger than the sample thickness, the semiconductor is set on the symmetry axis in the interior of the cavity (*Model A*). When the skin depth is far smaller than the sample thickness, a small central part of the circular wall of the cavity is replaced by a semiconductor sample (*Model B*). The semiconductor sample is placed so

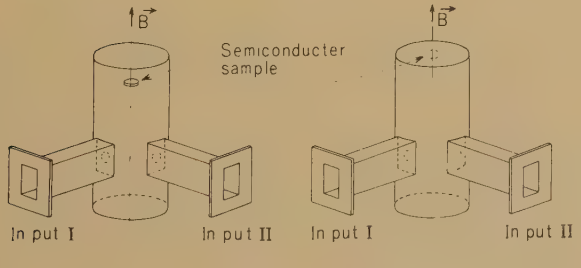


(a) *Mopel A*, in which a semiconductor sample is placed on the symmetry axis in the cavity.

(b) *Model B*, in which a semiconductor sample is substituted for a small central part of the circular wall of the cavity.

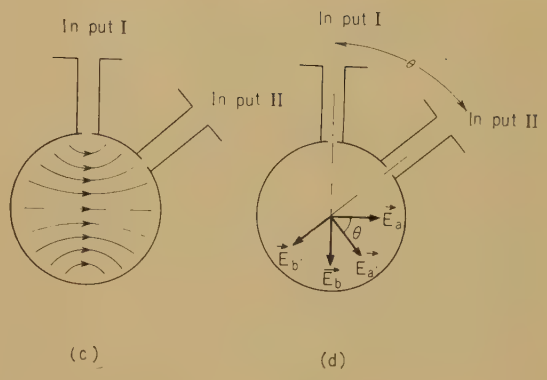


(c) Arrows show $E_a$ vector.

(d) The relations between input I and input II.

**Fig. 1**—Double mode cavity.

that the axial symmetry of the cavity is not broken. Then, following Slater, the radiation fields in the cavity are expanded in terms of the doubly degenerate $TE_{11n}$ modes, and the fundamental equations are as follows.

$$\left.\begin{aligned} \boldsymbol{E} &= e_a\boldsymbol{E}_a + e_b\boldsymbol{E}_b \\ \boldsymbol{H} &= j\sqrt{\varepsilon/\mu}\,(e_a\boldsymbol{H}_a + e_b\boldsymbol{H}_b) \end{aligned}\right\} \tag{2.1}$$

$$\left.\begin{aligned} k_i\int \boldsymbol{E}\cdot\boldsymbol{E}_i^*\,dv + (d/dt)\int \mu\boldsymbol{H}\cdot\boldsymbol{H}_i^*\,dv &= -\int_S (\boldsymbol{n}\times\boldsymbol{E})\cdot\boldsymbol{H}_i^*\,da \\ k_i\int \boldsymbol{H}\cdot\boldsymbol{H}_i^*\,dv - (d/dt)\int \varepsilon\boldsymbol{E}\cdot\boldsymbol{E}_i^*\,dv &= \int \boldsymbol{j}\cdot\boldsymbol{E}_i^*\,dv - \int_{S'} (\boldsymbol{n}\times\boldsymbol{H})\cdot\boldsymbol{E}_i^*\,da \end{aligned}\right\} \tag{2.2}$$

where

$\boldsymbol{E}_a$, $\boldsymbol{E}_b$: orthonormal $TE_{11n}$ modes

$e_a$, $e_b$: amplitudes of $a$ and $b$ modes

$k_a$, $k_b$: eigenvalues of $a$ and $b$ modes, which are equal in this case

$S$: surface of the cavity wall consisting of the conductor

$S'$: surface of the cavity wall, where input wave guides are connected. It consists of two parts $S_1'$ and $S_2'$

$i$: notation referring to $a$ and $b$.

In these equations, irrotational parts of the fields, which have not the property of wave propagation are neglected. The current $\boldsymbol{j}$ in Eq. (2.2) has the value given by Eq. (1.3) in the semiconductor sample and is zero elsewhere for *Model A*. The surface integral over $S$ gives the energy loss due to the current in the wall. For *Model B*, $\boldsymbol{E}$ in the integral over $S$ is given by Eq. (1.14) over the part of the wall replaced by the conductive semiconductor sample. The integral over $S'$ gives the coupling between cavity modes and input wave guides. From Eqs. (2.2), the following equation is obtained:

$$\mu\frac{d^2}{dt^2}\int\varepsilon\boldsymbol{E}\cdot\boldsymbol{E}_i^*dv+k_i^2\int\boldsymbol{E}\cdot\boldsymbol{E}_i^*dv$$
$$=-\mu\frac{d}{dt}\left\{j\boldsymbol{E}_i^*dv-\int_{S'}(\boldsymbol{n}\times\boldsymbol{H})\boldsymbol{E}_i^*da\right\}$$
$$-k_i\int_S(\boldsymbol{n}\times\boldsymbol{E})\boldsymbol{H}_i^*da \qquad (2.3)$$

Modes $a$ and $b$ are chosen so that mode $a$ couples with input I, but mode $b$ does not. Then $\boldsymbol{E}_a$ and $\boldsymbol{E}_b$ on $S_1'$ are expressed by

$$\boldsymbol{E}_a=v_{a1}\boldsymbol{E}_{t1},\qquad \boldsymbol{E}_b=0 \qquad (2.4)$$

where $v_{a1}$ is a coupling constant between mode $a$ in the cavity and mode $t_1$ in the input I wave guide in which only the dominant $TE_{10}$ mode of a rectangular wave guide can propagate. Next, we choose the $a'$ and the $b'$ modes which have the same relations with input II as the $a$ and the $b$ modes have with input I. (See Fig. 1 (d)).

$$\boldsymbol{E}_{a'}=v_{a'2}\boldsymbol{E}_{t2},\quad \boldsymbol{E}_{b'}=0. \qquad (2.5)$$

The relations between $\boldsymbol{E}_a$, $\boldsymbol{E}_b$ and $\boldsymbol{E}_{a'}$, $\boldsymbol{E}_{b'}$ may be derived from the relation shown in Fig. 1 (d) and the properties of the $TE_{11n}$ modes.[4]

$$\begin{aligned}\boldsymbol{E}_a&=\boldsymbol{E}_{a'}\cos\theta-\boldsymbol{E}_{b'}\sin\theta\\ \boldsymbol{E}_b&=\boldsymbol{E}_{a'}\sin\theta+\boldsymbol{E}_{b'}\cos\theta.\end{aligned} \qquad (2.6)$$

From these relations, we can derive the following relations:

$$\begin{aligned}e_a&=e_{a'}\cos\theta-e_{b'}\sin\theta\\ e_b&=e_{a'}\sin\theta+e_{b'}\cos\theta\end{aligned} \qquad (2.7)$$

where $e_{a'}$ and $e_{b'}$ are the expansion coefficients of the radiation fields in terms of the $a'$ and the $b'$ modes. As the next step, currents and voltages in the input wave guides are defined in the same manner as Slater did. That is,

$$\boldsymbol{E}=V_l\boldsymbol{E}_{tl} \qquad (2.8)$$

$$\boldsymbol{H}=i_lZ_{l0}\boldsymbol{H}_{tl} \qquad (2.8)'$$

on the surface $S_l'$.

For *Model A*, it is assumed here that the fields in the sample are parallel and uniform. And in addition, because the axial symmetry is preserved even when the sample is inserted, the depolarizing factors are the same for all $TE_{11n}$ modes; therefore the fields in the sample will be equal, whichever mode may be excited. For *Model B*, the same assumptions as for *Model A* are made. For example, it is assumed that the currents are parallel and uniform; and that the structure has axial symmetry.

On these assumptions, Eq. (2.3) is rewritten in terms of $e_a$, $e_b$, $e_{a'}$, and $e_{b'}$ supposing time variation to be $e^{j\omega t}$. That is,

$$\left.\begin{aligned}M_0e_a+M_1e_b&=\frac{1}{\varepsilon_0\omega_0}\{v_{a1}i_1+(v_{a'2}\cos\theta)i_2\}\\ M_0e_{a'}+M_1e_{b'}&=\frac{1}{\varepsilon_0\omega_0}\{(v_{a1}\cos\theta)i_1+v_{a'2}i_2\}\end{aligned}\right\} \qquad (2.9)$$

where $\omega_0=\omega_a=\omega_b=k_a/\sqrt{\varepsilon_0\mu_0}=k_b/\sqrt{\varepsilon_0\mu_0}$ is the resonance angular frequency of the hollow cavity, and $M_0$ and $M_1$ are expressed in the following form.

a) *Model A*

$$M_0=j\left(\frac{\omega}{\omega_0}-\frac{\omega_0}{\omega}\right)+j(\kappa-1)\,E_0\cdot E_0'\,v_s$$

$$+(1+j)\int_S \frac{\delta}{2} |H_a|^2 da + \frac{1}{\varepsilon_0\omega_0}\sigma_0 |E_0'|^2 v_s \tag{2.10}$$

$$M_1 = -\frac{1}{\varepsilon_0\omega_0}\sigma_1 |E_0'|^2 v_s \tag{2.11}$$

where

$\kappa$: dielectric constant of the semiconductor sample
$E_0'$: the value of $\boldsymbol{E}_a$ in the sample when the sample is in the cavity
$E_0$: the value of $\boldsymbol{E}_a$ at the position of the sample when the sample is absent
$\delta$: the skin depth of the wall
$v_s$: the volume of the sample.

In Eq. (2.10), the second and third terms express the shift of the resonance frequency due to the sample and the wall, and the fourth and fifth terms express the losses due to the sample and the wall. If we denote the losses due to the sample and the wall by $1/Q_s$ and $1/Q_\omega$ respectively, and imaginary parts are collected into one term; Eqs. (2.10) and (2.11) can be expressed simply as

$$M_0 = j\frac{2\Delta\omega}{\omega_0} + \frac{1}{Q_s} + \frac{1}{Q_\omega} \tag{2.12}$$

$$M_1 = \frac{\sigma_1}{Re(\sigma_0)} \cdot \frac{1}{Q_s} \tag{2.13}$$

where

$$\frac{1}{Q_s} = \frac{Re(\sigma_0)}{\varepsilon_0\omega_0} \cdot |E_0'|^2 v_s, \quad \frac{1}{Q_\omega} = \int_S \frac{\delta}{2} \cdot |H_a|^2 da$$

and

$$\Delta\omega = \omega - \omega_0 + \frac{\omega_0}{2}\left\{(\kappa-1)|E_0 \cdot E_0'|v_s + \int_S \frac{\delta}{2} \cdot |H_a|^2 da + \frac{I_m(\sigma_0)}{\varepsilon_0\omega_0} \cdot |E_0'|^2 v_s\right\}.$$

b) *Model B*

$$M_0 = j\left(\frac{\omega}{\omega_0} - \frac{\omega_0}{\omega}\right)$$

$$+(1+j)\int_S \frac{\delta}{2} \cdot |H_a|^2 da + \frac{Z_0}{\mu_0\omega_0} \cdot |H_0|^2 s \tag{2.14}$$

$$M_1 = -\frac{Z_1}{\mu_0\omega_0} \cdot |H_0|^2 s \tag{2.15}$$

where $H_0$ is the value of $\boldsymbol{H}_a$ at the central part of the circular wall, and $s$ is the surface area of the sample. Eqs. (2.14) and (2.15) may be reduced to simpler forms by the use of the losses due to the sample and the wall, $1/Q_s$ and $1/Q_\omega$ respectively.

$$M_0 = j\frac{2\Delta\omega}{\omega_0} + \frac{1}{Q_s} + \frac{1}{Q_\omega} \tag{2.16}$$

$$M_1 = -\frac{Z_1}{Re(Z_0)} \cdot \frac{1}{Q_s} \tag{2.17}$$

where,

$$\frac{1}{Q_s} = \frac{Re(Z_0)}{\omega_0\mu_0} \cdot |H_0|^2 s, \quad \frac{1}{Q_\omega} = \int_S \frac{\delta}{2} \cdot |H_a|^2 da$$

and

$$\Delta\omega = \omega - \omega_0 + \frac{\omega_0}{2}\left\{\frac{I_m(Z_0)}{\omega_0\mu_0} \cdot |H_0|^2 s + \int_S \frac{\delta}{2} \cdot |H_a|^2 da\right\}.$$

Eqs. (2.9) are easily solved for $e_a$ and $e_{a'}$ with the aid of Eqs. (2.7) as follows:

$$\left.\begin{aligned} e_a &= \frac{1}{M_0^2 + M_1^2}\left\{\frac{v_{a1}M_0}{\varepsilon_0\omega_0} i_1 + \frac{v_{a'2}(M_0\cos\theta - M_1\sin\theta)}{\varepsilon_0\omega_0} i_2\right. \\ e_{a'} &= \frac{1}{M_0^2 + M_1^2}\left\{\frac{v_{a1}(M_0\cos\theta + M_1\sin\theta)}{\varepsilon_0\omega_0} i_1\right. \\ &\quad \left.\left. + \frac{v_{a'2}M_0}{\varepsilon_0\omega_0} i_2 \right\}. \right. \end{aligned}\right\} \tag{2.18}$$

Eqs. (2.18) are rewritten as an impedance matrix, by making use of the definition (2.8), which is equivalent to $V_1 = v_{a1}e_a$, $V_2 = v_{a'2}e_{a'}$. The definitions

$$\frac{1}{Q_{ex1}}=\frac{v_{a1}^2}{\varepsilon_0\omega_0 Z_{10}}=M_{Q1}$$

and

$$\frac{1}{Q_{ex2}}=\frac{v_{a'2}^2}{\varepsilon_0\omega_0 Z_{20}}=M_{Q2}$$

are also used.

$$\begin{pmatrix} V_1 \\ V_2 \end{pmatrix}=\begin{pmatrix} Z_{11} & Z_{12} \\ Z_{21} & Z_{22} \end{pmatrix}\begin{pmatrix} i_1 \\ i_2 \end{pmatrix}$$

$$=\frac{1}{M_0^2+M_1^2}\begin{pmatrix} M_0M_{Q1}Z_{10}, & (M_0\cos\theta-M_1\sin\theta)\sqrt{M_{Q1}M_{Q2}Z_{10}Z_{20}} \\ (M_0\cos\theta+M_1\sin\theta)\sqrt{M_{Q1}M_{Q2}Z_{10}Z_{20}}, & M_0M_{Q2}Z_{20} \end{pmatrix}\begin{pmatrix} i_1 \\ i_2 \end{pmatrix}. \qquad (2.19)$$

The impedance matrix can be transformed into the $S$-matrix easily. If we express the incoming and the outgoing components by $(I_1^+, I_2^+)$ and $(I_1^-, I_2^-)$, they are related to $(V_1, V_2)$ and $(i_1, i_2)$ in the following manner:

$$\left.\begin{aligned} \frac{V_1}{\sqrt{Z_{10}}}&=I_1^++I_1^-, \quad \sqrt{Z_{10}}\,i_1=I_1^+-I_1^-, \\ \frac{V_2}{\sqrt{Z_{20}}}&=I_2^++I_2^-, \quad \sqrt{Z_{20}}\,i_2=I_2^+-I_2^-. \end{aligned}\right\} \qquad (2.20)$$

From Eqs. (2.19) and relations (2.20), the $S$-matrix of the cavity is derived as

$$\begin{pmatrix} I_1^- \\ I_2^- \end{pmatrix}=\frac{1}{(M_0M_{Q1}+M_0^2+M_1^2)(M_0M_{Q2}+M_0^2+M_1^2)-(M_0^2\cos^2\theta-M_1^2\sin^2\theta)M_{Q1}M_{Q2}}$$

$$\times\begin{pmatrix} (M_0M_{Q1}-M_0^2-M_1^2)(M_0M_{Q2}+M_0^2+M_1^2)-(M_0^2\cos^2\theta-M_1^2\sin^2\theta)M_{Q1}M_{Q2}, & \\ 2(M_0^2+M_1^2)(M_0\cos\theta-M_1\sin\theta)\sqrt{M_{Q1}M_{Q2}} & \\ 2(M_0^2+M_1^2)(M_0\cos\theta+M_1\sin\theta)\sqrt{M_{Q1}M_{Q2}}, & \\ (M_0M_{Q1}+M_0^2+M_1^2)(M_0M_{Q2}-M_0^2-M_1^2)-(M_0^2\cos^2\theta-M_1^2\sin^2\theta)M_{Q1}M_{Q2} & \end{pmatrix}\begin{pmatrix} I_1^+ \\ I_2^+ \end{pmatrix}. \qquad (2.21)$$

## 3. Interesting Special Cases of the $S$-Matrix

### 3.1. *Case* I*

$$\theta=\pi/2.$$

In this case, the $S$-matrix is reduced to

$$\begin{pmatrix} a_{11} & a_{12} \\ a_{21} & a_{22} \end{pmatrix}$$

$$=\begin{pmatrix} \dfrac{(M_{Q1}-M_0)(M_{Q2}+M_0)-M_1^2}{(M_{Q1}+M_0)(M_{Q2}+M_0)+M_1^2}, & \dfrac{-2M_1\sqrt{M_{Q1}M_{Q2}}}{(M_{Q1}+M_0)(M_{Q2}+M_0)+M_1^2} \\ \dfrac{2M_1\sqrt{M_{Q1}M_{Q2}}}{(M_{Q1}+M_0)(M_{Q2}+M_0)+M_1^2}, & \dfrac{(M_{Q1}+M_0)(M_{Q2}-M_0)-M_1^2}{(M_{Q1}+M_0)(M_{Q2}+M_0)+M_1^2} \end{pmatrix}. \qquad (3.1)$$

Eq. (3.1) is reduced further to the simpler form in the limit of the weak magnetic field. That is,

$$\begin{pmatrix} a_{11} & a_{12} \\ a_{21} & a_{22} \end{pmatrix}$$

$$=\begin{pmatrix} \dfrac{2M_{Q1}}{M_{Q1}+M_0}-1, & \dfrac{-2M_1\sqrt{M_{Q1}M_{Q2}}}{(M_{Q1}+M_0)(M_{Q2}+M_0)} \\ \dfrac{2M_1\sqrt{M_{Q1}M_{Q2}}}{(M_{Q1}+M_0)(M_{Q2}+M_0)}, & \dfrac{2M_{Q2}}{M_{Q2}+M_0}-1 \end{pmatrix}$$

* The formulae in this case are applicable to the double mode cavity without axial symmetry, for example, to a rectangular double mode cavity.

$$= \begin{pmatrix} \dfrac{2\dfrac{1}{Q_{ex1}}}{2j\dfrac{\Delta\omega}{\omega_0}+\dfrac{1}{Q_s}+\dfrac{1}{Q_\omega}+\dfrac{1}{Q_{ex1}}}-1, & \dfrac{-2\dfrac{\sigma_1}{\mathrm{Re}(\sigma_0)}\cdot\dfrac{1}{Q_s}\cdot\dfrac{1}{\sqrt{Q_{ex1}Q_{ex2}}}}{\left(2j\dfrac{\Delta\omega}{\omega_0}+\dfrac{1}{Q_s}+\dfrac{1}{Q_\omega}+\dfrac{1}{Q_{ex1}}\right)\left(2j\dfrac{\Delta\omega}{\omega_0}+\dfrac{1}{Q_s}+\dfrac{1}{Q_\omega}+\dfrac{1}{Q_{ex2}}\right)} \\ \dfrac{2\dfrac{\sigma_1}{\mathrm{Re}(\sigma_0)}\cdot\dfrac{1}{Q_s}\cdot\dfrac{1}{\sqrt{Q_{ex1}Q_{ex2}}}}{\left(2j\dfrac{\Delta\omega}{\omega_0}+\dfrac{1}{Q_s}+\dfrac{1}{Q_\omega}+\dfrac{1}{Q_{ex1}}\right)\left(2j\dfrac{\Delta\omega}{\omega_0}+\dfrac{1}{Q_s}+\dfrac{1}{Q_\omega}+\dfrac{1}{Q_{ex2}}\right)}, & \dfrac{2\dfrac{1}{Q_{ex2}}}{2j\dfrac{\Delta\omega}{\omega_0}+\dfrac{1}{Q_s}+\dfrac{1}{Q_\omega}+\dfrac{1}{Q_{ex2}}}-1 \end{pmatrix} \tag{3.2}$$

Eq. (3.2) corresponds to *Model A*. For *Model B*, the quantity in the numerator $\sigma_1/\mathrm{Re}(\sigma_0)$ should be replaced by $-Z_1/\mathrm{Re}(Z_0)$. Eq. (3.2) shows that $a_{11}$ and $a_{22}$ are the same reflection coefficients as those of the single mode cavity; $a_{12}$ and $a_{21}$, the transmission coefficients, are proportional to the off-diagonal components of the conductivity. Therefore *Case* I is appropriate to the measurement of the Hall mobility in the microwave region.

For example, in *Model A*, the procedures of measurement are as follows. The cavity with $Q_{ex1}=Q_{ex2}=Q_{ex}$ is used for simplicity. The reflection coefficients are measured with and without a sample, in the absence of a magnetic field. From the coefficients, the ratios $Q_\omega/Q_{ex}$ and $Q_s/Q_{ex}$ are deduced. Then the measurement of the transmission coefficient under the application of magnetic field gives $\sigma_1/\mathrm{Re}(\sigma_0)$ which is equal to $u_0B$. In the case of high field, Eq. (3.1) must be used and the procedure is somewhat complicated.

The matrix (3.1) is shown to be the same as that of two single mode cavities connected symmetrically with each other by an anti-symmetric circuit element inserted between them (See Appendix and Fig. 2).

### 3.2. *Case* II

$0<\theta<\pi/2$ and one of the off-diagonal components of the matrix vanishes.

The condition in *Case* II corresponds to the isolator condition. The isolator condition, $a_{12}=0$, is reduced to

$$M_0\cos\theta=M_1\sin\theta. \tag{3.3}$$

Under condition (3.3), the $S$-matrix becomes

$$\begin{pmatrix} a_{11} & a_{12} \\ a_{21} & a_{22} \end{pmatrix} = \begin{pmatrix} \dfrac{M_Q-(1+\cot^2\theta)M_0}{M_Q+(1+\cot^2\theta)M_0}, & 0 \\ \dfrac{4(1+\cot^2\theta)M_0M_Q\cos\theta}{\{M_Q+(1+\cot^2\theta)M_0\}^2}, & \dfrac{M_Q-(1+\cot^2\theta)M_0}{M_Q+(1+\cot^2\theta)M_0} \end{pmatrix} \tag{3.4}$$

This formula is formed on the assumption that $1/Q_{ex1}=1/Q_{ex2}=M_{Q1}=M_{Q2}=M_Q$. In the following, we will treat *Model A* and *Model B* respectively on the assumption that $\omega\tau\ll1$.

a) *Model A*

For this model, $M_1$ is real; and from condition (3.3), $M_0$ must be real also. In such a case, the amplitude transmission coefficient $t(=a_{21})$ is real. The maximum transmission

condition is achieved if $M_Q=(1+\cot^2\theta)M_0$. Then, $t=\cos\theta$, and the power transmission coefficient $T=|t|^2=\cos^2\theta$. From these conditions, the $S$-matrix takes the form

$$\begin{pmatrix} a_{11} & a_{12} \\ a_{21} & a_{22} \end{pmatrix}=\begin{pmatrix} 0 & 0 \\ \cos\theta & 0 \end{pmatrix}.$$

In this case, the reflection coefficient vanishes, and the cavity is matched to both inputs.

b) *Model B*

In this model, $M_1=-(1+j)/\sqrt{2}\ \mathrm{sign}\,(u_0B)\times|M_0|$, so that the condition $M_0\cos\theta=M_1\sin\theta$ implies that $\mathrm{sign}\,(u_0B)=-1$, for $0<\theta<\pi/2$, and $M_0$ must have the form $M_0=(1+j)/\sqrt{2}\times|M_0|$. The transmission coefficient $t$ includes an imaginary part, and the power transmission coefficient $T$ has a maximum of $1/(2+\sqrt{2})^2\cos^2\theta$ at $M_Q=(1+\cot^2\theta)|M_1|$. Then the matrix becomes

$$\begin{pmatrix} \dfrac{\sqrt{2}-1-j}{\sqrt{2}+1+j}, & 0 \\ \dfrac{(1+j)\sqrt{2}}{(\sqrt{2}+1+j)^2}\cos\theta, & \dfrac{\sqrt{2}-1-j}{\sqrt{2}+1+j} \end{pmatrix}.$$

c) *Numerical Examples of Model A*

Now, some numerical examples will be given:

1) For $n$-type Ge at room temperature, typical values are $u_0=0.3\ \mathrm{m^2/volt\cdot sec}$, $\rho=0.1\ \Omega\cdot\mathrm{m}$, and $\sigma_1/\sigma_0=u_0B=0.15$ when $B=0.5\ \mathrm{Wb/m^2}$. If $Q_\omega=3{,}000$ and $Q_s=1{,}000$, then

$$\frac{M_1}{M_0}=\frac{\dfrac{\sigma_1}{\sigma_0}\dfrac{1}{Q_s}}{\dfrac{1}{Q_\omega}+\dfrac{1}{Q_s}}=\frac{\dfrac{0.15}{1{,}000}}{\dfrac{1}{3{,}000}+\dfrac{1}{1{,}000}}\sim 0.11$$

$\cos\theta\sim 0.1$ $T\sim 1/100$ $1/Q_{ex}\sim 1/750$.

2) For $n$-type Ge at liquid $N_2$ temperature, typical values are $u_0=4\ \mathrm{m^2/volt\cdot sec}$, $\rho=0.05\ \Omega\text{-m}$ and $\sigma_1/\sigma_0=2$ when $B=0.5\ \mathrm{Wb/m^2}$. If $Q_\omega=5{,}000$ and $Q_s=1{,}000$, then

$$M_1/M_0\sim 1.67,\quad \cos\theta\sim 0.86\quad \theta\sim 31^\circ,$$

$$T\sim 0.74,\quad 1/Q_{ex}\sim 1/220.$$

**Concluding Remarks**

The properties of the cavity discussed in this paper in terms of the $S$-matrix may be discussed also in terms of the impedance matrix. But the former matrix is sometimes superior, because its components are directly connected with measurable quantities. For example, $a_{12}=0$ means that the transmission from input II to input I vanishes; that is, the cavity acts as an isolator, if $a_{21}\neq 0$. And $a_{21}$ gives the transmission coefficient of the isolator.

The transmission coefficient of the cavity used as an isolator never attains unity in principle. This is the fate of the isolator, which utilizes conductivity tensor as a working agent. Loss enters inevitably.

**Acknowledgement**

The author would like to express his sincere thanks to Dr. T. Niimi for his continual encouragement and to Dr. B. Oguchi for his valuable suggestions. The author also wishes to give thanks to Mr. Y, Kanai and Mr. R. Nii for their many valuable discussions and helpful advices during the course of this work.

**Appendix**

**Equivalent Circuit of *Case* I**

A single mode cavity with two inputs may be characterized by the following $S$-matrix:

$$\begin{pmatrix} a_{11} & a_{12} \\ a_{21} & a_{11} \end{pmatrix}$$

$$=\begin{pmatrix} \dfrac{2\dfrac{1}{Q_{ex1}}}{2j\dfrac{\Delta\omega}{\omega_0}+\dfrac{1}{Q_0}+\dfrac{1}{Q_{ex1}}+\dfrac{1}{Q_{ex2}}}-1, & \end{pmatrix}$$

$$\begin{pmatrix} \dfrac{2\dfrac{1}{\sqrt{Q_{ex1}Q_{ex2}}}}{2j\dfrac{\Delta\omega}{\omega_0}+\dfrac{1}{Q_0}+\dfrac{1}{Q_{ex1}}+\dfrac{1}{Q_{ex2}}} & \dfrac{2\dfrac{1}{\sqrt{Q_{ex1}Q_{ex2}}}}{2j\dfrac{\Delta\omega}{\omega_0}+\dfrac{1}{Q_0}+\dfrac{1}{Q_{ex1}}+\dfrac{1}{Q_{ex2}}} \\ \dfrac{2\dfrac{1}{Q_{ex2}}}{2j\dfrac{\Delta\omega}{\omega_0}+\dfrac{1}{Q_0}+\dfrac{1}{Q_{ex1}}+\dfrac{1}{Q_{ex2}}} & \end{pmatrix} \tag{A.1}$$

where $1/Q_0$ expresses the loss due to the current in the wall and in the interior of the cavity; $1/Q_{ex1}$ and $1/Q_{ex2}$ correspond to the coupling to input I and to input II respectively.

If two cavities, with the same $\omega_0$ and $Q$'s, and an antisymmetric circuit element having the $S$-matrix $\begin{pmatrix} 0 & 1 \\ -1 & 0 \end{pmatrix}$ are connected as shown in Fig. 2, then the $S$-matrix of the whole system is easily calculated and the results are as follows:

$$\begin{pmatrix} a^*_{11} & a^*_{12} \\ a^*_{21} & a^*_{22} \end{pmatrix} = \begin{pmatrix} \dfrac{-\left(2j\dfrac{\Delta\omega}{\omega_0}+\dfrac{1}{Q_0}\right)^2+\dfrac{1}{Q_{ex}{}^2}-\dfrac{1}{Q_c{}^2}}{\left(2j\dfrac{\Delta\omega}{\omega_0}+\dfrac{1}{Q_0}+\dfrac{1}{Q_{ex}}\right)^2+\dfrac{1}{Q_c{}^2}} & \dfrac{-2\dfrac{1}{Q_c}\dfrac{1}{Q_e}}{\left(2j\dfrac{\Delta\omega}{\omega_0}+\dfrac{1}{Q_0}+\dfrac{1}{Q_{ex}}\right)^2+\dfrac{1}{Q_e{}^2}} \\ \dfrac{2\dfrac{1}{Q_c}\dfrac{1}{Q_e}}{\left(2j\dfrac{\Delta\omega}{\omega_0}+\dfrac{1}{Q_0}+\dfrac{1}{Q_{ex}}+\right)^2+\dfrac{1}{Q_c{}^2}} & \dfrac{-\left(2j\dfrac{\Delta\omega}{\omega_0}+\dfrac{1}{Q_0}\right)^2+\dfrac{1}{Q_{ex}{}^2}-\dfrac{1}{Q_c{}^2}}{\left(2j\dfrac{\Delta\omega}{\omega_0}+\dfrac{1}{Q_0}+\dfrac{1}{Q_{ex}}\right)^2+\dfrac{1}{Q_c{}^2}} \end{pmatrix} \tag{A.2}$$

This matrix is exactly the same as Eq. (3.1), if we put

$$\frac{1}{Q_c}=\frac{\sigma_1}{Re(\sigma_0)}\cdot\frac{1}{Q_s}, \qquad \frac{1}{Q_0}=\frac{1}{Q_s}+\frac{1}{Q_\omega}$$

in Eq. (A.2) and

$$\frac{1}{Q_{ex1}}=\frac{1}{Q_{ex2}}=\frac{1}{Q_{ex}}$$

in Eq. (3.1). These considerations show the physical meaning of Eq. (3.1) clearly, that is, the semiconductor sample connects two otherwise mutually independent modes of the cavity.

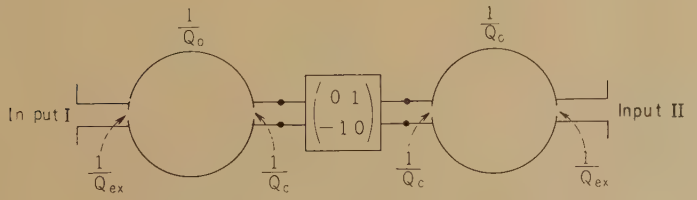


**Fig. 2**—Equivalent circuit of the cavity in *Case* I.

## References


1) J. C. Slater, *Microwave Electronics*, D. Van Nostrand Company, Inc., New York, 1950.
2) S. Tomonaga, T. Miyajima, and K. Shimoda, *Kyokuchotampa Riron Gaisetsu* (in Japanese), Risunaa Co., Tokyo, p. 56, 1950.
3) For the definitions and the derivations of formulae in this section, see Chap. 4 of *Microwave Electronics*, by J. C. Slater.
4) See, for example, J. A. Stratton, *Electro-magnetic Theory*, McGraw-Hill Book Co., Inc., New York, p. 541, 1941.


* * * *

U.D.C. 621.385.64.001

# Energy Build-up in Magnetrons*

*Daijiro KOBAYASHI*†

*The previously published "A New Analysis of Magnetron"[3] has been extended to the theory of the energy build-up in magnetrons. The build-up time is given as $QL/\pi f_0$. By applying this theory, some characteristics of PPM noise are clearly explained.*

## Introduction

The transient phenomena of the energy build-up of magnetron oscillations have been studied by Hunter,[1] Rieke,[2] and others. But, so far as the author knows, the analyses of such build-up behaviors is rather complicated.

The author published "A New Analysis of Magnetron" about a year ago. By applying this theory, it is possible to know how the oscillation builds up when the anode voltage is applied. The build-up time is determined by frequency and by loaded $Q$; and the calculated values are compared with those obtained in Hunter's paper.

On the other hand, the PPM noise of magnetrons has been investigated by many authors, and it has been found that for many magnetrons the lines of constant signal to noise ratio ($S/N$) on Rieke diagram are almost parallel to the lines of constant output power; and fortunately, that the $S/N$ ratio becomes high for that load which gives optimum output power. The reason for such phenomena, however, has not yet been determined.

It would be natural to believe that the more rapidly the oscillation builds up, the better the $S/N$ ratio will be. With such an assumption, the characteristics of the $S/N$ lines on the Rieke diagram can be explained.

* MS received by the Electrical Communication Laboratory, April 20, 1960.

† Electronics Parts Research Section.

## 1. Energy Build-up

According to analysis[3] which the author described before, electronic power $P_e$ to be supplied to the anode by electrons, and circuit power $P_c$ to be drawn from the anode to the outer circuit when the $r$-$f$ voltage $\tilde{V}$ is generated across the anode gaps are given as

$$P_e = C\tilde{V} \tag{1}$$

$$P_c = \frac{\tilde{V}^2}{2Z_0} \tag{2}$$

where $C$ and $Z_0$ are, respectively, the current parameter and the circuit impedance seen from the anode gap. Since $P_e$ is proportional to $\tilde{V}$, while $P_c$ is proportional to $\tilde{V}_2$, their relation will be as shown in Fig. 1.

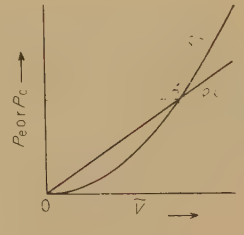


**Fig. 1**—Electronic power and circuit power vs. $r$-$f$ voltage.

At the beginning of the oscillation, a small $r$–$f$ voltage induced by noise appears across

the gap where the electronic power is, as can be seen from Fig. 1, larger than the circuit power; therefore the power supplied to the anode is larger than that derived from the anode. As a result, the remainder of energy is stored in the anode resonator, thereby reinforcing the $r$–$f$ voltage. Thus, the oscillation increases until the $r$–$f$ voltage increases to point A of Fig. 1, where the electronic power and the circuit power will be in equilibrium, thereby sustaining the oscillation.

How $r$–$f$ voltage increases may be seen from the process of growth of the amplitude of $\tilde{V}$. The energy stored in the anode resonator, $W$, may be given as

$$W=\int_0^t (P_e-P_c)dt. \qquad (3)$$

Time $t$ is measured from the instant when the oscillation starts.

From the definition of loaded $Q$, we have

$$Q_L=\frac{\omega_0 W}{P_c}. \qquad (4)$$

where $\omega_0$ is the resonant angular frequency of the anode cavity or the angular frequency of the oscillation. Using Equation (2),

$$W=\frac{Q_L}{2Z_0\omega_0}\tilde{V}^2. \qquad (5)$$

Substituting this into Equation (3) and differentiating by $t$,

$$\frac{Q_L}{Z_0\omega_0}\cdot\frac{d\tilde{V}}{dt}+\frac{\tilde{V}}{2Z_0}-C=0. \qquad (6)$$

The solution of this equation which satisfies the initial condition is given as

$$\tilde{V}=2Z_0C(1-e^{-\frac{\omega_0 t}{2Q_L}}). \qquad (7)$$

The $r$–$f$ voltage increases with the law $(1-e^{-\alpha t})$. The relaxation time $\tau$ is given as

$$\tau=\frac{2Q_L}{\omega_0}=\frac{Q_L}{\pi f_0}. \qquad (8)$$

We will call $\tau$ the "build-up time." The build-up time is proportional to $Q_L$; and it is inversely proportional to $f_0$, the frequency of oscillation.

The solid-line in Fig. 2 shows the rate of increase of $r$–$f$ voltage according to Equation (7). This is the case when an ideal rectilinear pulse is applied to the anode. In practical cases, the pulse to be applied to the anode will also be shaped like this curve, because of the stray capacity and the internal resistance of the pulser. Therefore, the real build-up curve will be affected by the starting curve of the pulse and will take the pulse shape similar to that of the dotted-line* curve in Fig. 2.

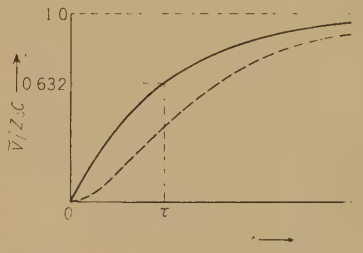


**Fig. 2**—Build-up curve of oscillation.

Usually, the build-up time $\tau$ in conventional magnetrons is about 10 nS(m$\mu$S). It is equivalent to or rather shorter than the build-up time of conventional pulsers. It may be supposed, therefore, that the build-up of the oscillations of the magnetron will be affected rather markedly by the build-up of the pulser.

Hunter[1] calculated the variation of starting time with the variation of loaded $Q$ and compared it with the result obtained by experiment. He obtained the curve shown in Fig. 3. But according to the authors analysis, the build-up time, being proportional to $Q_L$, will be as shown by the dotted-line curve in Fig. 3. Though it is a qualitative explanation, the dotted-line curve agrees well with the measured points.

* For example, the dotted-line curve in Fig. 2 represents the function $(1-e^{-\alpha t})^2$.

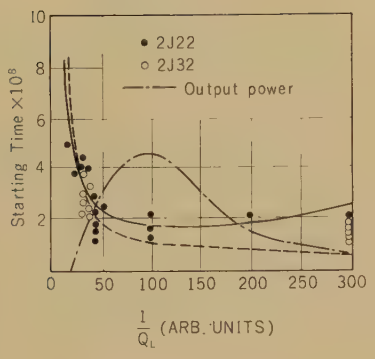


**Fig. 3**—Variation of starting time and output power vs. load.

In Reference (2) the result of an oscillographic observation of the build-up phenomena, where the build-up $Q$ is defined as a measure of steepness of the start of oscillation is given. But, as the photograph shows, the build-up characteristic does not follow the law $e^{\alpha t}$, but takes the form as represented by the dotted-line curve in Fig. 2. The author therefore believes it will be more resonable to use the build-up time given by Equation (8) for the purpose of indicating such steepness.

### 2. PPM Noise

Jitter at the start of the oscillation causes noise in PPM communication system. Signal-to-noise ratio has been measured for various load conditions of the magnetron, and, as a result, it is known that the lines of equal $S/N$ ratio when plotted on a Rieke diagram will be almost parallel to the lines of constant power output. Generally, the higher the output power, the better the $S/N$ ratio was obtained. An example is shown in Fig. 4, which represents the result of a measurement made with an M-750, a magnetron for PPM transmitters in the 4,000 Mc band. The cause of such phenomena is still not clear.

Let us try to explain this by way of application of the build-up time analysis. Since both the top and the bottom of the magnetron pulse are removed by the limiter in the receiver, ordinary AM noise will not cause PPM noise if the pulse is perfectly square. But, if the leading edge of the pulse is inclined, AM noise on this part of the pulse will cause PPM noise. Therefore, it would be natural to belive that the more rapidly $r$-$f$ voltage increases, the better the $S/N$ ratio will be.

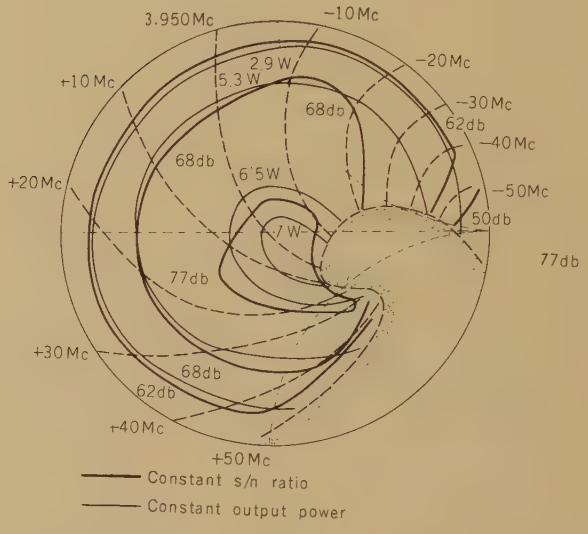


**Fig. 4**—Relation of lines of constant $S/N$ ratio to lines of constant output power on a Rieke diagram.

According to the aforementioned analysis[3] of magnetrons, the output power $P$ of a magnetron is given as

$$P=\frac{2C^2G_a}{G_a^2+B_a^2}\cdot\frac{g}{g+(Q_e/Q_u)} \tag{9}$$

$$G_a=\frac{N(\text{or } 2N)}{Z_{01}Q_L}$$

$$B_a=\frac{N(\text{or } 2N)}{Z_{01}}\left(\frac{f}{f_0}-\frac{f_0}{f}+\frac{b}{Q_e}\right).$$

The first term of Equation (9) represents the electronic power, and the second term the circuit efficiency. $G_a$ and $B_a$ are respectively the conductance and the susceptance of the anode as seen from the resonator gap. $Z_{01}$

and $2N$ are respectively the gap impedance and the number of slots in the anode. The parenthesis is chosen according to whether a rising sun magnetron or other type of magnetron is contemplated. And, $g$ and $b$ are the conductance and the susceptance of the load.

On the other hand, the loaded $Q$ is given as

$$Q_L^{-1} = \frac{1}{Q_u} + \frac{g}{Q_e} \qquad (10)$$

where $Q_u$ and $Q_e$ are unloaded $Q$ and external $Q$, respectively. So, the abscissa of Fig. 3 will correspond to $g$. By making use of Equations (9) and (10), the relation between $P$ and $g$ can be obtained as shown by the dot-dash-line curve in Fig. 3.

As can be seen clearly from this figure, as the output power increases, the build-up time decreases; thus making the $S/N$ ratio increase. It should be noted that the right hand side of Fig. 3. where $g$ is large corresponds to the region of unstable oscillation, where the contours of constant frequency in the Rieke are close to each other.

The empirical result that PPM noise is very liable to be affected by noise from the pulser can be understood easily from the fact that the build-up time of a magnetron is comparable to or even shorter than that of the pulser.

Even when the build-up curve of the pulser is made very sharp and the noise of the pulser is reduced as low as possible, PPM noise will still remain, because the start of the oscillation itself will be triggered by noise. Experiment, however, showed that the jitter at the start of the oscillation had an amplitude smaller than one half cycle of the microwave oscillation. Under such good conditions, the $S/N$ ratio will not be improved by any means such as introducing a priming signal into the magnetron before it is triggered by the pulse.

## Conclusion

Analysis of energy build-up in magnetrons has been accomplished by extending the analysis published previously by the author. The build-up time is proportional to loaded $Q$ and inversely proportional to frequency. Results are compared with those described in the paper of Hunter, and show fairly good agreement. By way of application of this analysis, the behavior of PPM noise has been clearly explained.

The author wishes to acknowledge the helpful discussions made by his colleagues of the Electrical Communication Laboratory of the N.T.T.

## References

(1) L. P. Hunter, "Energy Build-up in Magnetrons," *J. A. Phs.* **17**, 10, p. 833, 1946.
(2) G. B. Collins, *Microwave Magnetrons*, 1st. Fd., p. 339, 1948 McGraw-Hill, N. Y.
(3) D. Kobayashi, "A New Analysis of Magnetron," *Reports of the E.C.L.*, N.T.T., **7**, 4, p. 100, 1959.
(4) D. Kobayashi and S. Hamada, "On the noise of Magnetron M-750," *Reports of the E.C.L.*, N.T.T. **2**, 1, p. 191, 1953.

* * * *

U.D.C. 621.394.3-185.4:681.613.4

# On Stochastic Representations for Incoming Telephone Calls*

*Gisaku NAKAMURA*†

*Stochastic processes representing incoming calls at telephone exchanges are studied generally under the assumption of independency. After introducing some basic concepts, an impulsive process, in which calls can occur only impulsively at some fixed instant, is defined; and its properties are investigated in connection with some other special processes. It is proved that countable impulsive processes are contained in the process satisfying the condition of independency. Consequently, a new process $I_p$ can be derived from the original process by continuing successively subtractions of each impulsive process until no impulsive process is contained in the remainder. After discussing some properties of $I_p$, the stochastic representation for $I_p$ is given in general form. It is shown that the process $I_p$ can be always decomposed to generalized Poisson processes with a variable parameter.*

## Introduction

In many reviews of telephone traffic the assumption is frequently made for theoretical convenience that stochastic processes representing incoming calls at telephone exchanges can be expressed as the Poisson process. There are, however, some cases where this assumption is not satisfied in practice. It is well known that the Poisson process is characterized by three conditions: 1) independency, 2) temporal homogeneity, and 3) rarity. So far as the independency is concerned, it is natural to consider that this condition is satisfied approximately in actual processes since most of incoming calls are mutually independent. There is, however, no reason that the actual processes of calls have to satisfy the two other conditions. For this report, some studies have been made on the processes representing incoming telephone calls under the assumptton of independency. The author believes that there are some new interpretations and stochastic representations in this report, though the general studies of stochastic processes have been made in the field of probability theory.[1]

## 1. Some Definitions

Let $[T+t_1, T+t_1+t)$ be a time interval which is contained in some finite time interval $[T, T')$* and let $a_n(t: T+t_1)$ denote the probability with which $n$ calls occur during $[T+t_1, T+t_1+t)$ in the process. Of course, this notation can be justified since the probability does not depend on any calls occurring before the time $T+t_1$ because of the condition of independency. Then we have

$$\left.\begin{aligned} &\sum_{n=0}^{\infty} a_n(t: T+t_1)=1 \\ &a_n(t: T+t_1)\geqq 0 \quad \text{for} \quad n\geqq 0 \end{aligned}\right\} \tag{1}$$

and

$$\sum_{n=1}^{\infty} n a_n(t: T+t_1)<\infty, \tag{2}$$

where $t_1$ and $t$ satisfy the inequalities

$$\left.\begin{aligned} &0\leqq t_1<T'-T \\ &0<t\leqq T'-T-t_1 \end{aligned}\right\}. \tag{3}$$

* MS in Japanese received by the Electrical Communication Laboratory, March. 11, 1959. Published in the *Kenkyû Zituyôka Hôkoku* (*Electrical Communication Laboratory Technical Journal*), N.T.T., Vol. 9, No. 4, pp. 373-396, 1960.

† Communication Network Section.

* $[T, T')$ signifies a set of $x$ satisfying the inequality $T\leqq x\leqq T'$.

Eq. (2) means that the expected values of the number of calls in finife time intervals are finite. Evidently, this property is satisfied in the actual processes.

$A_n(t:T+t_1)$, defined by

$$A_n(t:T+t_1)=\sum_{m=n+1}^{\infty} a_m(t:T+t_1) \quad \text{for} \quad n\geqq -1, \tag{4}$$

is the probability with which more than $n$ calls occur during $[T+t_1,\ T+t_1+t)$ in the process and plays an important role in the analysis, as does $a_n(t:T+t_1)$. It is easily verified that

$$\left.\begin{aligned} &A_{-1}(t:T+t_1)=1 \\ &A_{n-1}(t:T+t_1)\geqq A_n(t:T+t_1)\geqq 0 \text{ for } n\geqq 0 \end{aligned}\right\}, \tag{5}$$

$$\sum_{n=0}^{\infty} A_n(t:T+t_1)<\infty \tag{6}$$

and

$$a_n(t:T+t_1)=A_{n-1}(t:T+t_1)-A_n(t:T+t_1). \tag{7}$$

Now, let us introduce other probabilities for the process. Since $A_n(t:T+t_1)$ is defined only for intervals, $t$ must be positive. However, if we consider the limit $t\to 0$ in the following way, a new probability for $t=0$ can be derived. To do this, consider two probabilities $A_n(t:T+t_1)$ and $A_n(t':T+t_1)$ where $t>t'>0$. Then

$$A_n(t:T+t_1)\geqq A_n(t':T+t_1) \text{ for } t>t'>0 \tag{8}$$

is obtained, since calls may occur during $[T+t_1+t',\ T+t_1+t)$. Eq. (8) means that the function $A_n(t:T+t_1)$ is monotone decreasing as $t$ decreases. Obviously this function is always non-negative for $t>0$, therefore the limit

$$A_n(0:T+t_1)=\lim_{t\to 0} A_n(t:T+t_1) \quad \text{for} \quad n\geqq -1 \tag{9}$$

exists and satisfies

$$\left.\begin{aligned} &A_{-1}(0:T+t_1)=1 \\ &A_{n-1}(0:T+t_1)\geqq A_n(0:T+t_1)\geqq 0 \text{ for } n\geqq 0 \end{aligned}\right\} \tag{10}$$

and

$$\sum_{n=0}^{\infty} A_n(0:T+t_1)<\infty. \tag{11}$$

Thus, the limit derived above satisfies the same relations for $A_n(t:T+t_1)$ and is suitable for a probability. It is natural to interpret the limit as representing the probability with which more than $n$ calls occur impulsively at the time $T+t_1$. Then the probability $a_n(0:T+t_1)$ corresponding to $a_n(t:T+t_1)$ is derived by

$$a_n(0:T+t_1)=A_{n-1}(0:T+t_1)-A_n(0:T+t_1) \quad \text{for} \quad n\geqq 0. \tag{12}$$

It is obvious that

$$\left.\begin{aligned} &\sum_{n=0}^{\infty} a_n(0:T+t_1)=1 \\ &a_n(0:T+t_1)\geqq 0 \quad \text{for} \quad n\geqq 0 \end{aligned}\right\}, \tag{13}$$

$$\sum_{n=1}^{\infty} n a_n(0:T+t_1)<\infty \tag{14}$$

and

$$a_n(0:T+t_1)=\lim_{t\to 0} a_n(t:T+t_1). \tag{15}$$

Here we note that to derive $a_n(0:T+t_1)$ directly by Eq. (15) is more difficult than by the above method, since the function $a_n(t:T+t_1)$ is not generally a monotone function of $t$.

Sometimes generating functions are available in the analysis of probability theory.[2] Generating functions of sequences $\{a_n(t:T+t_1)\}$ and $\{A_n(t:T+t_1)\}$ are defined by

$$\left.\begin{aligned} &g(s,t:T+t_1)=\sum_{n=0}^{\infty} a_n(t:T+t_1)s^n, \\ &G(s,t:T+t_1)=\sum_{n=0}^{\infty} A_n(t:T+t_1)s^n \end{aligned}\right\} \text{ for } t\geqq 0 \tag{16}$$

respectively and both of them converge absolutely at least in the closed interval $-1 \leqq s \leqq 1$, since the coefficients of $s^n$ are bounded and both series converge for $s=1$. Here, the variable $s$ itself has no significance. It is easily derived that

$$\left.\begin{aligned} a_n(t : T+t_1) &= g^{(n)}(0, t : T+t_1)/n! \\ A_n(t : T+t_1) &= G^{(n)}(0, t : T+t_1)/n! \end{aligned}\right\}, \quad (17)$$

$$\left.\begin{aligned} g(s, 0 : T+t_1) &= \lim_{t \to 0} g(s, t : T+t_1) \\ G(s, 0 : T+t_1) &= \lim_{t \to 0} G(s, t : T+t_1) \end{aligned}\right\}, \quad (18)$$

$$1-g(s, t : T+t_1) = (1-s)G(s, t : T+t_1), \quad (19)$$

and

$$E(n) = g'(1, t : T+t_1) = G(1, t : T+t_1) \quad (20)$$

where $E(n)$ denotes the expected value of the number of calls.

Now, let us derive a fundamental relation of a generating function for the processes satisfying the condition of independency. Let $[T+t_1, T+t_1+t')$ and $[T+t_1+t', T+t_1+t)$ be two adjacent time intervals, and let $a_n(t' : T+t_1)$ and $a_n(t-t' : T+t_1+t')$ denote the probabilities with which $n$ calls occur during above time intervals. Then, by the condition of independency, the probability for $[T+t_1, T+t_1+t)$ can be expressed by

$$a_n(t : T+t_1) = \sum_{m=0}^{n} a_m(t' : T+t_1) \cdot a_{n-m}(t-t' : T+t_1+t') \quad \text{for } t > t' > 0. \quad (21)$$

Multiplying $s^n$ by both sides of Eq. (21) and then summing each side for all positive integers $n$, we obtain the desired relation

$$g(s, t : T+t_1) = g(s, t' : T+t_1) \cdot g(s, t-t' : T+t_1+t_1') \quad \text{for } t > t' > 0. \quad (22)$$

It is important to note that Eq. (22) is only satisfied for $t' > 0$, though the generating function $g(s, t' : T+t_1)$ is defined even for $t'=0$. The reason why we avoid the case $t'=0$ is as follows. If $t' \to 0$, then $[T+t_1, T+t_1+t')$ becomes a point $T+t_1$ and $[T+t_1+t', T+t_1+t)$ becomes an open interval $(T+t_1, T+t_1+t)$. However, the generating functions are not defined for open time intervals. Thus, it is necessary to define probabilities for open intervals too, if we wish to justify Eq. (22) for $t'=0$. This may cause some confusion since probabilities are defined for both open and semi-closed intervals. But the considerations of this limit will play a quite important role later. Then, this problem will be investigated in the next section from another point of view.

The additivity of the expected number of calls can be obtained easily from Eq. (22). Differentiating both sides of Eq. (22) with respect to $s$ and then putting $s=1$, we obtain

$$g'(1, t : T+t_1) = g'(1, t' : T+t_1) + g'(1, t-t' : T+t_1+t') \quad (23)$$

since the relation

$$g(1, t : T+t_1) = 1 \text{ for } t \geqq 0$$

is satisfied identically.

### 2. Decomposition of Process and Impulsive Processes

The processes $I_1, I_2, \cdots\cdots, I_m$ are called mutually independent if the number of calls occurring in any process of them is not affected by other calls. A new process $\sum_{n=1}^{m} I_n$ named compound process can be defined when the $I_m$s are mutually independent. Since the definition can be made inductively by

$$\sum_{n=1}^{m} I_n = \left(\sum_{n=1}^{m-1} I_n\right) + I_m \quad \text{for } m \geqq 3, \quad (24)$$

the consideration is restricted, without loss of generality, to the case in which only two processes $I_1$ and $I_2$ are compounded. Let $b_n(t : T+t_1)$ and $c_n(t : T+t_1)$ denote the probabilities for $I_1$ and $I_2$ respectively. Then the probability $a_n(t : T+t_1)$ for $I_1+I_2$ is defined

by

$$a_n(t:T+t_1)=\sum_{m=0}^{n} b_m(t:T+t_1)\cdot c_{n-m}(t:T+t_1) \quad \text{for} \quad n\geqq 0. \tag{25}$$

Since these newly defined processes satisfy the condition of independency, Eq. (24) is always justified as is pointed out above.

Decompositions of process are defined by the inverse procedures of compounding. It is called that the process $I_0$ is decomposed to proceses $I_1, I_2, \cdots\cdots, I_m$ if we can find mutually independent processes $I_n$s such that

$$I_0=\sum_{n=1}^{m} I_n \quad \text{for} \quad m\geqq 2. \tag{26}$$

Obviously, $I_0$ can be decomposed to $I_1$ and $\sum_{n=2}^{m} I_n$ too, if Eq. (26) is satisfied. Therefore, without loss of generality, the considerations can be restricted to the case in which a process is decomposed to only two mutually independent processes. A useful decomposition can be derived by introducing a process named the null process. The null process is defined by a process in which no call can occur in any time interval. Evidently, the null process satisfies the condition of independency and, furthermore, it does not depend on any other processes. Although the null process seems to be trivial, it plays an important role in this analysis analgous to the role of the integer 0 in arithmetic.

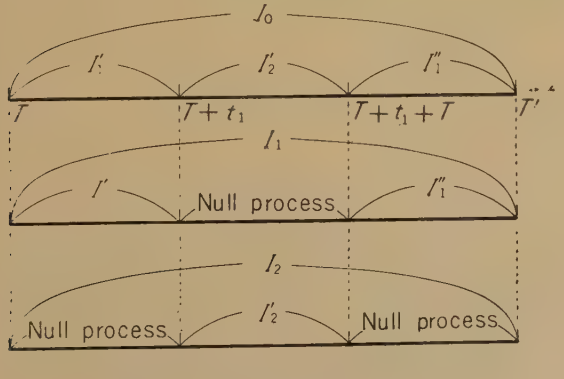


**Fig. 1**—Decomposition of $I_0$.

Now, let us derive the decomposition stated above. Let $[T, T')$ be an arbitrary time interval. Divide it into three subintervals $[T, T+t_1)$, $[T+t_1, T+t_1+t)$ and $[T+t_1+t, T')$, and denote the parts of process $I_0$ in each subinterval by $I_1'$, $I_2'$, and $I_1''$ respectively (see Fig. 1). Then we have

$$g_0(s, T'-T:T)=g_0(s, t_1:T)g_0(s, t:T+t_1)\cdot g_0(s, T'-T-t_1-t:T+t_1+t) \tag{27}$$

where $g_0$ denotes the generating function of $I_0$. If we consider a new process $I_1$ which consists of $I_1'$, $I_1''$ and a null process in $[T+t_1, T+t_1+t)$, then the generating function of $I_1$, say $g_1(s, T'-T:T)$, is represented by

$$g_1(s, T'-T:T)=g_0(s, t_1:T)\cdot g_0(s, T'-T-t_1-t:T+t_1+t). \tag{28}$$

In the same way, considering $I_2$ which consists of $I_2'$ and two null processes in $[T, T+t_1)$ and $[T+t_1+t, T')$ respectively, the generating function of $I_2$ is represented by

$$g_2(s, T'-T:T)=g_0(s, t:T+t_1). \tag{29}$$

Thus we have

$$g_0(s, T'-T:T)=g_1(s, T'-T:T)g_2(s, T'-T:T). \tag{30}$$

Since the processes $I_1$ and $I_2$ are mutually independent, we know that the process $I_0$ can be decomposed to $I_1$ and $I_2$. Here, it is important to note that the generating functions obtained above are all defined for the same interval $[T, T')$. Then, in this case, we can consider the limit $t\to 0$ in Eq. (30), differing from Eq. (22). Thus, considering the limiting case in Eq. (30), $I_0$ can be decomposed to limit processes whose generating functions are represented by $g_0(s, T'-T:T)/g_0(s, 0:T+t_1)$ and $g_0(s, 0:T+t_1)$ respectively. Here we note that the function $g_0(s, T'-T:T)/g_0(s, 0:T+t_1)$ exists even if

$$g_0(s, 0:T+T_1)=0,$$

as is easily proved. The above decomposition of process is reduced to a trivial case if

$$g_0(s, 0 : T+t_1)=1$$

or

$$1-a_0(0 : T+t_1)=A_0(0 : T+t_1)=0 \quad (31)$$

is satisfied, where $a_0(0 : T+t_1)$ denotes the probability for $I_0$. Because, in this case, the process $I_2$ becomes a null process in the whole time interval $[T, T')$ and then $I_0$ is decomposed only to $I_0$ itself and the null process. However, when

$$A_0(0 : T+t_1)>0, \quad (32)$$

the decomposition becomes nontrivial. It is easily verified that calls can occur at the instant $T+t_1$ impulsively in $I_2$ and no call can occur at $T+t_1$ in $I_1$, if Eq. (32) is satisfied.

The limit process $I_2$ obtained above is called an impulsive process at the time $T+t_1$ because of its meaning. It can be imagined that a new process, say $I_p$, can be derived such that

$$B_0(0 : T+t_1)=0 \quad \text{for} \quad 0 \leqq t_1 < T'-T, \quad (33)$$

where $B_0(0 : T+t_1)$ denotes probability for $I_p$, if the decompositions of above type are carried out for every time point satisfying Eq. (32). To justify this statement, however, it is necessary to show that there are only countable points satisfying Eq. (32), since the decompositions can be done one after another. In the next section, some preliminary considerations will be made to prove this countability and some other properties.

### 3. Special Processes

In this section, three special processes will be investigated for the sake of analysis in subsequent sections.

First, let us consider a process whose probability satisfied

$$1>a_n(T'-T : T)=1-a_0(T'-T : T)>0 \quad (34)$$

for a fixed positive integer $n$. This means that $n$ calls must occur invariably in this process if any calls definitely occur during $[T, T')$. Let $[T, T')$ divide into two adjacent subintervals $[T, T+t)$ and $[T+t, T')$. Then there exist the largest number of calls $N_1$ and the smallest number $n_2$ occurring with positive probabilities during $[T, T+t)$. In the same way, there exist $N_2$ and $n_2$ for $[T+t, T')$. Since the relations

$$n=N_1+N_2 \quad \text{and} \quad 0=n_1+n_2$$

are evident by Eq. (34), we obtain

$$N_1=n, \ N_2=0 \quad \text{or} \quad N_1=0, \ N_2=n, \quad (35)$$

as is easily proved. Eq. (35) shows that one of the processes must be a null process. Therefore, moving $t$ from $T'-T$ to 0 continuously, one of following two cases occurs. First,

$$N_2=0 \quad \text{for} \quad t>0 \quad (36)$$

is satisfied and the original process becomes the impulsive process at the time $T$. Second, we can find a point $t_1$ in the open interval $(0, T'-T)$ such that

$$\left.\begin{array}{l} N_2=0 \quad \text{for} \quad t>t_1 \\ N_2=n \quad \text{for} \quad t \leqq t_1 \end{array}\right\}, \quad (37)$$

and the original process becomes the impulsive process at the time $T+t_1$. Thus, we can conclude that the process considered becomes the impulsive process at the time $T+t_1$ contained in $[T, T')$.

Next, let us consider a slightly generalized process, that is

$$\left.\begin{array}{l} a_N(T'-T : T)>0 \\ A_N(T'-T : T)=0 \end{array}\right\} \quad (38)$$

where $N$ is a finite fixed integer. This means that only a finite number of calls can occur during $[T, T')$ in this process. Then, there exist the largest number of calls $N_1$ and $N_2$ occuring with positive probabilities during the subintervals $[T, T+t)$ and $[T+t, T')$ re-

spectively, and the relation

$$N=N_1+N_2 \tag{39}$$

is satisfied. Thus, moving $t$ from $T'-T$ to 0 continuously, either

$$N_2=0 \quad \text{for} \quad t>0 \tag{40}$$

or

$$\left.\begin{aligned} &N_2=0 \quad \text{for} \quad t>t_1 \\ &N_2>0 \quad \text{for} \quad t\leqq t_1 \end{aligned}\right\}, \tag{41}$$

are satisfied. In the former case, it is obvious that the original process becomes the impulsive process at the time $T$. In the latter case, however, the process does not become a single impulsive process unless

$$N_1=0$$

happens. But, in this case, the same procedure derived above is available for the process in $[T, T+t')$. Since

$$N_1<N$$

is satisfied, the original process can be decomposed into finite impulsive processes if the above procedures are repeated successively until the remainder becomes a null process.

Finally, let us consider another type of process in which

$$a_0(T'-T:T)=1-A_0(T'-T:T)=0 \tag{42}$$

is satisfied. This means that calls definitely occur during $[T, T')$ in this process. From Eqs. (42) and (6), we can find an integer $m$ such that

$$\left.\begin{aligned} &A_{m-1}(T'-T:T)=1 \\ &A_m(T'-T:T)<1 \end{aligned}\right\}.$$

Since above equations are equivalent to

$$\left.\begin{aligned} &a_m(T'-T:T)>0 \\ &a_n(T'-T:T)=0 \quad \text{for} \quad n<m \end{aligned}\right\}, \tag{43}$$

there exists the smallest number of calls $m_1$ and $m_2$ occurring with positive probabilities during the subintervals $[T, T+t)$ and $[T+t, T')$ respectively. Clearly,

$$m=m_1+m_2 \tag{44}$$

holds, and either

$$m_2=0 \quad \text{for} \quad t>0 \tag{45}$$

or

$$\left.\begin{aligned} &m_2=0 \quad \text{for} \quad t>t_1 \\ &m_2>0 \quad \text{for} \quad t\leqq t_1 \end{aligned}\right\} \tag{46}$$

are satisfied. In the former case, the impulsive process at the time $T$ can be subtructed from the original process by decomposition and we obtain a process whose probability satisfies

$$b_0(T'-T:T)>0. \tag{47}$$

In the latter case, the impulse process at the time $T+t_1$ is subtracted from the original process and same procedure is repeated for the process in $[T, T+t)$. Since

$$m_1<m,$$

is satisfied, finite impulsive processes can be subtracted from the original process and Eq. (47) is obtained for the remainder also. Thus, we can conclude that the process whose probability satisfies Eq. (47) is always obtained by the subtraction of finite impulsive processes from the original process.

### 4. Countability

In this section we will prove, as we stated in section 2, the countability of points $T+t_1$ satisfying Eq. (32), To begin with, we note that the considerations can be restricted to

$$A_0(T'-T:T)<1 \tag{48}$$

without loss of generality. Because, if

$$A_0(T'-T:T)=1$$

is satisfied, we can obtain Eq. (48) by the subtraction of finite impulsive processes from the original process. It is obvious from Eq. (8) that

$$A_0(t:T)<1 \quad \text{for} \quad 0\leqq t<T'\leqq T \tag{49}$$

if Eq. (48) is satisfied.

Now, let us consider $A_0(t:T)$ as a function of $t$. Since discontinuous points of monotone functions are countable generally, as is well known from the set theory, we can denote discontinuous points of $A_0(t:T)$ by $t_1, t_2, \cdots\cdots$. Then we can find $\delta_\varepsilon$ such that

$$0\leqq A(t+\delta_\varepsilon:T)-A_0(t:T)<\varepsilon$$
$$\text{for} \quad t\neq t_n(n=1,2,\cdots\cdots\cdots) \tag{50}$$

where $\varepsilon$ is an arbitrary positive number. And there are fixed $k_n s$ such that

$$A_0(t_n+\varepsilon:T)-A_0(t_n:T)\geqq k_n>0$$
$$\text{for} \quad n=1,2,\cdots\cdots\cdots. \tag{51}$$

Since the relation

$$A_0(t+\delta_\varepsilon:T)-A_0(t:T)$$
$$=A_0(\delta_\varepsilon:T+t)\{1-A_0(t:T)\}$$

is easily derived, Eq. (50) can be transformed to

$$0\leqq A_0(\delta_\varepsilon:T+t)\{1-A_0(t:T)\}<\varepsilon$$
$$\text{for} \quad t\neq t_n(n=1,2,\cdots\cdots\cdots).$$

Therefore, dividing the above inequality by $\{1-A(t:T)\}$, which is always positive from Eq. (49), we have

$$0\leqq A_0(\delta_\varepsilon:T+t)\leqq\varepsilon/\{1-A_0(t:T)\}$$
$$\text{for} \quad t\neq t_n. \tag{52}$$

Evidently, Eq. (52) means

$$A_0(0:T+t)=0 \quad \text{for} \quad t\neq t_n(n=1,2,\cdots\cdots\cdots). \tag{53}$$

Next, let us consider the discontinuous points $t_n s$. Using a method similar to that used above, it is easily derived that

$$A_0(\varepsilon:T+t_n)\geqq k_n/\{1-A_0(t_n:T)\}>0$$
$$\text{for} \quad n=1,2,\cdots\cdots\cdots. \tag{54}$$

And this means that

$$A_0(0:T+t_n)>0 \quad \text{for} \quad n=1,2,\cdots\cdots\cdots. \tag{55}$$

Thus the desired countability can be established by Eqs. (53) and (55).

Now, we are ready to state a general result concerning impulsive proeesses. There are only countable impulsive processes in any process satisfying the condition of independency, and they are subtracted subsequently from the original process. When all impulsive processes are subtracted from the original process, a new process $I_p$ is obtained whose probability satisfies Eq. (33). Thus, studies remained later are related to the process $I_p$. The two succeeding sections will be devoted to these analyses.

### 6. General Studies on $I_p$

Let us start our discussions from the basic property

$$B_0(0:T+t_1)=0 \quad \text{for} \quad 0\leqq t_1<T'-T. \tag{56}$$

Although the null process satisfies the above equation as a special case, we exclude it from our considerations because of its triviality. Then we can find a time interval $[T+t_1, T+t_1+t)$ contained in $[T, T')$ such that

$$B_0(t:T+t_1)>0. \tag{57}$$

It is obvious that

$$\left.\begin{aligned} &B_0(t:T+t_1)<1 \\ &B_n(t:T+t_1)>0 \quad \text{for} \quad n\geqq 0 \end{aligned}\right\}, \tag{58}$$

otherwise there will be a point $T+t_1+t'$ in $[T+t_1, T+t_1+t)$ such that

$$B_0(0:T+t_1+t')>0 \tag{59}$$

by the results discussed in section 4. Of course, Eq. (59) contradicts Eq. (56). Hence, in this process, both no calls and more than $N$ calls can occur during $[T+t_1, T+t_1+t)$, where $N$ is a positive integer chosen arbitrarily. Eqs. (58) are equivalent to

$$\left.\begin{aligned} &1>b_0(t:T+t_1)>0 \\ &\sum_{n=0}^{N} b_n(t:T+t_1)<1 \end{aligned}\right\}, \tag{60}$$

by the definition

$$b_n(t:T+t_1)=B_{n-1}(t:T+t_1)-B_n(t:T+t_1). \tag{61}$$

Now, let us discuss continuities of $b_n(t:T+t_1)$ concerning the variable $t$. It is evident that the function $b_0(t:T+t_1)$ is continuous for $t$, otherwise $B_0(t:T+t_1)$ will become a discontinuous function and then Eq, (58) will be satisfied. Therefore, the continuity of $b_n(t:T+t_1)$ for all $n(\geqq 0)$ can be verified by induction, since the relation

$$\begin{aligned} &b_n(t+t':T+t_1)-b_n(t:T+t_1) \\ &=-\{1-b_0(t':T+t_1+t)\}b_n(t:T+t_1) \\ &\quad+\sum_{m=1}^{n} b_m(t':T+t_1+t)b_{n-m}(t:T+t_1) \end{aligned}$$

holds identically by the condition of independency. Thus $b_n(\Delta t:T+t_1+t)$ can be represented by

$$\left.\begin{aligned} &b_0(\Delta t:T+t_1+t)=1-\sum_{m=1}^{\infty}\lambda_{0m}(T+t_1+t)\Delta t^m \\ &b_n(\Delta t:T+t_1+t)=\sum_{m=1}^{\infty}\lambda_{nm}(T+t_1+t)\Delta t^m \text{ for } n\geqq 1 \end{aligned}\right\} \tag{62}$$

for small $\Delta t$, and

$$\lambda_{0m}(T+t_1+t)=\sum_{n=1}^{\infty}\lambda_{nm}(T+t_1+t) \quad \text{for} \quad m\geqq 1, \tag{63}$$

$$\lambda_{n1}(T+t_1+t)\geqq 0 \quad \text{for} \quad n\geqq 0 \tag{64}$$

are evident by

$$\sum_{n=0}^{\infty} b_n(\Delta t:T+t_1+t)=1,$$

$$b_n(\Delta t:T+t_1+t)\geqq 0 \quad \text{for} \quad n\geqq 0$$

respectively.

Now, we are ready to investigate the functional form of $b_n(t:T+t_1)$. Using the Eq. (62), it is easily derived that

$$\begin{aligned} &b_n(t+\Delta t:T+t_1)-b_n(t:T+t_1) \\ &=-\sum_{m=1}^{\infty}\lambda_{0m}(T+t_1+t)\Delta t^m b_n(t:T+t_1) \\ &\quad+\sum_{m=0}^{n-1}\sum_{l=1}^{\infty}\lambda_{n-m,l}(T+t_1+t)\Delta t^l b_m(t:T+t_1) \end{aligned}$$

$$\text{for} \quad n\geqq 0, \tag{65}$$

providing

$$\sum_{m=0}^{n-1}\cdot=0 \quad \text{for} \quad n=0.$$

Dividing both sides of Eq. (65) by $\Delta t$ and then putting $t\to 0$, we have

$$\begin{aligned} &db_n(t:T+t_1)/dt=-\lambda_{01}(T+t_1+t)b_n(t:T+t_1) \\ &\quad+\sum_{m=0}^{n-1}\lambda_{n-m,1}(T+t_1+t)b_m(t:T+t_1). \end{aligned} \tag{66}$$

Thus, if we use the generating function defined by

$$g(s,t:T+t_1)=\sum_{n=0}^{\infty} b_n(t:T+t_1)s^n, \tag{67}$$

we can obtain

$$\begin{aligned} &dg(s,t:T+t_1)/dt \\ &=-\sum_{n=0}^{\infty}(1-s^n)\lambda_{n1}(T+t_1+t)g(s,t:T+t_1) \end{aligned} \tag{68}$$

after some calculations. Therefore, using the

initial condition given by

$$g(s, 0: T+t_1)=\sum_{n=0}^{\infty} b_n(0: T+t_1)s^n=1,$$

the final solution can be derived such that

$$g(s, t: T+t_1)$$
$$=\exp\left\{-\sum_{n=1}^{\infty}(1-s^n)\int_0^t \lambda_{n1}(T+t_1+x)dx\right\}. \tag{69}$$

It is, however, not so simple to find the functional form of $b_n(t: T+t_1)$ from Eq. (69), though it can be done theoretically. The meaning of Eq. (69) will be clarified in the next section.

### 7. Temporal Homogeneity and Rarity

In this section, two special types of processes are discussed in connection with $I_p$. First, let us consider the process satisfying further the condition of temporal homogeneity in addition to the condition of independency. It is easily verified that there exists no impulsive process in the process satisfying the condition of temporal homogeneity because of the countability obtained in section 5. Then this process becomes $I_p$ and we can use the results established in the preceding section. Thus we have

$$g(s, t)=\exp\left\{-\sum_{n=1}^{\infty}(1-s^n)\lambda_{n1}t\right\} \tag{70}$$

where $g(s, t)$ is the generating function for the process considered. Thus, in this case, the process can be determined completely when $\lambda_{n1}$s are given for all positive $n$. Putting $t=1$ in Eq. (70), we have a generating function for unit time interval such that

$$g(s, 1)=\exp\left\{-\sum_{n=1}^{\infty}(1-s^n)\lambda_{n1}\right\}. \tag{71}$$

Since $g(s, 1)$ corresponds to a generating function for a discrete probability distribution, we can construct processes satisfying both independency and temporal homogeneity from probability distributions. The followings are some examples for $\lambda_{n1}$ derived from representative distributions.

1) Poisson distribution

$$P_n=e^{-a}a^n/n!, \quad \lambda_{11}=a, \quad \lambda_{n1}=0 \text{ for } n\geqq 2.$$

2) Geometric distribution

$$P_n=p^n(1-p), \quad \lambda_{n1}=p^n/n \text{ for } n\geqq 1.$$

3) Polya distribution

$$p_n=\frac{(1+d)^{-h/d}\Gamma\{(h/d)+n\}\{d/(1+d)\}^n}{n!\Gamma(h/d)},$$

$$\lambda_{n1}=hd^n/nd(1+d)^n \text{ for } n\geqq 1.$$

Next, we shall consider the process satisfying the condition of rarity, in addition to the condition of independency. Usually rarity means that

$$\left.\begin{aligned}&\lambda_{01}(T+t_1+t)=\lambda(T+t_1+t)\\&\lambda_{n1}(T+t_1+t)=0 \text{ for } n\geqq 2\end{aligned}\right\}. \tag{72}$$

Then the generating function of process becomes

$$g(s, t: T+t_1)=\exp\left\{-(1-s)\int_0^t \lambda(T+t_1+x)dx\right\}, \tag{73}$$

and the probability can be represented by

$$b_n(t: T+t_1)=e^{-\lambda(T+t_1+y)t}\{\lambda(T+t_1+y)\}^n/n!$$
$$\text{for } n\geqq 0 \tag{74}$$

where

$$\lambda(T+t_1+y)=\frac{1}{t}\int_0^t \lambda(T+t_1+x)dx.$$

Of course, this process is the Poisson process with a variable parameter.

Now, let us generalize slightly the definition of rarity such that

$$\left.\begin{aligned}\lambda_{m1}(T+t_1+t)&=\lambda(T+t_1+t)\\ \lambda_{n1}(T+t_1+t)&=0 \text{ for } n\neq m\end{aligned}\right\}. \quad (75)$$

where $m$ is a fixed integer. This means that $m$ calls occur with probability almost 1 during an infinitesimal interval if calls definitely occur during this interval. Then, the generating function of this process becomes

$$g(s,t:T+t_1)=\exp\left\{-(1-s^m)\int_0^t\lambda(T+t_1+x)dx\right\}. \quad (76)$$

Since this process can be interpreted as a generalized Poisson process with a variable parameter, we can obtain a final result for $I_p$ that $I_p$ can be decomposed to the generalzed Poisson processes with a variable parameter. This is the meaning of Eq. (69).

## 8. Conclusion

There are generally countable impulsive processes in the processes satisfying the condition of independency. These impulsive processes can be subtracted completely from the original one by successive decompositions. The remainder is also decomposed to generalized Poisson Processes with a variable parameter.

## References

(1) J. L. Doob, "*Stochastic processes*," J. Wiley, New York, Chap. 8, p. 654, 1952.
(2) W. Feller, "*An Introduction of Probability Theory and its Applications*," J. Wiley, New York, Chap. 11, p. 461, 1957.

* * * *

U.D.C. 621.395.44.001.2:[621.395.5:621.315.212

# Design of the Terminal Equipments for the 12 Mc/s System on Coaxial Pairs*

*Hideo IIJIMA*†

*The design of carrier terminal equipment for the 12 Mc/s system on the 2.6/9.5 mm standard coaxial cable is described. The author points out that this terminal equipment for the 12 Mc/s system can easily be added to existing lines without modifying the equipments of the present 4 Mc/s system.*

## Introduction

A twelve Mc/s system on 2.6/9.5 mm standard coaxial cable has been under investigation in this laboratory since 1955.

In the design, there are many important factors which should be considered; i.e. the relationship between the new system and the present system, allotment of permissible noise power, economic considerations, etc. The fundamental considerations and design are described in this paper.

## 1. Design Objectives

The frequency allocations and the hypothetical reference circuit which are design fundamentals of the terminal equipment are assumed to conform to those recommended by the C.C.I.T.T. and concluded by the C.C.I.T.T. working party.(1)

Fig. 1 (a) shows the recommendation of the C.C.I.T.T., and Fig. 1 (b) and Fig. 2 show the conclusions obtained by the C.C.I.T.T. working party.

2,500 picowatts is permitted at a zero relative level point as the mean psophometric noise power produced by all the translating equipments in the hypothetical reference circuit shown in Fig. 2. Therefore, a portion of the 2,500 pW should be allotted to the new translating equipments. Consequently, the relationships of the new translating equipments to and the influences of the new translating equipments on the present 4 Mc/s system should be considered very carefully.

In case the 12 Mc/s system coexists with the 4 Mc/s system as shown in Fig. 2, it is economical to use the equipments of present 4 Mc/s system making as little change as possible.

1) The specification for the present supergroup equipment is also to be applied to the new basic mastergroup equipment, since the basic mastergroup is composed of supergroups 4 to 8. Therefore, the specifications for the supergroups equipments and for the lower stages than the supergroup equipment are the same as those for the 4 Mc/s system.

2) Specifications for the translating filters are allowed to be, if necessary, severe because only a small number of types are required.

3) A modulator with low signal leak is desirably used for supermastergroup translation to make the filter design easier.

4) The input level of the modulator is to be determined considering the basic noise and the gain of the amplifier as well as the distortion factor of the modulator.

The number of group and supergroup translating equipments in the hypothetical reference circuit are, as shown in Fig. 2, less by 3 pairs than those of the 4 Mc/s coaxial systems.(2) Therefore, if the noise alloted to

* MS in Japanese received by the Electrical Communication Laboratory April 22, 1959. Published in the *Kenkyû Zituyôka Hôkoku (Electrical Communication Laboratory Technical Journal)*, N.T.T., Vol. 8, No. 6, pp. 653-659, 1959.

† Transmission Section.

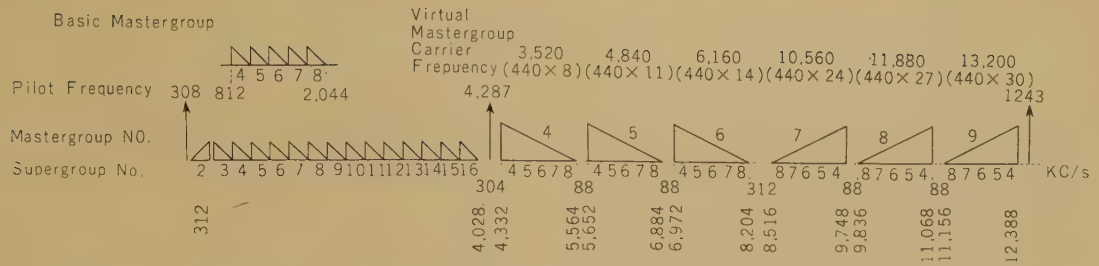


**Fig. 1 (a)**—Allocation of line frequencies for the 12 Mc/s coaxial pair telephone system.

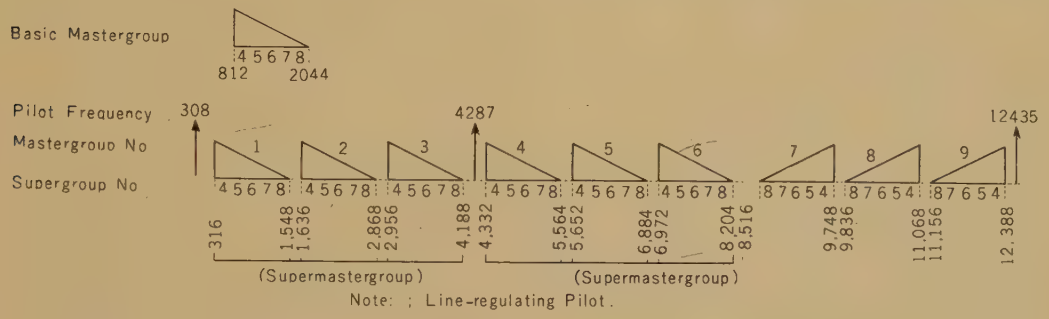


**Fig. 1 (b)**—Allocation of line frequencies proposed as an alternative to Fig. 1 (a).

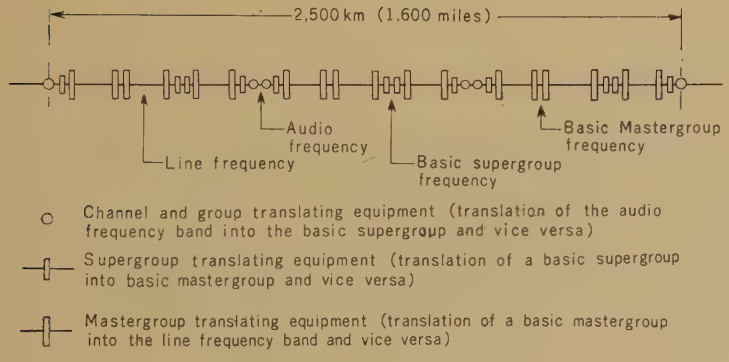


**Fig. 2**—Diagram of the hypothetical reference circuit for 12 Mc/s system on coaxial pairs.

the 3 pairs of group and supergroup translating equipments in the 4 Mc/s system's reference circuit can be assigned interchangeably to the new translating equipments, any changes in specification need not be made for both the supergronp equipments and for their lower stage equipments. Since the noise powers for each pair of the group equipment and for each pair of the supergroup equipment are both approximately 100 pW,[3] a total of 600 pW may be considered to be the object of allotment.

Thus, 450 pW is allotted to the mastergroup and supermastergroup translating equipment; reserving the remainder of 150 pW for branching and allowance.

### 2. Design

The fundamental design of these carrier terminals for the wide band system is in accordance with the method described in

detail in the bibliography.[4]

The basic noise of the amplifier is determined by the first stage vacuum tubes and by the input circuit used.

Some freedom in design remains in connection with distortion, since the output level of the amplifier used for the translating equipments is comparatively low.

In ring modulators using nonlinear elements, however, considerably reduction of distortion due to improvement in the circuit design can not be expected with increase in frequency.

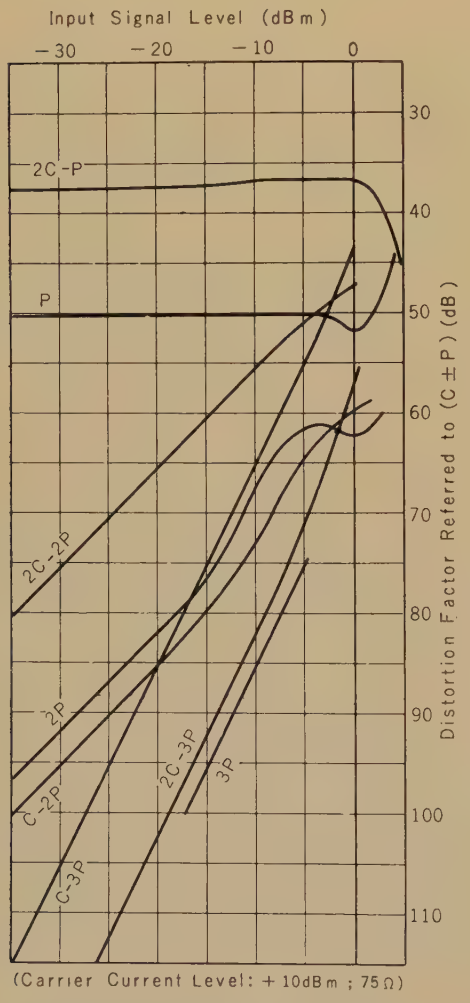


**Fig. 3**—Distortion characteristics of Germanium ring modulator.

(The solution to this difficulty will be realized by the development of a new modulator element in the future.) Therefore, the permissible noise value due to the modulator distortion should first be determined. Fig. 3 shows the characteristics of a Germanium ring modulator.

Considering the several points described above, 450 pW is allotted to the 9 pairs of the mastergroup equipment; i.e. 50 pW per pair, and this 50 pW include the noise power produced by the supermastergroup translating equipment. Noise allotment to the translating stage is shown in Table 1.

**Table 1**

THE ALLOTMENT OF NOISE TO THE TRANSLATING STAGE (ONE PAIR)

| | |
|---|---|
| Basic Noise | 15 pW |
| Intelligible Crosstalk | 10 pW |
| Unused Side Band | 10 pW |
| Nonlinear Distortion | 15 pW |
| Total | 50 pW |

Fig. 4 shows the construction of the translating equipment and the carrier supply equipment, with the pilot frequency supply system omitted.

### 3.1. Filter

Assume that the modulater used in the mastergroup and supermastergroup translation has the following characteristics:

modulator input level: $-30$ dB
signal leak: $S/(\text{signal leak}) = +30$ dB
carrier leak: $S/C = -30$ dB

The signal leak of mastergroups 7, 8, and 9 produces intelligible crosstalk on the line corresponding to the supergroups from 4 to 8. The frequency band of this signal leak is, however, far apart from those of mastergroups; and it is easy to design the filter.

Allotting the amount of carrier leak equally to each modulator according to data extra-

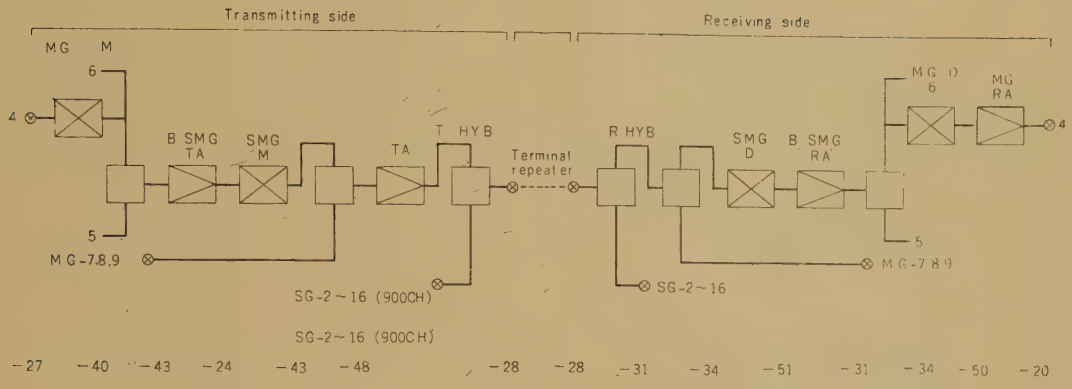


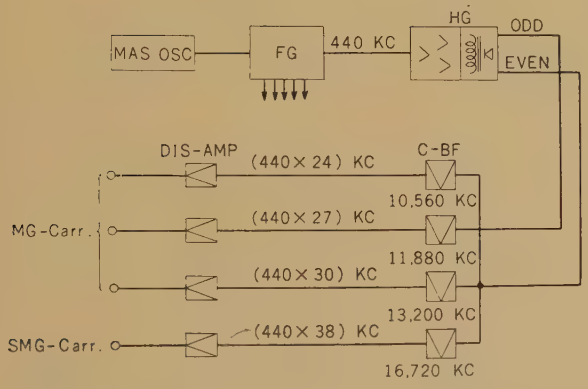


**Fig. 4**—Carrier supply equipment.

polated from the recommendations of the C.C.I.T.T.[5] results in a value of approximately −28 dBm.

From the above considerations the loss characteristics of the mastergroup translating filters are determined as shown in Fig. 5 (a).

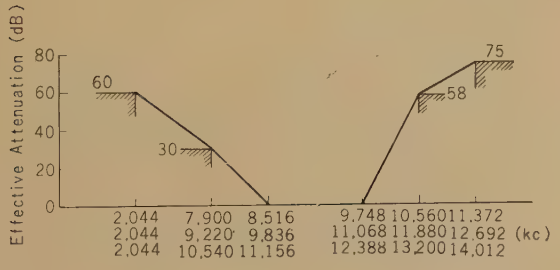


**Fig. 5 (a)**—Band-pass filter specification for mastergroup translation.

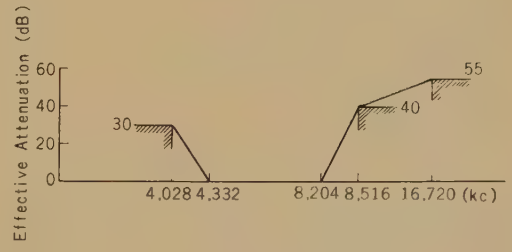


**Fig. 5 (b)**—Specification for supermastergroup translation.

A similar procedure is also to be followed in the design of the supermastergroup translating filters. However, in this translation, the signal leak should be sufficiently suppressed, as this leak produces intelligible crosstalk between the supermastergroups. It is considerably difficult to design the filter, because the spacing

**Table**

NOISE IN AMPLIFIERS

$T_2=(b/B)y_2t_24P^2$

| | | $B$ (c/s) | No. of Channels Contained | $P$ (mW) | Input Level (dBm) | Output Level (dBm) |
|---|---|---|---|---|---|---|
| MG | MOD | $1.232\times10^6$ | 300 | 13.2 | −30 | |
| | DEM | 〃 | 〃 | 〃 | −35 | |
| | RA | 〃 | 〃 | 〃 | −49 | −20 |
| SMG | MOD | $3.872\times10^6$ | 900 | 30.9 | −30 | |
| | DEM | 〃 | 〃 | 〃 | −39 | |
| B-SMG | RA | 〃 | 〃 | 〃 | −51 | |
| | TA | 〃 | 〃 | 〃 | −49 | −27 |
| TA | | $8.056\times10^6$ | 1,800 | 60.0 | −49 | −25 |

Note: (1) $b=3.1\times10^3$ (c/s). (2) Base noise and distortion noise

between the mastergroup Nos. 6 and 7 is only 312 kc/s. Concerning the noise at this filter, it is better to moderate the requirement for the filter by making a larger allotment of noise than is necessary for the other sections. Fig. 5 (b) is thus obtained.

### 3.2. Modulator

By assuming the standard characteristics of the ring modulator to be those shown in Fig. 3, we can obtain the nonlinear distortion noise. The influence of every channel to the adjacent channels should be considered because 3 mastergroups are combined together at the mastergroup translation.

Since the spacing between each mastergroup is only 88 kc/s, the suppression of the adjacent bands by the band-pass filter is very difficult. Therefore, the superposition of the pass band to some degree on the adjacent groups is unavoidable. Judging from the past experience the pass band is supposed to be overlapped by one fifth at least.

Consequently, the distribution of distortion[5] in the mastergroup 8 is probably shown by the cross hatches portion in Fig. 6; and the highest values of the distribution factor in the band are $y_2=0.6$ and $y_3=0.7$.

In the supermastergroup translation these troubles will never happen since the adjacent bands are perfectly separated by the band-pass filter designed to suppress signal leak.

It is assumed that amplifier in the translating equipments has from 20 to 25 dB negative feedback.

Therefore, the level diagram of these terminal equipments together with the permissible noises for the modulator and amplifier is given in Table 2, and the relationship between them is illustrated in Fig. 7.

### 3.3. Intelligible Crosstalk and Other Matters

From our experience, effective attenuation of crosstalk caused by bay wiring, harmful carrier frequencies, etc. can be kept to more

2

AND MODULATORS

$T_3=(b/B)y_3t_3 24P^3$

| $y_{2max}$ | $y_{3max}$ | $t_2$ (dBm) | $t_3$ (dBm) | Basic Noise (pW) | Distortion Noise | |
|---|---|---|---|---|---|---|
| | | | | | $T_2$ (pW) | $T_3$ (pW) |
| 0.6 | 0.7 | −85 | −105 | | 1.65 | 1.55 |
| 〃 | 〃 | −90 | −115 | | 0.52 | 0.155 |
| 〃 | 〃 | −90 | −110 | 3.15 | 0.52 | 0.49 |
| 0.5 | 0.56 | −85 | −105 | | 2.45 | 5.1 |
| 〃 | 〃 | −94 | −123 | | 0.31 | 0.08 |
| 0 | 〃 | | −119 | 5.02 | | 0.2 |
| 〃 | 〃 | | −119 | 3.15 | | 0.2 |
| 0.45 | 〃 | −95 | −140 | 3.15 | 0.4 | 0 |
| | | | Total | 14.47 | 5.85 | 7.775 |

are shown in respectively psophometric power.

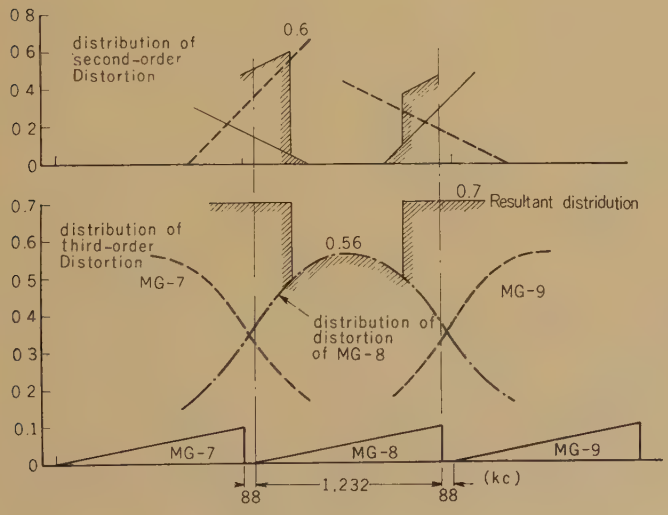


**Fig. 6**—Distribution of nonlinear distortion in mastegroup translation.

than 80 dB. Therefore the intelligible cross-talk caused by the above sources is estimated to be only several pW.[3]

The dead loss of the carrier filter should be kept as small as possible. Fig. 8 shows the specification for the crystal filters.

Frequency stability of $5\times10^{-8}$ cycles per second/°C is required for the carrier frequency. A study of the aging of quartz elements is now being conducted.

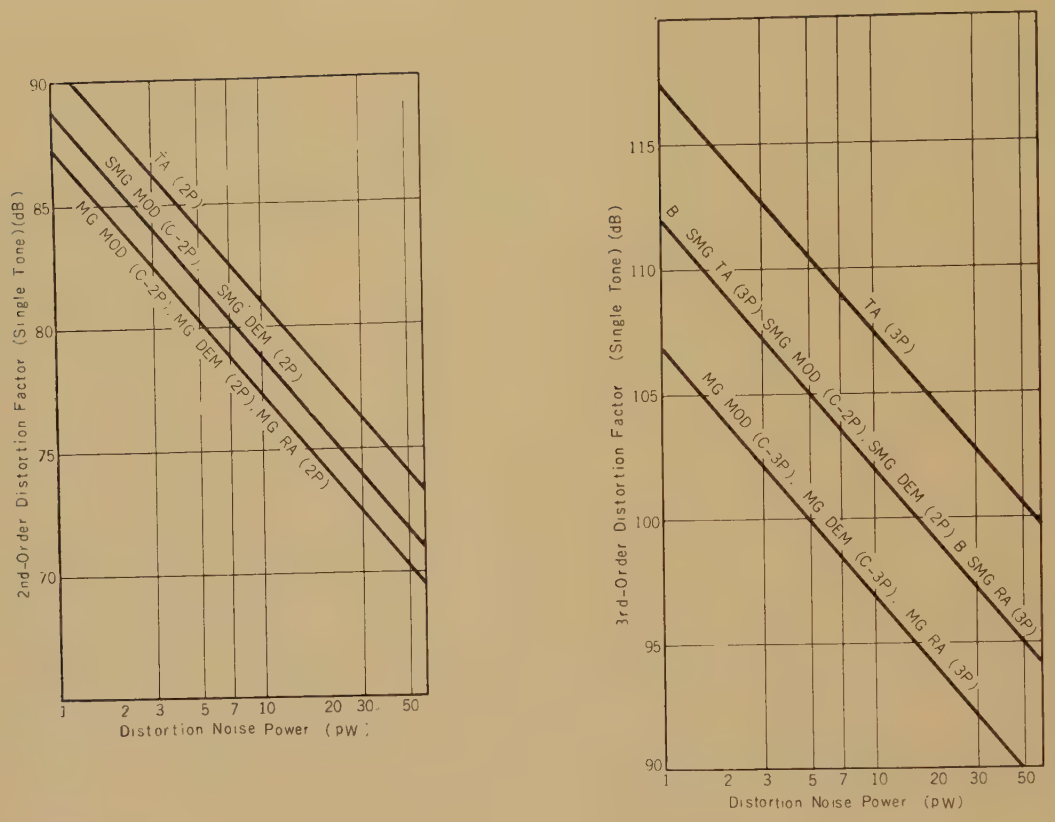


**Fig. 7**—Alloted psophometric noise power and distortion factor for amplifiers and modulators.

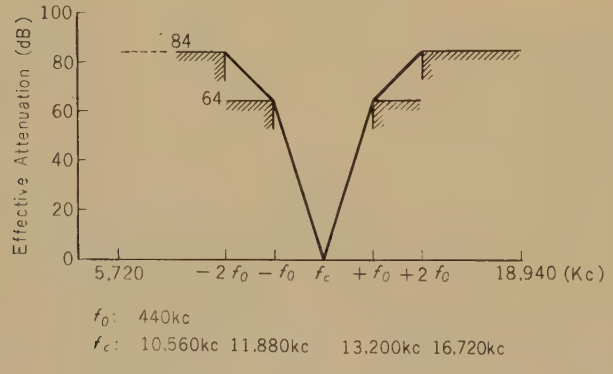


**Fig. 8**—Specification of carrier filters.

### Conclusion

The design objectives and an example of the telephone terminal equipment used for the 12Mc/s system on coaxial pairs are given. The author has shown that the equipments of the new translating stages can be constructed without making modifications on the present equipments.

The equipment has been made experimentally according to these design objectives determined in the laboratory; and it has been verified by tests that the expected results have almost been obtained. The details of

these results will be described in the future.

The equipments had been designed in advance of the meeting of the C.C.I.T.T. and the design objectives aimed at are more strict than those given by the working party of C.C.I.T.T.. It has consequently been ascertained that a new 12 Mc/s coaxial system conforming to the international circuit objectives can be constructed very easily by making a slight change in the level diagram.

**Acknowledgement**

The author is thankful for the kindness of Dr. Yazaki, Chief of Transmission Section, and his other friends who have favored him with good corporation and discussion.

**References**

(1) C.C.I.T.T. XVIIIth Plenary Assembly, Vol. III, *bis*, p. 111. C.C.I.T.T. Studygroup-1 Contribution 7, "Report of the Hauge meeting" Oct. 1957. "Report on meeting of M. Claey's Working Party," March 1959 at Munich.

(2) Same to (1) Vol. III *bis*, p. 109.

(3) The Specification for the 4 Mc/s system of the Nippon Telegraph and Telephone Public Corp.

(4) Ginsaku Yazaki, "The design of the wide band terminal equipment," The Journal of the Institute of Electrical Communication Engineers of Japan, **40**, 4, (1957-4).

(5) C.C.I.T.T. XVIIIth Plenary Assembly, Vol. III, *bis* and C.C.I.F. XVIIIth Plenary Assembly, Vol. III.

(6) R. A. Brockband and C. A. Wass, "Nonlinear Distortion in Transmission Systems," J.I.E.E., **92**, 12–20, Pt. II, (1945).
B. D. Holbrook and J. T. Dixon, "Load Rating Theory for Multi-channel Amplifiers," B.S.T.J., **18**, 4, (1939).

* * * *

U.D.C. 678.743

# Thermal Degradation of Polytrifluorochloroethylene*

*Nobuo YAMADA*†

*The mechanism of the thermal degradation of polytrifluorochloroethylene has been studied by means of measurements of the degree of polymerization of residual polymer molecules which were decomposed in vacuum under various experimental conditions.*

*As a result, it is found that the behavior of the thermal degradation of this polymer can not be explained by the theories which assume that the C-C links of polymer chains decompose at random, but the behavior can be explained excellently by the theory proposed by Jellinek who assumes that there are "weak links" in polymer chains and that these "weak links" decompose at random.*

## Introduction

In this paper, the mechanism of the thermal degradation of polytrifluorochloroethylene $(\text{-}CF_2\text{-}CFCl\text{-})p$ is examined.

This polymer is insoluble in any organic solvent at room temperature; and except for the work of Kaufman and Solomon, the behavior of dilute solutions of this polymer have scarcely been studied. It was therefore necessary to study the solution viscosity of this polymer in order to determine the relation between reduced viscosities and concentrations of solutions; and it was also necessary to find the molecular weight of this polymer as a preliminary study.

## 1. Experiments

Viscosity measurements were carried out in the silicon oil bath which was regulated at the temperature of 98°C by Ubbelohde type viscometer (capillary diameter 0.4 mm, length 80 mm, and flow time of pure solvent 307.4 sec.)

In these measurements, three types of polytrifluorochloroethylene (trade mark name: "Daiflon" produced by Ōsaka Metal. Co. N.S.T. 300, 270, and 240) were used as samples, and 11'3 trifluoropentachloropropane was used as the solvent.

## 2. Results and Discussion

The results are shown in Fig. 1 as the values of reduced viscosities $\eta_{sp}/C$ at various concentrations. From Fig. 1 it is easily found that the $\eta_{sp}/C$ is proportional to the concentration $C$. As a result, the relation between $\eta_{sp}/C$ and $C$ can be expressed by the following Huggins'-type equation:

$$\eta_{sp}/C=[\eta]+0.21[\eta]^2C \qquad (1)$$

where $[\eta]$ is the intrinsic viscosity.

On the other hand, Kaufman and Solomon[1] have proposed the following equation for the relation between $[\eta]$ and $M$ (molecular weight) for solutions of polytrifluorochloroethylene under the same experimental conditions:

$$[\eta]=2\times10^{-5}M^{1.0} \qquad (2)$$

Therefore, the molecular weight $M$ of this polymer can be calculated from measurements of solution viscosity by means of Eqs. (1) and (2).

* MS in Japanese received by the Electrical Communication Laboratory, May. 27, 1959. Originally published in the *Kenkyû Zituyôka Hôkoku* (*Electrical Communication Laboratory Technical Journal*), Vol. 8, No. 6, pp. 994-1, 001.

† Physical Research Section.

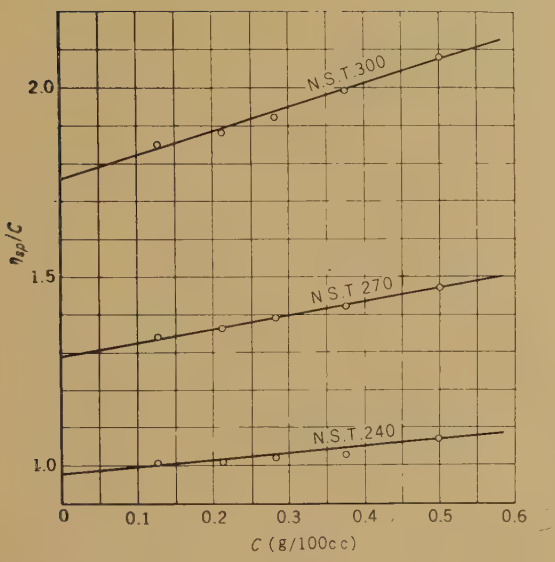


**Fig. 1**—Relation between reduced viscosity and concentration at 98° C.

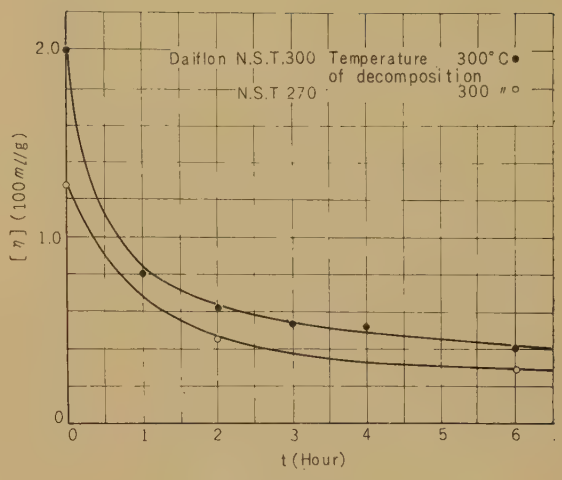


**Fig. 3**—Decrease of intrinsic viscosity by heat treatment.

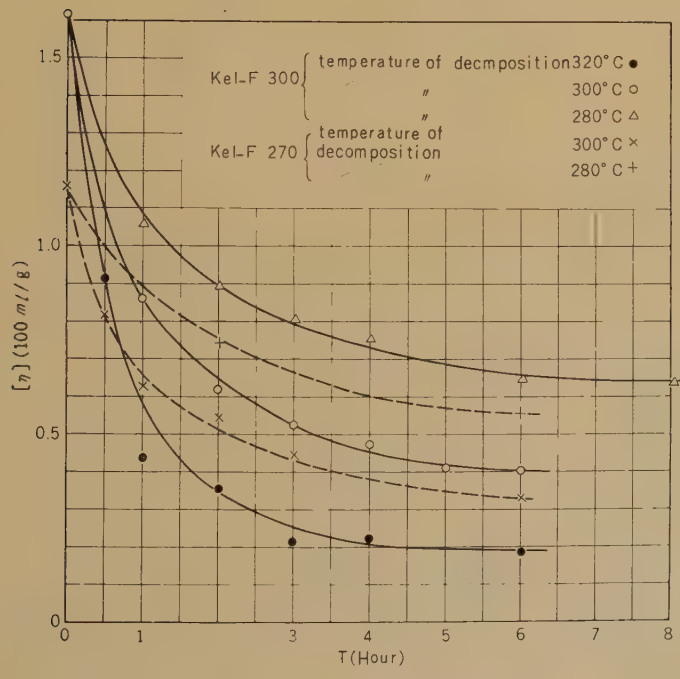


**Fig. 2**—Decrease of intrinsic viscosity by heat treatment.

After these preliminary experiments have been accomplished, four commercial polytrifluorochloroethylene (trade names: "Kel-F" N.S.T. 300 and 270, and "Daiflon" 300 and 270) were decomposed in vacuum at various constant high temperatures between 280° C and 300° C, and the molecular weight (or degree of polymerization $P$) of the residual polymers were measured various reaction time.

These results are shown in Figs. 2 and 3. It is found that the molecular weight of the residue suddenly decreases at the beginning of the reaction, and then gradually further decreases so as to approach its asymptotic critical molecular weight which is a function of the degradation temperature.

There are many theories for the thermal degradation of a linear polymer; such as those proposed by Mark,[2] Montrol,[3] and Sakurada[4]; which assume that the C-C links of the polymer chains decompose at random. According to these theories, depression of the degree of polymerization is expressed by the following equations:

$$\left.\begin{aligned} P_w/P_0 &= \frac{2}{S'}\left(S'-1+\frac{16}{e^{s'}}\right) \\ S' &= kt \end{aligned}\right\} \qquad (3)$$

where $S'$ is the number of decomposed links per original molecule (degree of polymerization $P$), $P_w$ is the weight average degree of polymerization of the degraded molecules after $S'$ links have decomposed, and $t$ is the time of heating.

If these theories are true, $S'$ will be proportional to $t$. The values of $S'$ were calculated from the experimental data by using Eq. (3); and these values of $S'$ were plotted against $t$. The result is shown in Fig. 4.

As it is found from Fig. 4 that $S'$ is not proportional to $t$, the behavior of thermal degradation of polytrifluorochloroethylene can not be explained by these theories.

On the other hand, Jellinek[5] has derived the following equations between the degree ot polymerization of a degraded polymer and the number of the decomposed "weak links," on the assumption that there are a constant number of "weak links" in the polymer chains and that these "weak links" are distributed at random in chains:

$$\begin{aligned} P_{wms} = P_0\Bigg\{ & \left(\frac{m-s}{m}\right)^m + {}_mC_1\left(\frac{S}{m}\right)\left(\frac{m-s}{m}\right)^{m-1}\frac{2}{3} \\ & + {}_mC_2\left(\frac{s}{m}\right)^2\left(\frac{m-s}{m}\right)^{m-2}\frac{1}{2} + \cdots\cdots\Bigg\} \\ & + {}_mC_{m-1}\left(\frac{s}{m}\right)^{m-1}\frac{m-s}{m}\,\frac{(m-1)}{P_0^2} \\ & \times \sum_1^{P_0-1} P^2\left(1-\frac{P}{P_0}\right)^{m-2} + \left(\frac{s}{m}\right)^m \frac{m(m+1)}{P_0^2} \\ & \times \sum_1^{P_0-1} P^2\left(1-\frac{P}{P_0}\right)^{m-1} \end{aligned} \qquad (4)$$

$$\log\left(\frac{m}{m-s}\right) = kt \qquad (5)$$

where $P_0$ is the degree of polymerization of the original polymer, $m$ is the average number of "weak links" per molecule, $s$ is the average number of decomposed weak links per original polymer, $P_{wms}$ is the weight average degree of polymerization of the whole sample after links of number $s$ have decomposed, and $k$ is a contact.

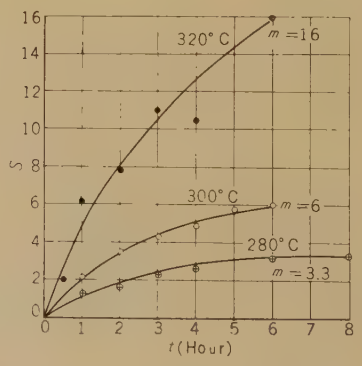


**Fig. 4**—Time dependency of $S'$ assuming random decomposition.

This theory was applied to our experiments and then the values of $m$ and $s$ were calculated from the experimental results.

**Table 1**

| | Kel-F N.S.T. 300 | | | Kel-F N.S.T. 270 | | Daiflon N.S.T. 300 | Daiflon N.S.T. 270 |
|---|---|---|---|---|---|---|---|
| | 320° C | 300° C | 280° C | 300° C | 280° C | 300° C | 300° C |
| $m$ | 16 | 6.0 | 3.3 | 5.0 | 2.2 | 8.0 | 4.3 |
| $P_0$ | 692 | 692 | 692 | 498 | 498 | 858 | 545 |
| $m/P_0$ | 0.023 | 0.008 | 0.005 | 0.010 | 0.004 | 0.009 | 0.008 |

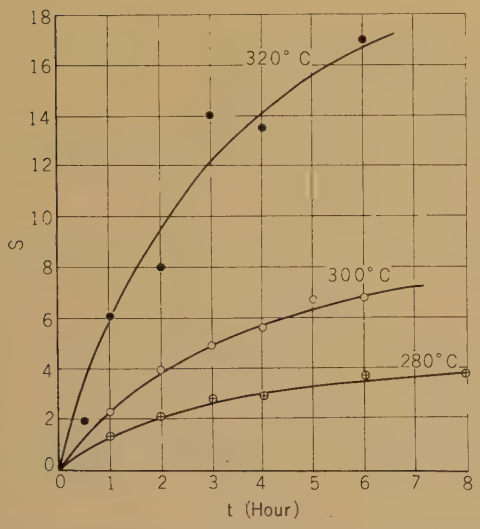


**Fig. 5**—Time dependency of $S$ assuming "weak links" decompositions.

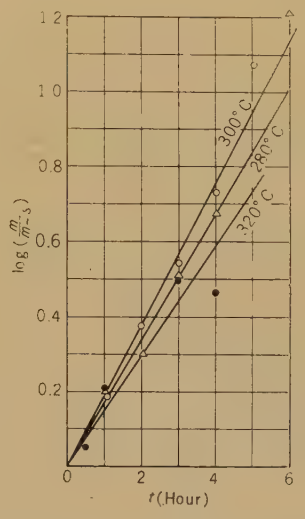


**Fig. 6**—Plot log $(m/m-s)$ against $t$ for Kel-F 300.

These values are shown in Table 1 and Fig. 5 for example. In Fig. 6, $\log m/(m-s)$ is plotted against $t$, and it is found that $\log m/(m-s)$ is nearly proportional to $t$ as shown in Fig. 6 and that therefore Jellinek's theory becomes quantitatively fulfilled by the experiments.

### Conclusion

It is concluded that, at least for the case when the reaction takes place in a vacuum, at high temperatures polytrifluorochloroethylene decomposes at the "weak links" of its polymer chains but not at the *C-C* links of its polymer chains.

* * * *

### References

(1) H. S. Kasfman and E. Solomon, "Fractionation of Chlorotrifluoroethylene Polymer," *Ind. Eng. Chem.*, **45**, p. 1,779, 1953.
(2) H. Mark and R. Simha, "Degradation of Long Chain Molecules," *Trans. Faraday Soc.*, **36**, p. 611, 1940,
(3) E. W. Montroll and R. Simha, "Theory of Depolymerization of Long Chain Molecules," *J. Chem. Phys.*, **8**, p. 721, 1940.
(4) I. Sakurada and S. Okamura, "Über den Abbau langer Kettenförmiger Moleküle," *Z. Physik. Chem., A 187*, p. 289, 1940.
(5) H. H. G. Jellinek, "On the Degradation of Long Chain Molecules," *Trans. Faraday Soc.*, **40**, p. 266, 1944.

# Papers Contributed to Scientific and Technical Journals by the Members of the Laboratory*

## Papers Published in Other Publications of the Electrical Communication Laboratory

U.D.C. 534.13:621.395.6

Some Investigations on the Conical Vibrating Plates for Telephone Receivers and Transmitters
*Kazuo IKEGAYA* and *Masayuki MURAKAMI*
Kenkyû Zituyôka Hôkoku (Electr. Comm. Labor. Techn. Journ.), NTT, **9**, 4, p. 431–443, Apr. 1960

Large models of the conical vibrating plates for telephone transmitters and receivers were measured, and by use of the results obtained the characteristic constants of the actual conical diaphragms and the effects of radial corrugations on the vibrating plates are calculated.

U.D.C. 621.385.632.12:621.375.018

Distributed Amplifier Tube
*Takuya KOJIMA*
Kenkyû Zituyôka Hôkoku (Electr. Comm. Labor. Techn. Journ.), NTT, **9**, 3, p. 201–244, Mar. 1960

A wide band amplifier tube based on the principle of distributed amplification was developed. An experimental tube gave nearly flat gain over the band from zero to 150 Mc/s.

U.D.C. 621.394.3-185.4:681.613.4

General Investigation of Teleprinter Construction
*Sanae AMADA*
Kenkyû Zituyôka Hôkoku (Electr. Comm. Labor. Techn. Journ.), NTT, **9**, 4, p. 321–372, Apr. 1960

Some results of an investigation on elementary teleprinter units new propositions are discussed; and furthermore, considerations concerning the design, the production, and the methods of measuring these units are described.

U.D.C. 621.395.31:519.2

On Stochastic Representations for Incoming Telephone Calls
*Gisaku NAKAMURA*
Kenkyû Zituyôka Hôkoku (Electr. Comm. Labor. Techn. Journ.), NTT, **9**, 4, p. 373–396, Apr. 1960

A general study of stochastic representations for incoming telephone calls was made. In this paper it is shown that the occurrence of calls can be expressed by the generalized Poisson process and by the impulsive type process.
The physical mechanism and characteristics of a magnesium-oxide cold cathode are described. Also, relations between the properties of the magnesium oxide and the properties of the cold cathode are discussed.

* Reprints may be available upon your request to the author.

U.D.C. 621.3.032.212:537.533

Cold Cathode Using Magnesium Oxide
*Tatsuji IMAI*
Kenkyû Zituyôka Hôkoku (Electr. Comm. Labor. Techn. Journ.), NTT, **9**, 4, p. 397–424, Apr. 1960

On magnesium oxide cold cathode which has been developed, outline of physical mechanism, some characteristics and relations between properties of magnesium oxide and cold cathode are described.

U.D.C. 621.391:[621.391.883:621.394.1

On the Group Synchronizing of Binary Data Transmission
*Toshi MINAMI*
Kenkyû Zituyôka Hôkoku (Electr. Comm. Labor. Techn. Journ.), NTT, **9**, 4, p. 425–429, Apr. 1960

There are many kinds of synchronizing methods for binary data transmission. In this study, the synchronizing error probability is sought when the bit error rate is given, and it is proved that the synchronizing pattern insertion method is most efficient synchronizing method.

U.D.C. 621.923.75.001.2:534.133

VHF Crystal Polishing and the Nature of Polished Quartz Surfaces
*Ichiro IDA* and *Yuzo ARAI*
Kenkyû Zituyôka Hôkoku (Electr. Comm. Labor. Techn. Journ.), NTT, 9, 3, p. 245–317, Mar. 1960

Polishing techniques for quartz oscillator-plates with frequencies of up to 140 Mc/s are described, and the polishing mechanism is discussed as the aggregation of micro-scratchings and also from the standpoint of residual stresses.

**Papers Published in Publications of Scientific and Technical Societies**

U.D.C. 621.382.323

A New Type Field Effect Transistor
*Toshiya HAYASHI*
The Journ. Inst. Electr. Comm. Engrs. Japan, **43**, 3, p. 298–305, Mar. 1960

A new type field effect transistor that is easy to produce is proposed; and construction, principle of design, method of production, and fundamental characteristics of experimentally produced transistors are described.

U.D.C. 621.382.333.029.6

High Frequency Transistors: Fused-Alloy Junction Type
*Tatsuya NIIMI* and *Susumu YOSHIDA*
The Journ. Inst. Electr. Comm. Engrs. Japan, **43**, 3, p. 424–426, Apr. 1960

This paper describes recent alloying techniques for producing planar p-n junctions. A high frequency alloy transistor with an $f_\alpha$ of 50–100 Mc/s developed in the Electrical Communication Laboratory is also discussed.

U.D.C. 621.382.2.029.621.63
621.375.9

Diodes for Microwave Frequency Use: Diodes Used for Parametric Amplification
*Shoichi KITA*
The Journ. Inst. Electr. Comm. Engr. Japan, **43**, 4, p. 456–459, Apr. 1960

The principles of semiconductor diodes for parametric amplification are discussed, and typical diodes now in use are described.

U.D.C. 621.383.3.004.6

Reliability of Transistors and Diodes: Reliability and Mechanism of Deterioration
*Tatsuya NIIMI* and *Sukejiro SHIKAMA*
The Journ. Inst. Electr. Comm. Engr. Japan, **43**, 4, p. 489–495, Apr. 1960

The reliability of transistors is reviewed and the physical mechanism of the degradation of transistor life is discussed in terms of the variation of surface properties.

U.D.C. 621.382:621.395.34

Uses of Semiconductor Elements: Electronic Switching
*Ichiro ENDO*
The Journ. Inst. Electr. Comm. Engr. Japan, **43**, 4, p. 506–511, Apr. 1960

Various types of semiconductor circuits for electronic exchange systems, including the unique speech path circuit in the experimental "$\omega$" system developed in the Electrical Communication Laboratory, are described.

U.D.C. 621.382.3:621.395

Applications in Semiconductor Elements to Wire Communication Apparatus
*Ginsaku YAZAKI*
The Journ. Inst. Electr. Comm. Engr. Japan, **43**, 4, p. 520–524, Apr. 1960

Theory and circuit design of singl-ended transistorized both-way repeaters for use on telephone transmission lines are discussed, and actual amplifiers are described.

U.D.C. 621.382.3:621.396

Applications of Semiconductor Elements to Wireless Communication Apparatus
*Tadasu FUKAMI*
The Journ. Inst. Electr. Comm. Engr. Japan' **43**, 4, p. 524–529, Apr. 1960

Applications of semiconductor devices to ratio communication apparatus in high frequency circuits, in frequency converter circuits, and in intermediate frequency circuits are discussed: and some experimental apparatus using these devices are described.

U.D.C. 621.382.3:608.3

Short Review of Patents Concerning Semiconductor Devices
*Minoru AIDA, Kinya OKUBO,* and *Toshiaki KISHIGAMI*
The Journ. Inst. Electr. Comm. Engr. Japan, **43**, 4, p. 538–543, Apr. 1960

Important patents concerning semiconductor devices issued after 1956, are classified into two groups: production methods and circuits. These patents are explained and tabulated according to applicants.

U.D.C. 678.742.3:539.19:539.26

Proton Magnetic Resonance and X-Ray Diffraction Studies of Polypropylene
*Atsuo NISHIOKA, Yasuhiro KOIKE, Masakazu OWAKI, Tsunezo NARABA,* and *Yoshinori KATO*
Journ. Phys. Soc. Japan, **15**, 3, p. 416–428, Mar. 1960

Crystallization and glass transition in various test samples of polypropylene were investigated by means of proton magnetic resonance over the wide range temperature from −180° C to 200° C and by means of X-ray diffraction at room temperature.

U.D.C. 541.64:678.012

Theory of Solutions of Chain Molecules
*Hiroshi OKAMOTO*
Journ. Phys. Soc. Japan, **15**, 4, p. 650–657, Apr. 1960

Using the first order Bethe approximation, a theory of solutions of chain molecules has been developed in which we considered the detailed configuration of chain molecules on a local system. The results are better than those of previous theories.

U.D.C. 678.743:541.64:541.24:532.13

Study on Poly-(Trifluorochloroethylene)
VI. Determination of Molecular Weight-Intrinsic Viscosity Relation
*Susum FURUYA* and *Masakazu HONDA*
Chemistry of High Polymers **17**, 180, p. 202–206, Apr. 1960

The molecular weight-intrinsic viscosity relation of poly-(trifluorochloroethylene) has been determined in ortho-chlorobenxotrifluoride at 130° C.

U.D.C. 678.842:541.64:541.24:532.13

Viscosity-Molecular Weight Relation for High Molecular Weight Poly-(Dimethylsiloxane)
*Susumu FURUYA*
Journ. of Japan Soc. for Testing Materials **9**, 79, p. 288–292, Apr. 1960

Viscosity of poly-(dimethylsiloxane) of molecular weights ranging from $6.1\times10^4$ to $23.5\times10^4$ were determined. Viscosities at 40° C and low shear rates were related to molecular weight $M$ by the equation, $\log\eta=3.5\log M-14.88$.

* * * *

Vol. 8 Nos. 5-6 MAY - JUNE 1960

# CONTENTS